



Norwegian University of
Science and Technology

Characterisation of photochromic oxygen-containing yttrium hydride by electron microscopy

Håkon Wiik Ånes

Master of Science in Physics and Mathematics

Submission date: June 2017

Supervisor: Antonius Theodorus Johann Van Helvoort, IFY

Co-supervisor: Fredrik Aleksander Martinsen, Institute for Energy Technology

Norwegian University of Science and Technology
Department of Physics

Abstract

Smart windows based on chromogenic materials have in recent years emerged as promising candidates for the next generation of energy-efficient windows. One group of chromogenic materials are photochromic, which are characterised by their ability to change their optical properties reversibly when exposed to light. They can thus be used in the fabrication of windows with dynamic control of solar energy. A photochromic oxygen-containing yttrium hydride (YHO) thin film is an attractive candidate for use in smart windows, but its detailed morphology and the development of the crystal structure, texture and oxygen concentration with film thickness are largely unknown.

YHO thin films with thicknesses of 100 nm and 650 nm were synthesised by reactive magnetron sputtering deposition on silicon and gallium arsenide substrates. SEM studies were done on film fragments dispersed on copper grids with carbon film. Plan-view and cross-section specimens for TEM studies were prepared by ultramicrotomy and tripod polishing. The specimens were studied using scanning precession and selected-area electron diffraction, bright-field and dark-field imaging, high resolution TEM, energy-filtered TEM and scanning TEM in combination with energy dispersive X-ray spectroscopy. The sets of scanning precession electron diffraction data were analysed using automated crystal orientation mapping and multivariate statistical analysis.

The films were found to have an expanded YH_2 fcc structure with a lattice parameter of 5.39 Å. Evidence of one or more additional crystalline phases in the film were found in diffraction experiments, however they were not identified. The microstructure of the films is dominated by a column growth, resembling *zone T* in the structure zone model for sputtering deposited thin films. The columns consist of multiple grains with an average grain size of 15 nm. The oxygen concentration was found to be highest in the film bottom and decreasing towards the top surface. This variation is attributed to a variation in the surface area of the structure from largest in the bottom due to smaller structures and smallest in the top due to expanding column growth structures. The crystal texture in the growth direction went from a weak [111] texture in the bottom, to a competitive growth with no texture in the lower middle, to finally a near unique [001] texture from the middle and towards the surface. The [001] texture dominates the microstructure.

Cover: *Different representations of the same thin film. Upper left: bright-field transmission electron microscope image. Upper right: orientation map in growth direction, colour from $m\bar{3}m$ inverse pole figure. Lower left: oxygen signal from X-ray spectroscopy. Lower right: loading map from non-negative matrix factorisation of a scanning precession electron diffraction dataset.*

Sammendrag

Smarte vinduer basert på kromogene materialer har de siste årene vokst frem som lovende kandidater for neste generasjon av energieffektive vinduer. En gruppe kromogene materialer består av fotokrome forbindelser, som karakteriseres av deres evne til å endre optiske egenskaper reversibelt under bestråling av lys. De kan dermed brukes i fabrikering av vinduer for dynamisk kontroll av solenergi. En fotokrom, oksygenrik yttriumhydrid (YHO) tynnfilm er en attraktiv kandidat for bruk i smarte vinduer, men filmens detaljerte morfologi samt utviklingen av krystallstruktur, tekstur og konsentrasjon av oksygen med tynnfilmtykkelse er for det meste ukjent.

Tynnfilmer av YHO med tykkelser på 100 nm og 650 nm ble syntetisert i en reaktiv magnetron pådampingsprosess på substrater av silisium og galliumarsenid. Studier med skanneelektronmikroskop ble gjort på fragmenter av tynnfilmene spredd utover koppergrid med karbonfilm. Prøver for studier i transmisjonelektronmikroskopi fra tynnfilmtoppen og -siden ble preparert med ultramikrotomering og tripodpolering. Prøvene ble studert med skannepresesjonelektron-diffraksjon og områdevalgt elektrondiffraksjon, lysefelts- og mørkefeltsavbildning, høyoppløsnings TEM, energifiltrert TEM og skanne-TEM i kombinasjon med energidispersiv røntgenspektroskopi. Settene med diffraksjonsmønstre fra skannepresesjonelektrondiffraksjon ble analysert i en automatisert kartlegging av krystallorienteringer og dekomponeringsalgoritmer fra multivariable statistisk analyse.

Filmene har en ekspandert YH_2 flatesentrert, kubisk krystallstruktur med en gitterparameter på 5.39 Å. Bevis for en eller flere ekstra krystallfaser i filmene ble funnet i diffraksjonseksperiment som ikke tidligere er rapportert om. Filmens mikrostruktur er dominert av kolonnevekst som minner om T-sonen i struktursonemodellen for pådampningssyntetiserte tynnfilmer. Kolonnene består av flere korn med en gjennomsnittlig kornstørrelse på 15 nm. Konsentrasjonen av oksygen er høyest i filmens bunn og synkende mot filmens overflate. Den observerte variasjonen er begrunnet med en variasjon i mikrostrukturens overflateareal, som er størst i bunn grunnet mindre strukturer og minst i toppen grunnet den dominerende, større kolonnestrukturen. Krystallteksturen i vekstretning gikk fra [111]-tekstur i bunn, til en konkurrerende vekst med ingen tydelig tekstur i nedre midtdel, til en endelig nær unik [001]-tekstur i resterende del mot overflaten. [001]-teksturen dominerer mikrostrukturen.

Preface

This thesis is a conclusion of my MSc. degree in Applied Physics at the Department of Physics of the Norwegian University of Science and Technology (NTNU), Trondheim. 30 credits have been spent on this work during the spring of 2017. The thesis is a result of the collaboration between the Institute for Energy Technology (IFE), Kjeller and the Department of Physics at NTNU. The experimental work has been carried out at the Department of Physics with Prof. Antonius T. J. van Helvoort from NTNU and Dr. Fredrik A. Martinsen from IFE as supervisors.

I sincerely thank Antonius and Fredrik for their greatly valued guidance, patience and enlightening discussions regarding the materials, the techniques and life in general. I thank senior engineers Bjørn Soleim and Ragnhild Sæterli at the TEM Gemini Centre for teaching me the different TEM techniques and preparation methods, seeing to that the instruments stay operational and for answering my sometimes desperate messages from the lab when things are not looking as they are supposed to. PhD students Jonas Sunde, Tina Bergh, Adrian Lervik and Emil Christiansen have my gratitude for useful discussions on the scanning precession electron diffraction technique and for providing source code snippets, making my life a lot easier. I would like to add that the TEM group as a whole is a wonderful and professional scientific environment to be a part of. Lastly, I thank my girlfriend Sarai Dery Folkestad for her great and loving support.

Håkon Wiik Ånes
NTNU, Trondheim
June 18, 2017

Abbreviations

ACOM-TEM	automated crystal orientation mapping in TEM
ADF	annular dark-field
bcc	body-centred cubic
BF	bright-field
BFP	back focal plane
BSE	backscattered electron
C1, C2	condenser lens 1, 2 etc.
CBED	convergent beam electron diffraction
CCD	charge-coupled device
CS	cross-section
DF	dark-field
DP	diffraction pattern
EDS	energy-dispersive X-ray spectroscopy
EELS	electron energy loss spectroscopy
EFTEM	energy-filtered TEM
fcc	face-centred cubic
FEG	field-emission gun
FFP	front focal plane
FFT	fast Fourier transformation
FT	Fourier transform
HAADF	high-angle annular dark-field

HRTEM	high-resolution transmission electron microscopy
IFE	Institute for Energy Technology
IL	intermediate lens
IPF	inverse pole figure
NBD	nanobeam diffraction
NMF	non-negative matrix factorisation
ODF	orientation distribution function
OL	objective lens
PCA	principal component analysis
PED	precession electron diffraction
PV	plan-view
PVD	physical vapour deposition
SAD	selected-area diffraction
SE	secondary electron
SEM	scanning electron microscope/microscopy
SPED	scanning precession electron diffraction
STEM	scanning transmission electron microscope/microscopy
SZM	structure zone model
TEM	transmission electron microscope/microscopy
VBF	virtual bright-field
VDF	virtual dark-field
VLM	visible light microscope/microscopy
XRD	x-ray diffraction
YH ₂	yttrium hydride
YHO	oxygen-containing yttrium hydride

Contents

Abstract	i
Sammendrag	ii
Preface	iii
Abbreviations	v
1 Introduction	1
2 Theoretical background	3
2.1 Crystal structure	3
2.1.1 Periodic array of atoms	3
2.1.2 Types of lattices	4
2.1.3 Index system for crystal planes	5
2.1.4 Reciprocal lattice	5
2.1.5 Dislocations	7
2.2 Transmission electron microscopy	7
2.2.1 Electron scattering and diffraction	8
2.2.2 Microscope design	14
2.2.3 Operation modes	16
2.3 Scanning electron microscopy	24
2.4 Crystal texture analysis	26
2.4.1 Orientations and misorientations	26
2.4.2 Orientation mapping	28
2.4.3 Grain size analysis and misorientations	29
2.5 Multivariate statistical analysis	31
2.6 Photochromism	33
2.6.1 Photochromism in oxygen-containing yttrium hydride	35

2.7	Thin film synthesis	36
2.7.1	Reactive sputtering deposition	37
2.7.2	Column growth morphology	37
3	Experimental methods and data processing	41
3.1	Thin film synthesis	41
3.2	Sample preparation	41
3.2.1	Transmission electron microscopy specimen preparation	42
3.2.2	Scanning electron microscopy sample preparation	44
3.3	Characterisation	44
3.3.1	Transmission electron microscopy studies	44
3.3.2	Scanning electron microscopy studies	46
3.4	Data processing	46
3.4.1	Crystal structure determination	47
3.4.2	Virtual imaging	47
3.4.3	Multivariate statistical analysis	47
3.4.4	Crystal orientation determination	47
3.4.5	Orientation data filtering and grain reconstruction	48
3.4.6	Energy-dispersive X-ray spectroscopy quantification	50
3.4.7	Image processing	50
4	Results	51
4.1	Column growth morphology	51
4.2	Crystal structure	53
4.3	Thin film texture	61
4.4	Grain size and misorientations	65
4.5	Elemental composition	70
4.6	Specimen preparation	72
5	Discussion	75
5.1	Microstructure and oxygen concentration	75
5.1.1	Crystal phases	75
5.1.2	Grain size and misorientations	76
5.1.3	Oxygen and yttrium EDS signals	77
5.1.4	Region i: bottom	77
5.1.5	Region ii: lower middle	78
5.1.6	Region iii: top half	78

5.1.7	Thin film growth and reaction model	79
5.2	Methods	80
5.2.1	Problem of overlapping grains	80
5.2.2	Data acquisition and processing	81
5.2.3	Specimen preparation	82
6	Conclusions	83
7	Further work	85
	References	87
A	Ultramicrotomy scheme	93
A.1	Film removal from substrate	93
A.2	Pre-sectioning cutting	94
A.3	Sectioning	94
B	Tripod polishing scheme	95
B.1	Cutting and gluing	95
B.2	Reference plane polishing	96
B.3	Second side polishing	97
B.4	Specimen mounting	98
C	Data analysis code snippets	99
D	Study of GaAs nanowires	105

1 | Introduction

The global energy demand is estimated to increase by one-third between 2013 and 2040.¹ Meanwhile, energy-related CO₂ emissions are projected to be 16% higher by 2040,¹ rendering the prospect of keeping global warming below 2 °C an unlikely one.² In addressing this challenge, one of the aims from the 2015 United Nations Climate Change Conference in Paris states that the world's countries should be 'Making finance flows consistent with a pathway towards low greenhouse gas emissions and climate-resilient development'.³ On top of this, world population growth is estimated to rise from 7.3 billion in 2016 to 9.8 billion in 2050,⁴ and clean, low-cost energy must be available to all. It is fair to say that the stage is set for innovations in nanotechnology and other advances in materials science to transform this vision into a reality.

Commercial and residential buildings are responsible for 20–40% of the total, global energy consumption,⁵ owing in large to the use of air-conditioning, heating and lighting. In fact, as of 2013 people in the US used as much electricity for air-conditioning as was consumed for all purposes by all 930 million residents of the continent of Africa.⁶ A way in which to reduce this consumption is to apply a thin film coating to windows in order to limit the amount of solar radiation entering or black-body radiation leaving a building.

Windows with adaptive capabilities belong to the family of *smart windows*. In general, the appearance of a smart window changes between transparent and opaque. The transformation is a result of applying an external stimulus like light, voltage or heat, which induces a reversible change in the materials properties so that more or less light passes through the window. The process is termed *chromism* and the materials that undergo chromism are called *chromogenic*. A variant of these smart windows are already in use in e.g. Boeing 787 Dreamliner airplanes.⁷ They use an *electrochromic* panel that can be darkened or bleached, depending on the applied voltage set by the user. However, these materials have long response times and high fabrication and implementation costs, limiting the range of applications.

Another usage example of chromogenic materials are sun glasses with a coating that darken upon illumination of ultra violet (UV) light and return to its initial state when the source of UV light diminishes or is removed. The glasses' coating is *photochromic*, meaning it changes its appearance when subjected to electromagnetic radiation.⁸ Many families of organic and inorganic photochromic compounds exist,⁹ with many more organic than inorganic compounds. Generally, organic compounds are varied and easy to modify or process, while inorganic compounds have considerable thermal stability, high strength and diverse coordination chemistry. The fundamental processes underpinning the photochromism can be very different. For organic

compounds, photochromism is mostly linked with molecular structural modifications. For inorganic compounds, photochromism is usually related to the presence of some impurities or crystal defects which interact with the electrons liberated under the influence of light.⁸ To work as a reliable switch in smart windows, photochromic systems should be able to undergo a large number of cycles. Although fatigue is present in photochromic systems as with every reactive medium,¹⁰ this is less of a problem for inorganic compounds. Inorganic, photochromic thin films as glass coatings have since the 90s been proposed as an energy efficient and environmentally intriguing technology.^{11–13} Examples include films based on titanium dioxide,¹⁴ vanadium dioxide,¹⁵ and yttrium hydride.¹⁶

An increased research interest on the properties of yttrium hydride started by Huiberts *et. al*¹⁷ in 1996 led in 2007 to the discovery of photochromism in a thin film of YH_2 and $\text{YH}_{3-\delta}$ by Ohmura *et. al*.¹⁶ Photochromism was later observed in oxygen-containing yttrium hydride, termed YHO, by Mongstad *et. al*.¹⁸ The YHO thin film has an initial appearance of yellowish transparent, but darkens under illumination with visible light of moderate intensity. This effect in combination with yttrium's abundance¹⁹ and non-toxicity presents a thin film based on YHO as a strong candidate for use in smart windows.

YHO thin films are synthesised using physical vapour deposition.²⁰ The synthesis starts with yttrium being sputtered from its solid form and deposited onto a substrate, while simultaneously reacting with hydrogen. Yttrium reacts strongly with oxygen, which is introduced in the film after it has been subjected to the atmosphere.²⁰ The strength of the photochromic effect of the resulting film vary with process parameters like the deposition pressure in the chamber and the type of substrate.²¹ The amount of oxygen in and the thickness of the film have been found to affect the photochromic effect,^{22,23} but no conclusion has been made as to what dictates how much oxygen the film absorbs.²⁰ Studies of the microstructure of the film have shown it to be highly porous and contain a large number of cracks which oxidise upon contact with air.²⁴ X-ray diffraction (XRD) experiments^{18,24} show that the YHO thin film in the transparent state has a face-centred cubic crystal structure with a lattice parameter varying from 5.35 Å to 5.4 Å. Synchrotron XRD experiments²⁵ also show that the film is *polycrystalline* and strongly *textured*, meaning that its microstructure consists of small grains with a preferred orientation. However, the microstructure results are averages from the bulk of the film. To understand why the films exhibit different macroscopic properties, a detailed study of the microstructure and oxygen concentration along the film thickness should be pursued.

The goal of this work is to study the evolution of the microstructure and oxygen concentration with film thickness of sputtering deposited, oxygen-containing yttrium hydride thin films. Of particular interest concerning the microstructure is the morphology, crystal structure, texture and grain size. A transmission electron microscope (TEM) is used because its spatial resolution enables a detailed study of these features along the film thickness. A scanning electron microscope (SEM) is also used to complement the TEM. A theoretical background covering crystal structure, electron scattering and diffraction in electron microscopes, crystal texture analysis, multivariate statistical analysis, photochromism and YHO and thin film synthesis by sputtering deposition is provided in §2. The experimental procedures of the thin film synthesis at IFE, specimen preparation for TEM and SEM, how the films are characterised and data processing are covered in §3. The results are presented in §4 followed by a discussion in §5. Conclusions are drawn in §6, followed by proposals for further work in §7.

2 | Theoretical background

Parts of the theoretical background covering crystal structure, TEM and SEM, photochromism and thin film synthesis are adapted from the author's project thesis of fall 2016.²⁶

2.1 Crystal structure

The properties of a solid are often related to its crystal structure. This is essentially because electron waves have short wavelengths responding dramatically to the regular periodic atomic order of the solid.²⁷ A *crystal* consists of a periodically, repeated basic structure known as a *cell*, filling three-dimensional (3D) space. The locations of the origins of these cells form a hypothetical *lattice* which may exist in one-, two- and three dimensions. A crystal is then constructed by first specifying the lattice and then associating an identical group of typically atoms, molecules or ions known as the *basis* with each point in the lattice.²⁸

2.1.1 Periodic array of atoms

A 3D lattice can be defined by three *translation vectors* $\mathbf{a}_1, \mathbf{a}_2, \mathbf{a}_3$, so that the arrangement of atoms in the crystal looks identical when viewed from a point \mathbf{r} as when viewed from every point \mathbf{r}' translated by an integral multiple of \mathbf{a}_i as

$$\mathbf{r}' = \mathbf{r} + n_1\mathbf{a}_1 + n_2\mathbf{a}_2 + n_3\mathbf{a}_3. \quad (2.1)$$

Here n_i are arbitrary integers, and the set of points \mathbf{r}' for all n_i defines the lattice. If there is no cell of a volume smaller than $\mathbf{a}_1 \cdot \mathbf{a}_2 \times \mathbf{a}_3$ that can serve as a building block for the crystal structure, the vectors \mathbf{a}_i are termed the *primitive translation vectors*. These vectors define the *primitive cell*. They are also often used to define the *crystal axes*, spanning the general shape of a parallelepiped. Hence, the total volume of the crystal can be covered by translating this parallelepiped through every lattice vector \mathbf{r}' defined by (2.1).²⁷

The *basis* of the crystal structure can now be defined by the crystal axes. The position of an atom j of the basis relative to the associated lattice point \mathbf{r}' is given as

$$\mathbf{r}_j = x_j\mathbf{a}_1 + y_j\mathbf{a}_2 + z_j\mathbf{a}_3. \quad (2.2)$$

The basis can consist of one or more than one atom. The origin of the cell, that is the associated lattice point \mathbf{r}' , can be chosen so that $0 \leq x_j, y_j, z_j \leq 1$. There are many ways of choosing the

crystal axes or cell for a given lattice. It follows from the above discussion that the primitive cell contains just a single lattice point. It is therefore in most cases desirable to work with a primitive cell. A non primitive cell is preferred in cases where it has a simple relation to the symmetry of the structure.²⁷

A crystal lattice can be mapped into itself by translation and various other *symmetry operations*. A typical operation is that of *rotation* n about an axis that passes through a lattice point. A lattice may have one-, two-, three-, four- and sixfold rotation axes that map it into itself. These correspond to rotations by, or by integral multiples of, 2π , $2\pi/2$, $2\pi/3$, $2\pi/4$ and $2\pi/6$, respectively. The rotation axes are denoted 1, 2, 3, 4 and 6. Another typical symmetry operation is *mirror reflection* m about a plane through a lattice point. The operation of combining a rotation n with a subsequent mirror plane m is termed an inversion \bar{n} . These three symmetry operations—translation, rotation and reflection—give a cell its *point group*. There are 32 different point groups.^{27,28}

2.1.2 Types of lattices

If a 3D lattice is to be invariant under one or more of the symmetry operations introduced so far, it imposes restrictions on the axes \mathbf{a}_i . There are five distinct lattice types in 2D and 14 in 3D. These distinct lattice types are termed *Bravais lattices*. The general lattice is triclinic, while the rest are grouped into systems classified by six types of cells which are monoclinic, orthorhombic, tetragonal, cubic, trigonal and hexagonal. The division into systems is determined by the relations between the axes \mathbf{a}_i , that is their lengths and the angles α, β, γ between them. The three Bravais lattices in the cubic system, together with the *face-centred cubic* (fcc) structure of yttrium hydride, can be seen in Fig. 2.1.^{27,29}

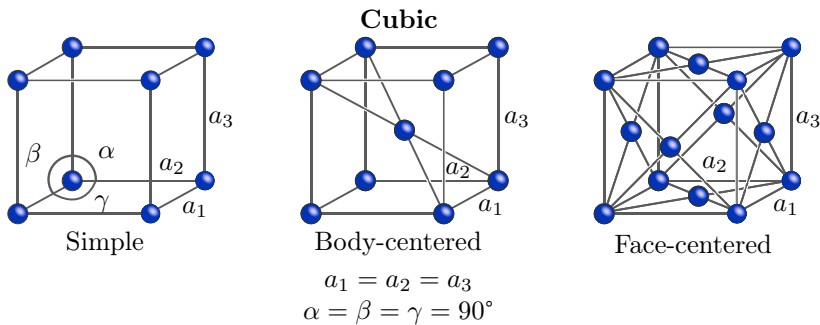


Figure 2.1: The three cubic Bravais lattices.

Combining the 32 point groups with the 14 Bravais lattices in 3D results in 230 different space groups.²⁹ A *space group* is some combination of the translational symmetry of a cell, the point group symmetry operations and the operations of *screw axes* and *glide planes*. The two latter are translation in combination with rotation and reflection, respectively. For diffraction techniques, as will be discussed in §2.2.1, it is important whether or not the crystals are centrosymmetric, i.e. contain an inversion centre so that for every point (x, y, z) in the cell there is an indistinguishable point $(-x, -y, -z)$. Since a diffraction experiment produces a projection of the lattice planes, the resulting reflection diagram must comprise the symmetry of the crystal structure. The intensities reflected at two opposite sides of the crystal planes are equal, hence diffraction

experiments are only able to distinguish between the various centrosymmetric crystal classes. These 11 so-called *Laue groups* containing an inversion centre are shown in Fig. 2.2 with their symmetry elements indicated. YH_2 belongs to the space group 225,³⁰ denoted $\text{Fm}\bar{3}\text{m}$, implying that it has the fcc structure, two non-equivalent mirror planes and a three-fold rotation-inversion axis along the cube diagonals. It also implies that it belongs to the Laue group $\text{m}\bar{3}\text{m}$.

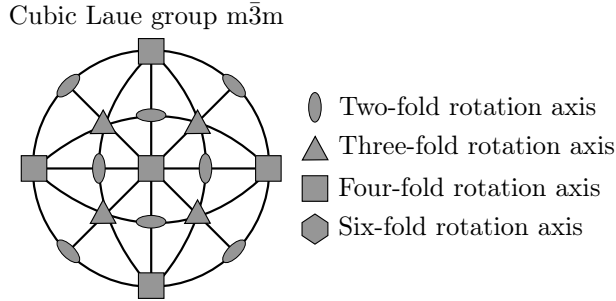


Figure 2.2: Symmetry elements in the cubic $\text{m}\bar{3}\text{m}$ Laue group with rotation operations indicated. Solid lines indicate mirror planes.

2.1.3 Index system for crystal planes

The notation concepts of *zone axes* and *Miller indices* are used for describing, respectively, directions and planes in crystals. A *zone* is defined as a set of planes or faces in a crystal whose intersections are all parallel. The common direction of the intersections is called a *zone axis*, and the axis must pass through the origin of a cell. The zone axis symbol is determined by expressing the fractions of a point's coordinates as whole numbers, for example [100]. Groups of crystallographically equivalent zone axes are denoted $\langle 100 \rangle$, this particular group encompassing both the positive and negative directions of the crystal axes \mathbf{a}_i in a cubic crystal. The *Miller index* of a plane is determined by the reciprocals of the intercepts of the plane on the crystal axes \mathbf{a}_i . The general indices are (hkl) , making the intercepts $a_1/h, a_2/k, a_3/l$ on the axes. The index is denoted with a bar \bar{h} when the interception is on a negative axis. Groups of crystallographically equivalent Miller indices are denoted $\{100\}$, this particular group representing the six faces of a cube. Examples of lattice planes in a cubic crystal, (111), (200), (220), (311), can be seen in Fig. 2.3. The *interplanar spacing* d_{hkl} in the case of a crystal with cubic axes $a_1 = a_2 = a_3 = a$ is given by

$$d_{hkl} = \frac{a}{\sqrt{h^2 + k^2 + l^2}}. \quad (2.3)$$

The definition of d_{hkl} in such a system is the distance between the cell origin and the plane (hkl) . Lattice planes and interplanar spacings form the basis for the concept of the reciprocal lattice and the Bragg law, the latter discussed in §2.2.1.²⁹

2.1.4 Reciprocal lattice

The *reciprocal lattice* represents the Fourier transform of the Bravais lattice. It provides a geometrical basis for understanding diffraction and the behaviour of electrons in crystals. The

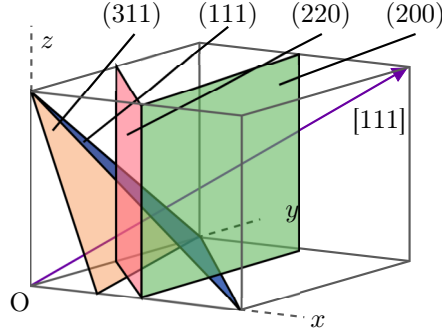


Figure 2.3: Description of directions and planes in a cubic crystal, relative to the origin O . The four planes indicated have Miller indices (111) , (200) , (220) and (311) . The $[111]$ plane normal is also indicated.

lattice can be defined by the points spanned by the set of vectors

$$\mathbf{G} = v_1 \mathbf{b}_1 + v_2 \mathbf{b}_2 + v_3 \mathbf{b}_3, \quad (2.4)$$

where v_i are integers. A vector \mathbf{G} of this form is a *reciprocal lattice vector*. The vectors \mathbf{b}_i are *primitive vectors of the reciprocal lattice* defined by

$$\mathbf{b}_1 = 2\pi \frac{\mathbf{a}_2 \times \mathbf{a}_3}{\mathbf{a}_1 \cdot \mathbf{a}_2 \times \mathbf{a}_3}; \quad \mathbf{b}_2 = 2\pi \frac{\mathbf{a}_3 \times \mathbf{a}_1}{\mathbf{a}_1 \cdot \mathbf{a}_2 \times \mathbf{a}_3}; \quad \mathbf{b}_3 = 2\pi \frac{\mathbf{a}_1 \times \mathbf{a}_2}{\mathbf{a}_1 \cdot \mathbf{a}_2 \times \mathbf{a}_3}. \quad (2.5)$$

The vectors \mathbf{b}_i are parallel to their real-space counterparts in systems where $\alpha = \beta = \gamma = 90^\circ$. In fact, the fcc reciprocal lattice and the *body-centred cubic* (bcc) real-space lattice are reciprocally related. It follows from geometrical considerations that when $(v_1, v_2, v_3) = (h, k, l)$ and \mathbf{G} is perpendicular to the plane (hkl) , the relation between the reciprocal lattice vector and the real-space interplanar spacing is

$$|\mathbf{g}_{hkl}| = \frac{2\pi}{d_{hkl}}, \quad (2.6)$$

where $\mathbf{g}_{hkl} = \mathbf{G} \parallel (hkl)$. A point on the reciprocal lattice hence corresponds to a unique interplanar spacing in real-space and thus represents a spatial periodicity, or *frequency*, in the crystal structure. The reciprocal lattice can in light of this relation be considered as the Fourier Transform (FT) of the crystal lattice.^{27,29}

While the Bravais lattice is infinite, a real crystal cannot be. As mentioned in the start of this section, a crystal can be constructed by first defining the lattice and then associating it, or more precisely convolving it, with the basis. To make it finite the convolving terms must also be multiplied with a step function to truncate the infinite structure. A result from Fourier analysis is that a short distance in real space corresponds to a long distance in reciprocal space. Hence, when considering a crystal which is ‘thin’ in some direction, its reciprocal points are elongated. The length of these *reciprocal-lattice rods*, or *relrods*, depends on how the crystal is truncated. As will be discussed in §2.2.1, these rods are prominent in diffraction patterns in the TEM due to the shape of the sample, or specimen.

2.1.5 Dislocations

No crystal is perfect, and a real crystalline material is prone to defects. A simple model states that every atom in a crystalline material is bound to the surrounding material by a certain energy W_b on the order of a few eV.³¹ At a finite temperature T there is a probability p of this atom acquiring a sufficient energy to move from its initial position to a neighbouring site, given as $p = e^{-W_b/k_b T}$, where k_b denotes the Boltzmann constant. The atom can jump to a vacant site or an interstitial site, i.e. in between normally occupied sites. Possible positions the atom can move to is determined by the crystal lattice. Atoms not inherent to the crystal structure, impurity atoms, will also cause defects. If they are similar in size to the inherent atoms, they tend to substitute these atoms. *Point defects* consist of only a single atom and are termed 1D defects. *Dislocations*, referred to as 2D defects, are extended regions of point defects. Dislocations greatly influence many material properties. Boundaries between adjoining crystals, or grains, consist of arrays of dislocations.²⁷ The (mis)orientation of grains in a polycrystalline material is covered in §2.4.

2.2 Transmission electron microscopy

The smallest distance between two points that our eyes can resolve is approximately 0.1 mm,³² and any instrument showing images that reveal details finer than 0.1 mm could be called a microscope. Rayleigh's criterion²⁸ states that the smallest, resolvable distance δ is given as

$$\delta = \frac{0.61\lambda}{n \sin \alpha}, \quad (2.7)$$

where λ is the radiation wavelength, n the refractive index of the viewing medium and α the semi-angle of collection of the magnifying lens. A visible-light microscope (VLM) can at best achieve $\delta \sim 300$ nm, corresponding to about 1 000 atom diameters. This renders the instrument insufficient to probe the nanostructure of materials, typically said to be structures smaller than 100 nm. However, these structures can be resolved using an electron microscope. In a TEM, a beam of electrons is transmitted through a specimen to form an image. The TEM is similar to the VLM in many ways, although there are notable differences which makes the TEM more powerful and complex. While the VLM uses visible light focused through curved glass lenses to collect a magnified image, the TEM focuses the electrons through magnetic lenses, apertures and deflectors. The TEM also records the image on a fluorescent screen or via a detector or a charge-coupled device (CCD) camera as a two-dimensional projection formed by electrons that have transmitted the sample.

Like all matter, electrons have properties of both particles and waves.³³ The momentum p of an electron with rest mass m_0 is related to its *De Broglie wavelength* λ through the Planck constant h as $\lambda = h/p$. By increasing the electron's velocity its effective wavelength is decreased, meaning it can resolve finer structures. The TEM imparts momentum to the electron by accelerating it through a potential drop V , giving it a kinetic energy eV, where e is the electron charge. The typical output energy range is 60-500 keV. At 200 keV the electron travels at approximately 0.7 times c , the speed of light in vacuum. Hence relativistic effects must be included in the theory

of electron scattering in a TEM. λ is then given as³²

$$\lambda = \frac{h}{\sqrt{2m_0eV \left(1 + \frac{eV}{2m_0c^2}\right)}}, \quad (2.8)$$

According to Eq. (2.8), a 200 keV electron has a wavelength of 0.002 51 nm, much smaller than the diameter of an atom. But unlike in a VLM where obtained resolutions approach that of applied wavelengths, obtainable resolutions in a TEM are much poorer than 0.002 51 nm due to the poor performance of the magnetic lenses. A modern, conventional TEM can experimentally achieve resolutions of $\sim 2 \text{ \AA}$ and $< 1 \text{ \AA}$ combined with aberration corrections C_s .³²

2.2.1 Electron scattering and diffraction

Since the electron has a low mass, a charge and a short wavelength, it can easily be deflected when passing close to the nucleus of an atom or its surrounding electron cloud. These electrostatic Coulomb interactions give rise to multiple scattering mechanisms and secondary signals when a high energy electron beam reacts with specimen. A common classification of electron-scattering phenomena are *elastic* and *inelastic* scattering, where the electron loses no energy in the former and some energy in the latter. Scattered electrons can also be *coherent* or *incoherent*, where two electrons are coherent if they are essentially in phase and of a fixed wavelength. Scattering is furthermore either *forward* ($< 90^\circ$) or *backward* ($> 90^\circ$), referring to the scattering angle, with respect to the incident beam and a specimen positioned normal to the beam. Examples of relations between these classifications are that elastic scattering is usually coherent if the specimen is thin and crystalline, and it generally leaves the specimen at relatively low angles of 1–10°. Also, inelastic scattering is mostly incoherent and leaves the specimen at very low angles of $< 1^\circ$.³²

A summary of the different signals originating from electron-matter interactions can be seen in Fig. 2.4. The size of the depicted tear drop shape of the *interaction volume* of electrons in a solid is dependent upon the energy of the incident beam and the atomic number and density of the solid. The average distance an electron travels between scattering events, known as its *mean free path*, is in the order of tens of nm in a solid due to the strong electron-matter interactions. Thus, specimens studied in the TEM cannot be much thicker than 200 nm to get a sufficient transmitted signal. Secondary electrons (SE) and backscattered electrons (BSE) are normally not detected in a TEM because the signals are weak. However, they contain topographical information about the specimen and are the primary signals in an SEM, discussed further in §2.3.³²

Scattering. The probability of an electron scattering elastically through an angle θ into a solid angle $d\Omega$ by the nucleus of an atom is governed by the *Rutherford differential cross-section*. The situation is illustrated in Fig. 2.5. When considering relativistic effects and effects of the electron cloud screening some of the Coulomb potential of the atomic nucleus, the cross-section is given as³²

$$\sigma(\theta) = \frac{Z^2\lambda^4}{64\pi^4a_0^2} \frac{d\Omega}{\left[\sin^2\left(\frac{\theta}{2}\right) + \frac{\theta_0^2}{4}\right]^2}. \quad (2.9)$$

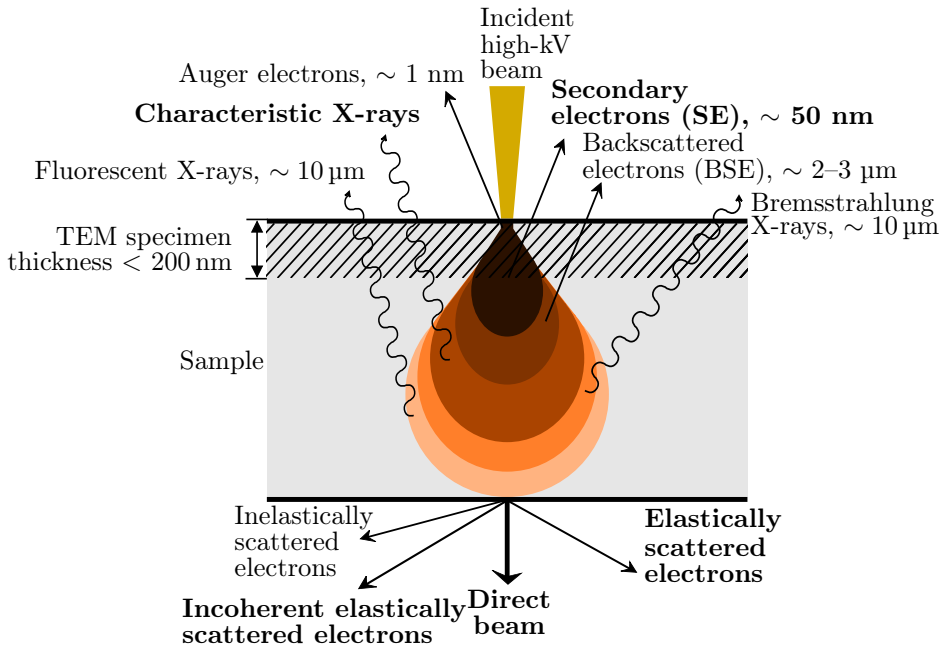


Figure 2.4: The interaction volume and the resulting signals from an incident high-kV electron beam in a specimen. The signals most relevant to this work are shown in bold. The typical TEM specimen thickness of $< 200\text{ nm}>$, although not to scale, is indicated.

Here, Z is the atomic number of the scatterer, λ is the relativistic wavelength of the electron as found in Eq. (2.8), $a_0 \approx 0.0529\text{ nm}$ is the Bohr radius and $\theta_0 = 0.117Z^{1/3}/E_0^{1/2}$, where E_0 is in keV. A derivation can be found in e.g. the standard TEM textbook by Williams and Carter.³² Eq. (2.9) is valid for TEM operating voltages $< 300\text{ kV}>$ and for elements with $Z < 30$ which scatter through smaller angles.

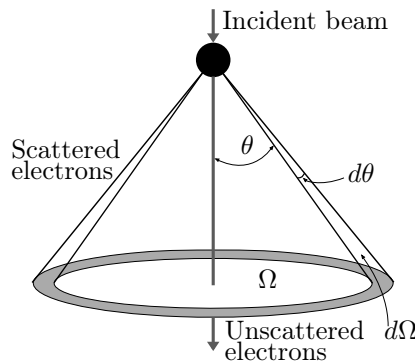


Figure 2.5: Electron scattering by a scattering centre. Electrons are scattered through an angle θ and the total solid angle of scattering is Ω .

Rutherford scattering is incoherent, while electrons scattered to lower angles $< 3^\circ$ are usu-

ally coherent. These are scattered by diffraction phenomena, and Eq. (2.9) is not valid for diffracted electrons because it does not account for the intensity of a scattered electron wave. The *atomic-scattering factor* $f(\theta)$ is a measure of the amplitude of an electron wave scattered from an isolated atom, and $|f(\theta)|^2$ is proportional to the scattered intensity. Its relation to the differential cross-section in Eq. (2.9) is given as

$$|f(\theta)|^2 = \frac{d\sigma(\theta)}{d\Omega}. \quad (2.10)$$

Based on the first Born approximation,³³ $f(\theta)$ can be related to the scattering factor f_X of X-rays as

$$f(\theta) = \frac{\left(1 + \frac{E_0}{m_0 c^2}\right)}{8\pi^2 a_0} \left(\frac{\lambda}{\sin(\theta/2)}\right)^2 (Z - f_X). \quad (2.11)$$

where f_X is defined as the FT of a scattering object. It is generally given as

$$f_X(\mathbf{K}) = \int_{-\infty}^{\infty} d^3\mathbf{r} \rho(\mathbf{r}) e^{i\mathbf{K}\cdot\mathbf{r}}. \quad (2.12)$$

Here, $\mathbf{K} = \mathbf{k}' - \mathbf{k}$ is the wave vector transfer between the incoming wave \mathbf{k} and the scattered wave \mathbf{k}' and $\rho(\mathbf{r})$ is the electron density of the scattering object as a function of the position \mathbf{r} relative to its centre. The differential cross-section in Eq. (2.9) and the atomic-scattering factor for electrons in Eq. (2.11) govern complementary scattering mechanisms, and are the primary origins of contrast in the TEM. But while the latter predicts how electrons scatter on isolated atoms, the collective, coherent scattering by a collection of atoms emerging from a specimen in the TEM can only be understood by discussing the principle of diffraction.

Diffraction. When an electron beam is incident on a crystal, the waves diffracted from all atoms in the lattice interfere. If the path difference for plane waves reflected from adjacent atomic planes is $2d_{hkl} \sin \theta$, where θ is measured from the plane, constructive interference from successive planes occurs when the path difference is an integral number n of wavelengths λ , so that

$$2d_{hkl} \sin \theta = n\lambda. \quad (2.13)$$

This is the *Bragg law*, only satisfied when $\lambda \leq 2d_{hkl}$. The situation can be seen in Fig. 2.6 (b). The law is useful in giving a physical picture of the constructive-interference phenomenon. Still, the picture is wrong since the waves are not reflected. A definition that gives a more precise, physical understanding of diffraction is the reciprocal space equivalent of the Bragg law. The situation can be seen in Fig. 2.6 (c), where an incoming plane wave scatters on two objects separated by some \mathbf{r} . A scattered wave is generated, interfering constructively when the path difference equals an integral number n of wavelengths λ , given as³²

$$\mathbf{r} \cdot \mathbf{K} = 2\pi n = \mathbf{r} \cdot (\mathbf{g}_{hkl} + \mathbf{s}). \quad (2.14)$$

These are the *Laue conditions*, where \mathbf{K} is the wave vector transfer and \mathbf{g}_{hkl} is the reciprocal lattice vector defined in Eq. (2.6). The *excitation error* $\mathbf{s} = \langle s_x, s_y, s_z \rangle$ denotes the small deviations, parallel to the incident beam direction \mathbf{k} , from the Bragg condition which still give

diffraction spots.

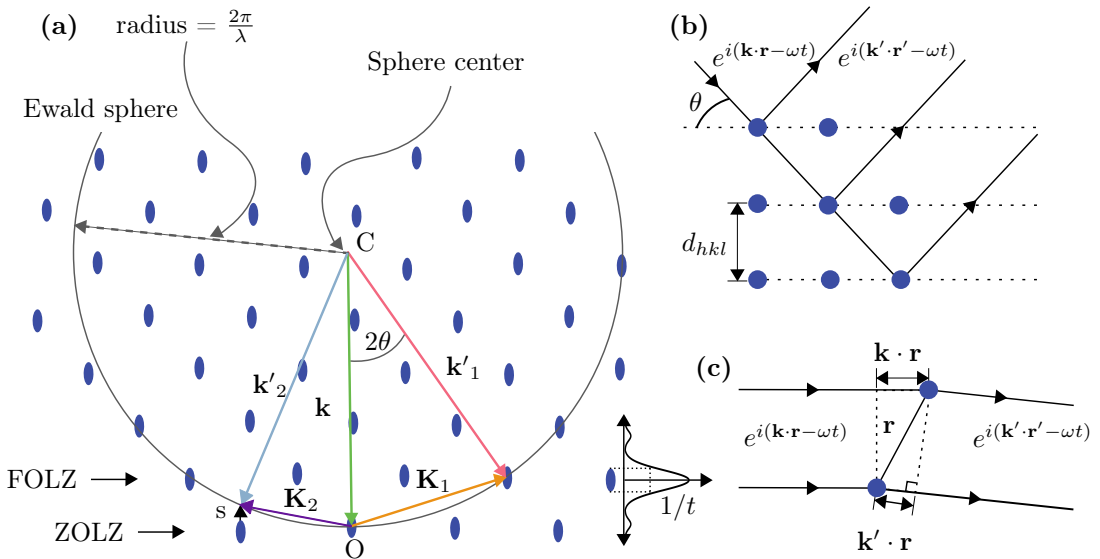


Figure 2.6: (a) The Ewald sphere construction for elastic scattering in a crystal, and (b) the Bragg and (c) Laue approaches to scattering interference. The Ewald sphere radius in (a) is not on scale.

Each point on the reciprocal lattice in a thin TEM specimen is associated with a relrod centred on the point, as mentioned in §2.1. The relrods are normal to the specimen, but have a finite thickness parallel to the specimen normal. A sphere of radius $k = 2\pi/\lambda$ can be constructed so that when it cuts through a lattice point in the lattice, the set of planes corresponding to that point satisfy the Bragg condition. Hence, those planes will diffract strongly. This construction is called the *Ewald sphere*, and the key feature is that since there are rods on each point in a thin specimen, a somewhat weaker diffraction spot is still observed even though the Bragg condition is not satisfied. The construction in two dimensions can be seen in Fig. 2.6 (a). The sphere is a visualisation of the Laue conditions in Eq. (2.14). In the TEM the point O represents the direct beam and the origin of the reciprocal lattice. \mathbf{k}' can be any vector beginning at C and ending on the sphere. The wavelength of electrons in the incident beam in a TEM is as mentioned ~ 0.00251 nm for 200 keV electrons, giving an Ewald sphere radius of 2500 nm^{-1} . So the sphere surface is almost planar, many relrods are intersected and many lattice planes satisfy the diffraction conditions in Eq. (2.14). When the row of reciprocal lattice points is essentially perpendicular to the incident beam, a plane through this row crossing the point O is called the zero-order Laue zone (ZOLZ). The planes of points which are parallel to the ZOLZ but do not contain O are thus termed first-order Laue zone (FOLZ), second-order Laue zone (SOLZ) and higher-order Laue zones (HOLZ). From Fig. 2.6 (a) it can be seen that the wave \mathbf{k}'_1 scatters on the FOLZ.³² Fig. 2.7 shows a ring diffraction pattern of gold nanoparticles (Au), typical of polycrystalline materials consisting of small crystals, and a ‘regular’ pattern from a single silicon (Si) crystal.

The observed intensity of a diffraction spot is proportional to the square of the modulus of the

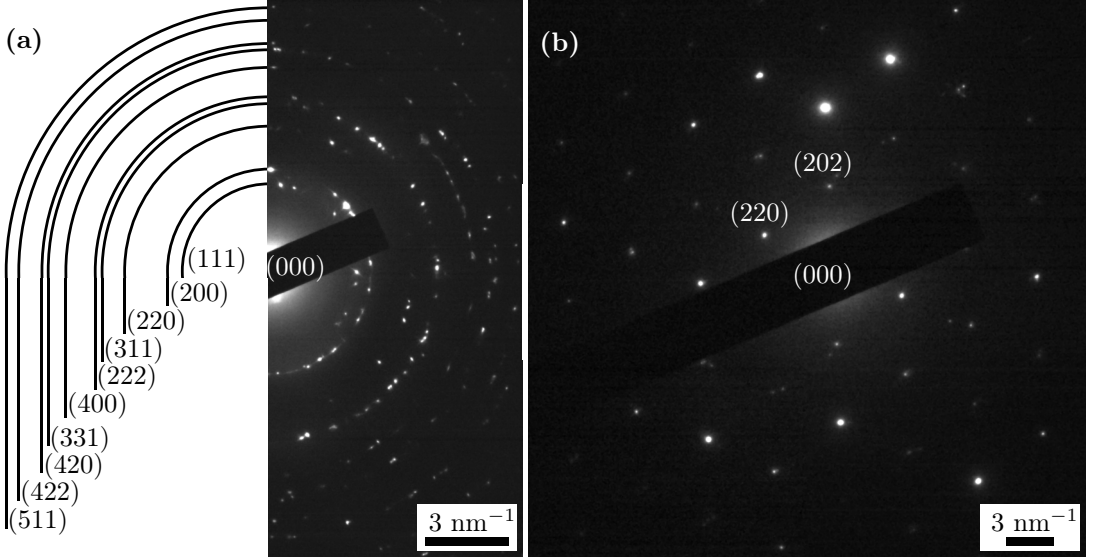


Figure 2.7: Electron diffraction patterns from multiple Au nanoparticles (a) with different orientations resulting in a ring pattern, and from a single Si crystal (b). The direct beam (000) is blocked by a beam stopper. The Si crystal is viewed along its $[\bar{1}11]$ direction, evident by the pattern's three-fold symmetry. Both structures belong to the cubic Laue group $m\bar{3}m$.

crystal structure factor as²⁷

$$I \propto |F_{\text{crystal}}(\mathbf{K})|^2. \quad (2.15)$$

F_{crystal} is found by expanding the atomic-scattering amplitude $f(\theta)$ in Eq. (2.12) to the lattice cell giving

$$F_{\text{crystal}}(\mathbf{K}) = \sum_{\{\mathbf{r}'+\mathbf{r}_j\}} f_j(\mathbf{K}) e^{i\mathbf{K}\cdot(\mathbf{r}'+\mathbf{r}_j)} = \sum_{\mathbf{n}} e^{i\mathbf{K}\cdot\mathbf{r}'_{\mathbf{n}}} \sum_j f_j(\mathbf{K}) e^{i\mathbf{K}\cdot\mathbf{r}_j}. \quad (2.16)$$

F_{crystal} is defined as the amplitude of waves scattered by the crystal at unit distance in the direction $\mathbf{k} + \mathbf{K}$. In Eq. (2.16) $\mathbf{r}'_{\mathbf{n}}$ is any lattice point as defined in Eq. (2.1) and \mathbf{r}_j is the position of atom j of the basis in the cell as defined in Eq. (2.2). Hence, the two sums on the right are the convolution of the individual structure factors F_{lattice} and F_{cell} . When the diffraction condition $\mathbf{K} = \mathbf{g}_{hkl}$ in Eq. (2.14) is satisfied, F_{cell} becomes

$$F_{\text{cell}} = \sum_j f_j(\mathbf{g}_{hkl}) e^{2\pi i(hx_j + ky_j + lz_j)}. \quad (2.17)$$

In the case of the fcc structure with four atoms in the cell with coordinates $(0, 0, 0)$, $(\frac{1}{2}, \frac{1}{2}, \frac{1}{2})$, $(\frac{1}{2}, 0, \frac{1}{2})$ and $(0, \frac{1}{2}, \frac{1}{2})$, F_{cell} becomes

$$F = f \{1 + e^{\pi i(h+k)} + e^{\pi i(h+l)} + e^{\pi i(k+l)}\}. \quad (2.18)$$

The value of F is zero whenever the sum of the exponentials is -1 , which is whenever one of

the indices h, k or l is odd but the other two are even, or vice versa. Therefore

$$\begin{aligned} F &= 4f \quad \text{if } h, k, l \text{ are all even or all odd,} \\ F &= 0 \quad \text{if } h, k, l \text{ are mixed even and odd,} \end{aligned}$$

which are the *structure-factor rules* for the fcc crystal structure. They determine which reflections are allowed in a diffraction pattern (DP). They also assign a weight (which might be zero) to each of the points in the reciprocal lattice, corresponding to the intensity observed for each reflection in a DP.³²

In further considerations of the observed intensity of a diffraction spot, the structure factor F_{lattice} in Eq. (2.16) can be expanded by substituting $\mathbf{K} = \mathbf{g} + \mathbf{s}$ from Eq. (2.14) to get

$$F_{\text{lattice}} = \sum_{\{hkl\}} e^{-i\mathbf{s} \cdot \mathbf{r}'_{hkl}}. \quad (2.19)$$

Since only small excitation errors \mathbf{s} are considered, the phase $(-i\mathbf{s} \cdot \mathbf{r}'_{hkl})$ varies slowly in moving through the crystal and can therefore to a good approximation be replaced by an integral over the crystal volume $V = L_1 L_2 L_3$.³³ By applying geometrical considerations while keeping in mind that the lateral dimensions of a TEM specimen far exceeds its thickness t , the total diffracted intensity by a thin foil is found to be

$$I(\mathbf{s}) = |F_{\text{cell}}|^2 \cdot |F_{\text{lattice}}|^2 = \frac{L_2 L_3 |F|^2}{V_{\text{cell}}^2} \left(\frac{\sin \pi t s_x}{\pi s_x} \right)^2 \delta(s_y) \delta(s_z). \quad (2.20)$$

Eq. (2.20) shows the intensities in a DP spread out in the form of a spike normal to the thin foil. The result is also the well-known diffracted intensity distribution in optics of light from a slit of width t . Following the discussion in §2.1 on re rods, this finite distribution of scattered intensity can in the Ewald sphere construction be represented by extending each reciprocal lattice point in the direction normal to the crystal by a length $1/t$, as shown in Fig. 2.6 (a). Eq. (2.20) can furthermore be used to calculate the absolute intensity of a diffracted beam emerging from the TEM specimen, by considering the total intensity scattered into the solid angle $d\Omega$ about the beam. A complete derivation can be found in Ref. 33, the result being the intensity scattered through 2θ (see Fig. 2.6) in the g^{th} diffracted beam from a crystal of thickness t given as

$$I_g(t) = \left(\frac{\pi}{\xi_g} \right)^2 \left(\frac{\sin \pi t s}{\pi s} \right)^2. \quad (2.21)$$

s_x is replaced by s , the component of \mathbf{s} normal to the thin foil. ξ_g is the material dependent *extinction distance* with units in length given as

$$\xi_g = \pi k V_{\text{cell}} \cos \theta / F(2\theta), \quad (2.22)$$

where k is the magnitude of the incident beam. The intensity at the fully satisfied Bragg condition $s = 0$ is

$$I_g(t) = \left(\frac{\pi t}{\xi_g} \right)^2, \quad (2.23)$$

which cannot be greater than unity, the incident beam intensity. Hence, $t_{\text{max}} = \xi_g / \pi$ is the

upper limit of the foil thickness for which kinematical diffraction theory is valid at the Bragg position. $t_{\max} \approx 100 \text{ \AA}$, with typical extinction distances of a few hundred \AA , can be considered an upper limit since kinematical theory assumes a single scattering event. Even though for large deviations s , I_g from Eq. (2.21) may be small and kinematical theory may still be usefully applied, a dynamical theory including multiple scattering must be used. A simple interpretation is that the beam, which has been strongly Bragg diffracted once, is necessarily in the perfect Bragg orientation to be diffracted back into the direct beam by the same set of planes.³² The likelihood of this process occurring will increase with specimen thickness. In this *two beam* dynamical theory the diffracted intensities from a perfect crystal at the Bragg position $s = 0$ are

$$I_0(t) = \cos^2(\pi t/\xi_g), \quad (2.24)$$

$$I_g(t) = \sin^2(\pi t/\xi_g), \quad (2.25)$$

where $I_0(t)$ is the transmitted intensity. Both intensities now only vary with specimen thickness, and the interchange of intensity between the two beams is analogous to the energy interchange of two coupled simple harmonic oscillators. This interchange alters the intensity distribution in the diffraction plane, one consequence being that some reflections kinematically forbidden by the structure-factor rules can still be present in the DP. Further discussions on the intricate and extensive dynamical theory of diffraction can be found in e.g. the books by Williams and Carter³² or by Humphreys.³³

2.2.2 Microscope design

The following is a discussion on the electron beam path in the TEM, as is shown in Fig. 2.8, while details on the contrast mechanisms and different operation modes are discussed in §2.2.3.

The two common electron sources are a field-emission gun (FEG) with a tungsten (W) filament and a thermionic gun with a lanthanum hexaboride (LaB_6) filament. The intensity per solid angle, i.e. brightness, and the coherency of the electrons leaving the filament of a FEG is generally superior to the thermionic gun. However, since the filament tip of a FEG is smaller than in a thermionic gun, it cannot image as large areas. Therefore, a FEG is preferable when acquiring phase contrast images, while a thermionic gun is preferable when doing amplitude contrast imaging.³²

The lenses in a TEM are electromagnetic pole pieces generating a nearly symmetric, variable magnetic field around the optic axis, focusing the electrons through the Lorentz force in a helical motion. A lens' focal length can be altered by changing its strength. Although magnetic, the lenses are comparable to refractive lenses in regular optical microscopes, so most of the terminology and theory of electron propagation in a TEM is based on light optics.³² All lenses in a TEM suffer from aberrations and astigmatism, and electrons passing a lens far from the optic axis are more affected by lens defects than electrons passing closer to the optic axis.

The *condenser lenses* (C1, C2) as seen in Fig. 2.8 can form either a parallel or convergent beam. The first crossover is an image of the electron source and acts as the object for the first condenser lens (C1). When forming a parallel beam, as needed in the selected-area diffraction (SAD), bright-field (BF) and dark-field (DF) TEM modes, the second condenser lens (C2)

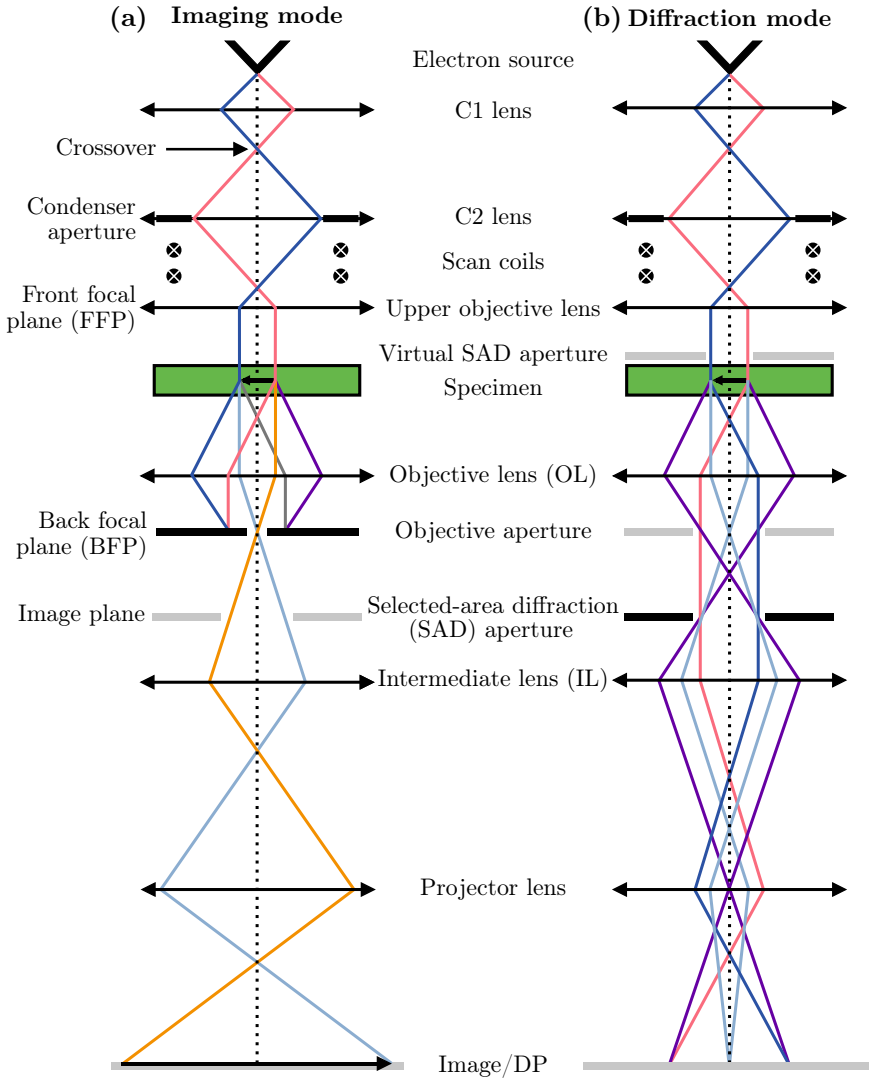


Figure 2.8: Simplified diagrams of ray propagation in the TEM. In imaging mode (a) the objective aperture selects the non-diffracted electrons to form the final image on the viewing screen/CCD camera. In diffraction mode (b) the electrons leaving the specimen at a certain angle are selected by the SAD aperture and focused to a specific point in the BFP of the OL. The BFP then acts as the object plane for the IL and the DP is projected onto the viewing screen/CCD camera.

creates an image of the crossover in the *front focal plane* (FFP) of the upper *objective lens* (OL). When forming a convergent beam, as needed in the scanning TEM (STEM) and convergent beam electron diffraction (CBED) modes, C2 creates this image on the specimen rather than in the FFP. A condenser aperture in the plane of C2 controls both the electron current on the specimen and the semi-angle of convergence α . Astigmatism, arising when the beam is not perfectly round, is corrected for by the stigmator lenses, not shown in the figure. The scan coils

translate or tilt the beam off the optic axis so it impinges on the specimen at a specific angle. This is essential e.g. when creating a scanning beam for STEM imaging, scanning precession electron diffraction (SPED) or performing centred DF imaging.³²

The *specimen stage* clamps the specimen holder in the correct position, so the OL can form images and DPs from the electrons emerging from the exit surface of the specimen in a reproducible manner. They are then magnified by the imaging system, as can be seen in Fig. 2.8. Most specimen holders can be tilted both parallel and orthogonal to their axes. To achieve reproducibility from session to session, a standard reference value for the OL current is desired. For the image to be in focus, this standard value imposes a reference plane for the specimen to be in, known as the *eucentric plane*. If the specimen is in this plane, a point on the optic axis does not move laterally when tilting the specimen.³²

After the OL has dispersed the electrons exiting the specimen it creates a DP in its *back focal plane* (BFP), as seen in Fig. 2.8. The imaging system can then be adjusted to either use the OL's BFP as the object plane for the *intermediate lens* (IL), or use the OL's image plane as the IL's object plane. In this way either a DP or an image of the specimen is projected onto the viewing screen/CCD camera. In diffraction mode an SAD aperture is inserted into the image plane of the OL to select electrons leaving the specimen at a certain angle to form the final DP. In imaging mode an objective aperture is inserted into the BFP of the OL to form the final image.³²

A vacuum pressure of typically $\sim 1 \times 10^{-5}$ Pa, ten orders of magnitude lower than the atmospheric pressure, is needed inside the TEM column. This is because electrons are strongly scattered by atoms, and a higher pressure will lead to a decreased electron current reaching the specimen. The vacuum also plays a role in keeping the specimen clean from contamination, typically hydrocarbons and water vapour.³²

2.2.3 Operation modes

The TEM is a versatile instrument as it can image structurally and crystallographically different domains in a specimen by DF imaging, obtain crystal orientation and phase maps by SPED, acquire phase-contrast images by high-resolution TEM (HRTEM), determine the chemical composition by energy-dispersive X-ray spectroscopy (EDS) and probe the electron configuration of elements by electron energy loss spectroscopy (EELS), all from the same region on a specimen. The following is a discussion of the contrast mechanisms and operation modes applied in this work.

Electrons travelling through a specimen may get their amplitudes and phases changed, giving rise to the two distinct types of contrast in a TEM, namely amplitude contrast and phase contrast. *Amplitude contrast* results from variations in mass, thickness or a combination of the two, or from regions of the specimen diffracting electrons differently. This contrast can in the TEM mode be promoted by inserting an OA in the BFP of the OL, i.e. where the DP is formed. Similarly can this contrast in the STEM mode be promoted by detectors rather than apertures. Now either scattered or unscattered coherent electrons can be selected to form an image. It is important to consider that while a small aperture will enhance the contrast, it might decrease the resolution. *Phase contrast* arises from the interference between scattered and unscattered beams and is the basis of HRTEM. This contrast is promoted by allowing more beams to form

an image.³²

Bright-field TEM. Selecting only the electrons scattered less than typically 10 mrad with an objective aperture results in a BF image. Regions of a specimen that scatter strongly will appear dark and regions that scatter less will be brighter. The greater the mass or density of a region, that is the higher the atomic number Z , the more it will scatter according to the Rutherford cross-section in Eq. (2.9). A thicker region will likewise lead to more scattering than a thinner region. This is called *mass-thickness* contrast. How much a region diffracts the electrons also contributes to the contrast in a BF image. Fig. 2.8 (a) shows a simplified diagram of a ray propagation forming a BF image.³²

Dark-field TEM. Selecting one of the diffracted spots in a DP, that is coherently scattered electrons, with an objective aperture results in a DF image with a strong intensity contrast. Now one or multiple specific spatial frequencies form the image. This method is powerful when studying structure or orientation domains in a specimen because these domains may diffract electrons to separate reflections in a DP. Forming a DF image of such a reflection may then show the shape and size of the diffracting domain. To avoid astigmatism in the DF image, the incident beam can be tilted so it hits the specimen at an angle equal and opposite to the scattering angle, leading the selected electrons to travel down the optic axis in what is known as centred DF imaging.³² Diffraction contrast can produce thickness fringes and *bending contours* in a DF image. Whether the Bragg condition is fulfilled or not will vary with the specimen bending. Crystal planes parallel to the incident beam will appear dark in the image, but bending can create a gradual transition to planes fulfilling the Bragg condition. It is also evident from Eq. (2.21) that the intensity changes with the deviation parameter s , causing such contours in the image. Another result of Eq. (2.21) is that the intensity varies with sinus squared of the thickness, causing *thickness fringes*. The periodicity of the fringes is related to the extinction distance ξ_g .

Diffraction. As mentioned in §2.2.2 will an SAD aperture select electrons diffracted to a certain angle to form a DP on the viewing screen/CCD camera when in SAD mode. The ability to easily switch between these two modes of operation is a great advantage of the TEM. Fig. 2.8 (b) shows a simplified diagram of a ray propagation forming a DP.³² In *nanobeam diffraction* (NBD) mode, the condenser lenses create a nearly parallel probe on the specimen, with typically a diameter of a few nanometres and a semi-convergence angle $\alpha < 1.5$ mrad.³⁴ The smaller the probe, the lower the current available and the higher the brightness needed to provide a reasonable current. It is therefore common to use a high-brightness FEG microscope when performing NBD. The perhaps biggest advantage over SAD is that the small probe allows for illumination of an individual nanostructure, like a single grain in a polycrystalline material, and a reduced background in the DP from the surrounding material. When using a condenser aperture with a small α , the recorded DP spots are expanded into small featureless disks with uniform intensity. NBD is considered to be a coherent form of CBED. CBED uses an α in between the ones used in the NBD and STEM modes. The connection between NBD and CBED is illustrated in Fig. 2.9. By considering the incident plane-wave components of the illumination to be incoherently related, the features within the expanded diffraction disks can be related to dynamical scattering, and a wide array of quantitative information can be obtained. Examples

include specimen thickness, unit cell determination and 3D crystal symmetry.

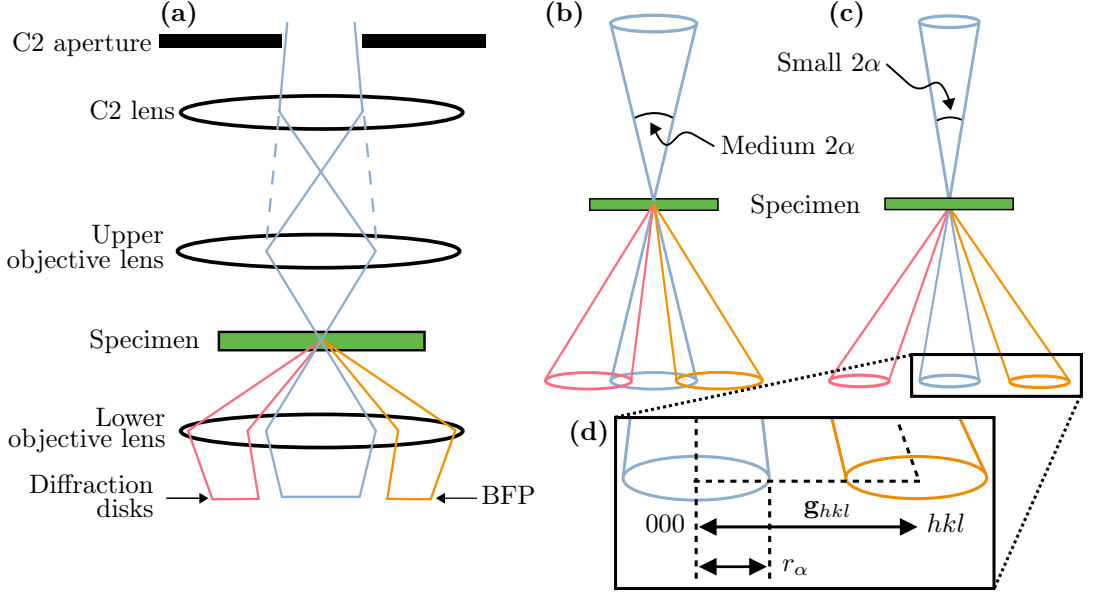


Figure 2.9: Ray diagram (a) of CBED pattern formation in TEM, and STEM mode with the C2 lens relaxed (dotted line). The convergent beam at the specimen results in the formation of disks in the BFP of the OL. Decreasing the C2 aperture size causes the CBED pattern to change from overlapping (b) to non-overlapping (c) disks, approaching the conditions used in NBD. The diffraction disk geometry (d) with the disk radius r_α and reciprocal lattice vector \mathbf{g}_{hkl} .

High-resolution TEM. An HRTEM image is the result of electron beams diffracting differently, enabling studies of very fine structures. In general no objective aperture is used so as to collect as many beams as possible to form the image. The image intensity varies sinusoidally with a periodicity related to \mathbf{g}^{-1} , hence the distance between the interference peaks is related to the interplanar spacing d_{hkl} . Therefore can a *Fast* FT (FFT) of such an image give information on the periodic structures these frequencies originate from. Lattice fringes can be seen as bright spots on a dark background in the image if the specimen is aligned along a zone axis. The information transferred from the specimen to the image is described by the *transfer function*³²

$$T(\mathbf{u}) = A(\mathbf{u})E(\mathbf{u})2 \sin \chi(\mathbf{u}), \quad (2.26)$$

where \mathbf{u} is the reciprocal lattice vector. $A(\mathbf{u})$ represents the apertures, $E(\mathbf{u})$ the attenuation of the wave and $2 \sin \chi(\mathbf{u})$ expresses the lens aberrations. The term $\chi(\mathbf{u})$ is the phase distortion function approximated as³²

$$\chi(u) = \pi \Delta f \lambda u^2 + \frac{1}{2} \pi C_s \lambda^3 u^4, \quad (2.27)$$

where Δf is the defocus value of the OL, λ is the applied electron wavelength and C_s is the lens quality or *spherical aberration*. The transfer function is derived from the weak phase-object

approximation which states that there is a linear relationship between the image and the weak specimen potential.³² However, this assumption is only true for the thinnest TEM specimens. Fig. 2.10 (a) shows a comparison of transfer functions for two different Δf , where $T(\mathbf{u}) < 0$ indicates positive contrast where atoms are *represented* by dark spots. The transfer function can be optimised by balancing the effect of spherical aberration against a particular negative defocus value known as the Scherzer defocus, occurring at

$$\Delta f_{\text{Sch}} = -1.2(C_s\lambda)^{1/2}. \quad (2.28)$$

At this defocus value all the beams will have nearly constant phase out to the ‘first crossover’ of the x -axis, denoting the ‘instrumental resolution limit’. Only for values below this point can dark spots be intuitively interpreted as atoms. The ‘information retrieval limit’ is defined as where $T(\mathbf{u})$ approaches zero.³²

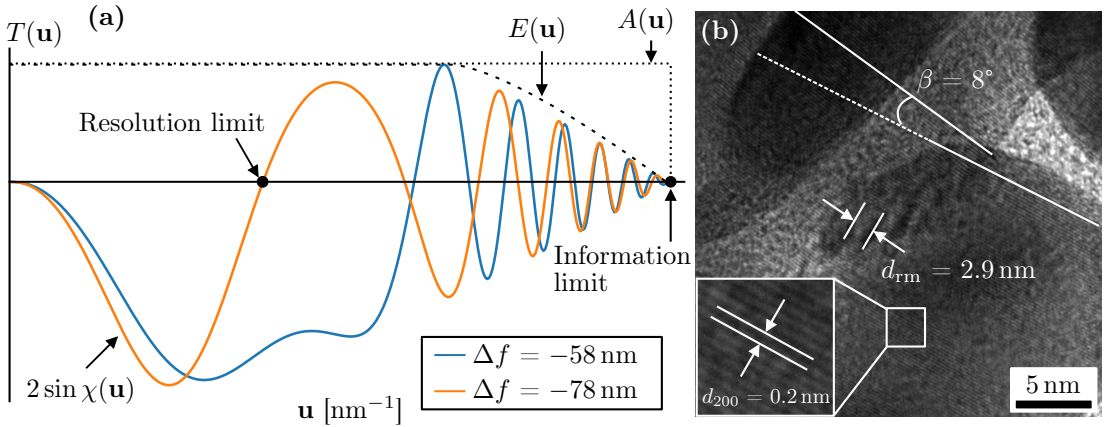


Figure 2.10: Comparison of two transfer functions (a) $T(\mathbf{u})$ (see Eq. (2.26)) with $\lambda = 0.00251 \text{ nm}$, $C_s = 1 \text{ mm}$ and two defocus values $\Delta f = -58 \text{ nm}$ and $\Delta f = -78 \text{ nm}$. Where $T(\mathbf{u})$ crosses the x -axis for the first time represents the point-to-point resolution, while the information limit is where it approaches zero. An HRTEM image (b) demonstrating rotational moiré fringes from two overlapping Au nanoparticles where Eq. (2.30) is used.

So-called *moiré fringes* arise when two sets of lattice planes have nearly common periodicities, corresponding to the lattice spacings of the interfering planes. The two fundamentally different types of interference are the translational moiré g_{tm} where $g_1 \neq g_2$ and rotational moiré g_{rm} where $g_1 = g_2$, respectively given by

$$d_{\text{tm}} = \frac{1}{g_{\text{tm}}} = \frac{d_1}{1 - d_2/d_1}, \quad (2.29)$$

$$d_{\text{rm}} = \frac{1}{g_{\text{rm}}} = \frac{d}{2 \sin \beta/2}. \quad (2.30)$$

Fig. 2.10 (b) show an HRTEM image of rotational moiré fringes from two Au nanoparticles rotated 8° relative to each other.

Scanning TEM. In STEM mode unlike in normal TEM mode, the electron beam is focused to a fine spot which is then scanned over the specimen in a raster to form the image. The beam produces a CBED pattern as shown in Fig. 2.9 in each probe position. The raster scanning is performed by deflection scan coils arranged below the condenser lens. This enables a variety of signals to be detected and plotted as a function of probe position, forming a magnified image directly correlated to quantitative data. Modes using transmitted electrons that leave the specimen at relatively low and high angles with respect to the optic axis are respectively referred to as BF imaging and *annular* DF (ADF) imaging. Element analysis in a point, line or region can be done by collecting either X-rays generated from electron excitations (EDS), or by collecting transmitted electrons that lost a measurable amount of energy as they passed through the specimen and forming a spectrum of them as a function of the energy lost (EELS).³⁵

A schematic of the STEM detector setup is shown in Fig. 2.11. A small detector on the optic axis collects the intensity from coherently scattered electrons, analogous to inserting an objective aperture in the TEM DP and only allowing the direct electrons into the imaging system. Both setups enhances phase contrast, giving BF imaging. An objective aperture is also commonly used in BF STEM to minimise lens aberrations. An annular detector centred on the optic axis at angles 10–50 mrad can be translated parallel to the axis by varying the camera length to collect a desired range of incoherently scattered electrons. This leads to ADF imaging. The intensity per probe position is now strongly dependent on the specimen thickness and the atomic number Z at that position. Moving the detector to higher angles > 50 mrad thus fully excluding coherent electrons enhances the compositional Z -contrast, and leads to *high-angle* ADF (HAADF) imaging.^{32,35}

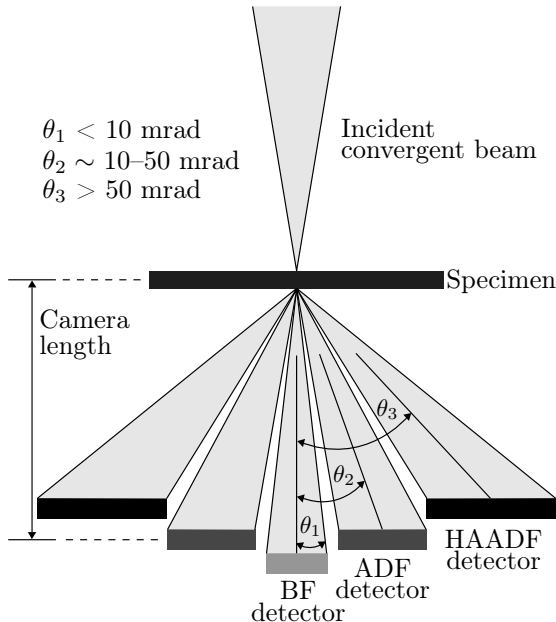


Figure 2.11: Simplified schematic of the STEM detector setup. The angular detection range of the ADF detector can be varied by varying the camera length.

Post-specimen optics can control the angles subtended by the detectors, but play no part in

the image formation process. Hence, the image resolution is not limited by aberrations in the imaging lens, only by the aberrations and dimensions of the beam probe. As with NBD and CBED it is common to use a high-brightness FEG microscope for STEM imaging.^{32,35}

Scanning precession electron diffraction. Precession electron diffraction (PED) is a specialised method to collect localised DPs in the TEM. A convergent beam is precessed around the optic axis at a constant *precession angle* ϕ and *precession frequency* ω as the DP is recorded.³⁶ A schematic ray diagram for PED with ϕ and ω indicated can be seen in Fig. 2.12 (a). The electron beam is rocked in a hollow cone above the specimen and then de-rocked below.

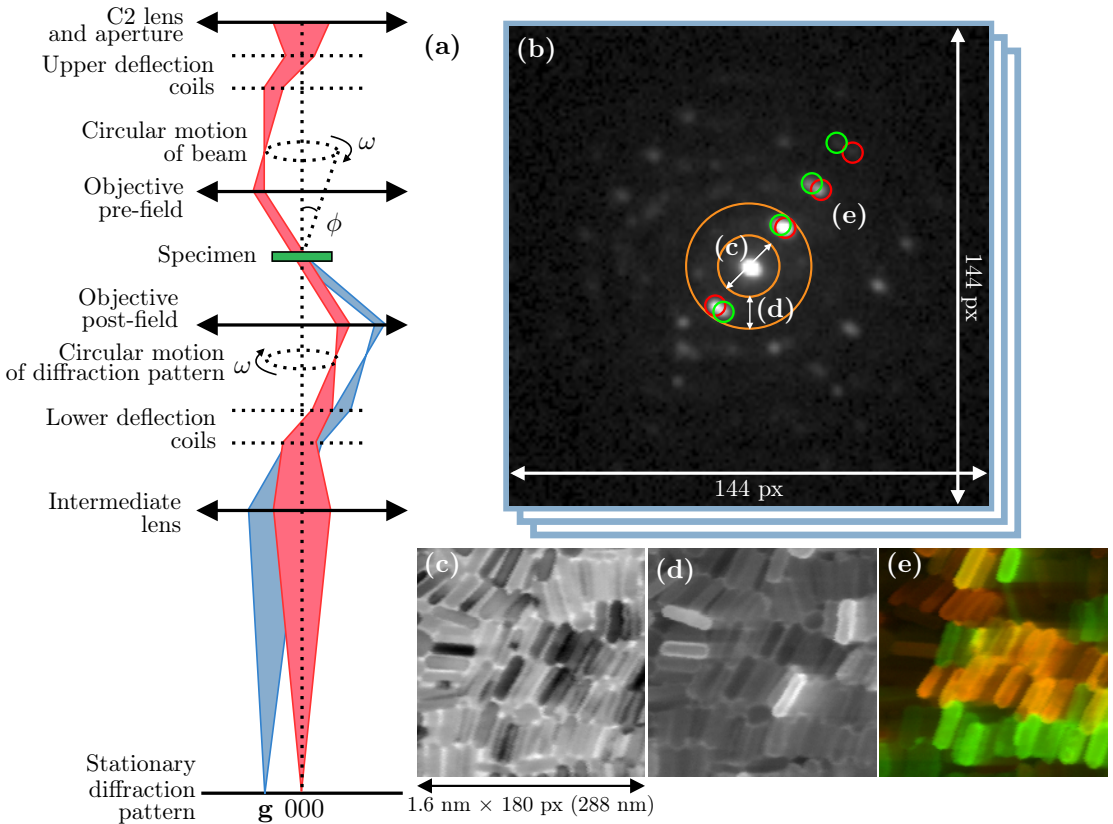


Figure 2.12: Schematic ray diagram (a) in PED mode, adapted from Midgley et. al.³⁷ One DP (b) is acquired per position when the precessing probe is scanned across an area of interest in SPED mode, resulting in a stack of DPs. Intensities in the DP stack can be integrated inside a virtual aperture and annulus to form respectively a VBF image (c) and a VDF image (d) of the Au specimen. The arrows in (c) denotes the scan size as well as the fast scan direction to the right. Two VDFs (e), each formed by summing intensities inside four virtual apertures (red or green), can also be summed to show overlapping features (yellow). The sizes of the scan (c) and DP (b) are indicated.

The hollow cone rocking motion of the beam can be translated to a similar motion of the Ewald sphere.³⁶ The sphere excites different reflections during its rocking motion, effectively ‘integrating’ the intensity over a range of angles that include the Bragg condition. This overall

intensity is the only relevant parameter for a particular reflection, and it also follows that the resultant pattern is composed of more reflections than would be the case for an unprocessed beam. Even though individual intensities are not kinematic, the ensemble of intensities in a PED pattern shows reduced dynamical effects.³⁷ This reduction eases the identification of orientations and phases when compared to simulated patterns, as these are simulated assuming kinematical diffraction. This crystallographic *template matching* is explained in §3.4.4.

By scanning the precessing probe, DPs can be acquired pixel-by-pixel to form a four-dimensional (4D) SPED data set in which 2D reciprocal information is available at each 2D real space position.³⁸ One such DP, acquired by a camera mounted externally to the TEM column looking at the viewing screen, is shown in Fig. 2.12 (b), from a data set of gold (Au) nanoparticles³⁹ acquired to illustrate the SPED technique and texture and grain size analysis. The technique has been developed primarily to complement EBSD⁴⁰ in an SEM to provide orientation and phase information at the nanometre scale in the form of overall grain structure, texture, strain etc. Virtual BF (VBF) or virtual DF (VDF) images can be formed by integrating intensities inside virtual apertures or annuli in the DP stack, as shown in Fig. 2.12 (b-e). Overlapping features can be studied by considering the sum of e.g. two VDF images as shown in Fig. 2.12 (e). A large precession angle ϕ is desirable to obtain clear PED patterns with as many reflections as possible. However, this may limit the achievable angular resolution in the determination of the orientation of the reflecting crystal. As a compromise a typical ϕ of 0.5° is chosen.⁴¹ Other notable parameters affecting the resolution apart from the precession angle and frequency are the probe size, semi-convergence angle α , probe position dwell time, camera length L and probe step size. A smaller probe increases the spatial resolution, but reduces the recorded intensity such that a larger dwell time should be used. Depending on the dwell time and the quality of the viewing screen, reflections recorded from one probe position can carry over to the next, hence adding noise to the recorded DPs. This can lead to so-called afterglow, evident in the upper right corner of Fig. 2.12 (e). Using a smaller L means probing a larger part of reciprocal space which might improve the template matching, but it will also reduce angular resolution due to the inherent limitation of available detector pixels. Using a smaller step size will also increase the spatial resolution, but will additionally lead to longer acquisition times and data sets of larger size.

Energy-dispersive X-ray spectroscopy. EDS utilizes the *characteristic* X-rays to determine which elements are present in the specimen. X-ray emission is the most important and used secondary signal generated in a specimen,³² both in a TEM and an SEM. Emission occurs when an electron with a sufficiently high energy incident on an atom causes an inner-shell electron to escape the attractive field of the nucleus and leave a hole in the shell. The ionized atom can return almost to its lowest energy state by filling in the hole with an electron from an outer shell. This transition is accompanied by the emission of either an X-ray or an Auger electron, both characteristic of the difference in energy between the two electron shells involved. The energy difference is unique to the atom.³²

The simple Bohr theory of atomic structure is conventionally used when describing peaks in the acquired spectrum. The characteristic X-rays are named in terms of the shell being filled and the shell from which the electron comes, that is the K, L, M, etc. terminology. The energy of these X-rays are detected in an energy-dispersive detector positioned above and as close to the specimen as possible. The X-rays with different energies are counted individually, and the

number of counts in each detector energy channel are turned into a spectrum showing counts per energy. A typical detector has 2048 channels with an energy range of 5 eV to 10 eV per channel, although the energy resolution is about 140 eV. Hence it could be that some spectrum peaks overlap.³²

When operating in STEM mode, the electron probe can be scanned over a region or along a line of interest. It is then possible to detect an X-ray spectrum at every pixel in a digital STEM image, thus extracting lines or maps showing the distribution of each element in the specimen and its relationship to the position along the line or the features in the electron image. While this operation mode literally adds another dimension to the power of the TEM, it lacks in statistical sampling due to the small probe size exciting fewer atoms than a larger probe. This can be compensated for by increasing the acquisition time. But, longer acquisition brings with it several disadvantages, like specimen drift with respect to the probe, the beam damaging the specimen and build up of hydrocarbon contamination on the illuminated region. This leads to worsening of both the spatial, energy and chemical resolution. Ideally, X-ray counts from a specimen are only a function of Z , but since a thicker region of a specimen will emit more X-rays than a thinner region, this variation in thickness has to be considered when interpreting spectra. A background radiation arising as beam electrons are slowed down or stopped by electrostatic interactions with nuclei in the specimen is always present in EDS spectra. The intensity of this braking or *bremstrahlung* radiation is zero at the beam energy and rises until it is effectively infinite at zero energy.³²

One way to quantify the relative amounts of each element present in a spectrum is to consider the relative intensities I of two elements A and B in a spectrum. By summing the area under the element peaks above the background, the weight percent ratio of each element is given as

$$\frac{C_A}{C_B} = k_{AB} \frac{I_A}{I_B}, \quad (2.31)$$

where k_{AB} is a sensitivity factor, dependent on the atomic number Z and the TEM-EDS system and the applied acceleration voltage V_{acc} . It is not a constant since V_{acc} determines the size of the X-ray interaction volume. Eq. (2.31), known as the Cliff-Lorimer ratio technique,⁴² is the most common quantitative EDS technique, but is not ideal due to its cancellation of variations in the probe current incident on the analysis area.³² The k factor can be calculated theoretically or determined experimentally, however theoretical values are shown to give an error of 15-20%.³² The ζ -factor method⁴³ is an improved approach which requires *in-situ* measurements of the probe current. By assuming that the characteristic X-ray intensity is proportional to the mass thickness ρt , i.e. that absorption and fluorescence are negligible, the ζ -factor for pure element A is a proportional factor connecting I_A to ρt and C_A .

Electron energy-loss spectroscopy. EELS discriminate the transmitted electrons according to their loss of kinetic energy when interacting with the specimen. The electrons are separated by a magnetic prism situated below the TEM column and projected onto a detector creating a spectrum of energy loss per energy. This enables the study of many different material properties such as band structure, composition, electron density and thickness of the specimen. By constructing an image consisting only of electrons with a desired energy loss, known as energy-filtered TEM (EFTEM), a thickness map can be constructed by subtracting a zero-loss EFTEM image from an unfiltered image. It can be shown that the equation relating the specimen thick-

ness t , the specimen material mean free path λ , the zero-loss intensity I_0 in the EFTEM image and the total intensity I_t of the unfiltered image is given as³²

$$\frac{t}{\lambda} = \ln \frac{I_t}{I_0}. \quad (2.32)$$

Since λ is the average length the electron travels between scattering events, t/λ is the average number of scattering events for a transmitted electron.

2.3 Scanning electron microscopy

In the SEM, the image is produced by scanning the sample surface with a focused beam of electrons. Since the SEs and BSEs are the main signals in an SEM, as discussed in §2.2.1, information on the surface topography of a sample, which is lost in a TEM, can easily be obtained in an SEM. Also, where samples in the TEM have to be thinner than ~ 200 nm, the SEM permits studies of bulk samples.

There are many similarities between a TEM and an SEM electron column, the latter shown in Fig. 2.13 (a). The column consists of a thermionic electron gun or FEG, two or more magnetic lenses, apertures and deflection coils. Vacuum pumps produce a vacuum of about 10^{-4} Pa, poorer than commonly obtained in the TEM. The gun generates electrons and accelerates them to an energy in the range 0.1–30 keV. The lenses demagnify the electrons to produce a beam at the sample with a spot size diameter < 10 nm that contains a sufficient probe current to form an acceptable image. The beam interacts with the sample to a depth of ~ 1 μ m and generates SEs and BSEs to form an image. The scanned image is formed point by point by the deflection system, which moves the beam to create a ‘raster’ on the sample in much the same way as in the STEM operation mode. The system consists of two pairs of deflection coils which sweep the beam across the sample. The raster size on the sample depends on the working distance, i.e. the distance from the bottom of the final lens to the sample. Since electrons are affected within the working distance, it is desirable to minimise this effect to improve the resolution. The common objective lens design are the one depicted in Fig. 2.13 (a) with the sample and detector below the lens, and another in (b) where the sample is situated *in* the lens and the detector above it. The in-lens design provides a zero effective working distance and a superior resolution. But it also limits the sample size, and magnetic samples cannot be studied.⁴⁴

Image contrast arises when the collected signal varies from one location to another. SEs are loose, outer shell electrons that easily gain sufficient kinetic energy from the scattering process to be escape the material. The SE signal mainly gives topographical contrast since only the SEs close to the surface are able to escape. Edge features on the sample will be bright in the image as the electrons here will have a higher chance of escaping. BSEs are electrons scattered elastically by more than 90° relative to the incident electron probe. This high angle elastic scattering is proportional to the atomic number squared Z^2 , thus giving compositional contrast similar to the contrast in the BF and DF TEM operation modes. Images formed from this signal has lower resolution than from the SE signal and little topographical contrast, since fewer BSEs escape from the sample and the electrons escape from a larger area.⁴⁴

The limiting sharpness and feature visibility of SEM images are dependent upon four parameters: the electron probe size d_p , the electron probe current i_p , the electron probe convergence

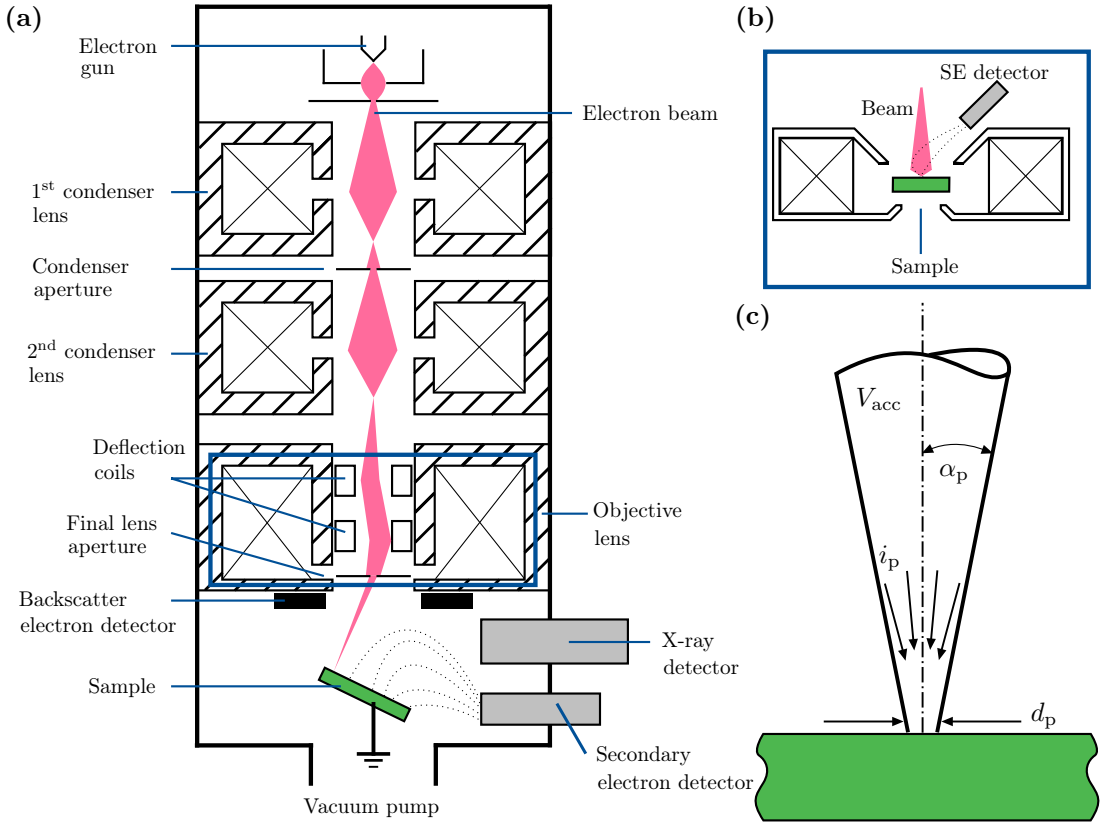


Figure 2.13: Schematic of a typical SEM (a) with a conventional objective lens above the sample. An in-lens objective lens (b) with no working distance, but limited sample size. Four major electron beam parameters (c) where the probe impinges on the sample: the electron probe diameter d_p , the electron probe current i_p , the electron probe convergence α_p and the electron beam acceleration voltage V_{acc} . Adapted from Goldstein et. al.⁴⁴

angle α_p and the electron beam accelerating voltage V_{acc} , as shown in Fig. 2.13 (c). d_p is the diameter of the final beam at the sample surface, i_p is the current that impinges upon the sample and α_p is the half-angle of the cone of electrons converging onto the sample. To study the smallest features of a sample, d_p must be as small as possible while still providing a sufficient i_p . Large i_p is necessary for successful compositional analysis using X-rays, because only a small fraction of beam interactions result in X-ray emission. For the best depth of focus α_p must be as small as possible, since then d_p changes only a little over a long vertical distance and features at different heights will appear to be in focus at the same time. $\alpha_p = 1$ mrad is considered to be small. At $V_{acc} \leq 5$ kV the beam interaction with the sample is confined to the upper few hundred nm of the surface. This enhances the surface detail of an image compared to images obtained at higher V_{acc} where the beam penetrates deeper into the sample and the emerging electrons mostly carry information about the interior of the sample.⁴⁴

2.4 Crystal texture analysis

The *orientation*^{45,46} of crystals or ‘grains’ in polycrystalline materials refers to how the atomic planes in a volume of grain are positioned relative to a fixed reference. Deformation and recrystallisation develop a preferred orientation or *texture* of these grains in most materials, and many macroscopic properties are texture specific. The relationships between grains are specified by the *rotation* or *misorientation* between adjacent grains and their interface boundary.⁴⁵ Such a relationship can thus be defined by three misorientation parameters and two interface parameters (for approximately planar interfaces). Spatially resolved crystal orientation and phase maps can be obtained by a number of X-ray^{47,48} and electron diffraction^{38,40} techniques. An example is *automated crystal orientation mapping* and phase mapping in a TEM (ACOM-TEM) by SPED. While how to assign crystal orientations to each PED pattern is covered in the experimental section §3.4.4, how to represent and interpret the orientation data is discussed here.

2.4.1 Orientations and misorientations

Each position in a crystal orientation map describes the phase and directions of the crystal basis vectors. The directions with respect to the specimen are specified in terms of a *specimen reference frame* r and a *crystal reference frame* h_i . The local orientation can then be described as a transformation between coordinate systems. To simplify the description it is common to use orthonormal, right-handed reference frames that share the same origin. An orientation is then defined as

$$r = gh, \quad (2.33)$$

where the orientation matrix g relates the crystal coordinates $h = (\mathbf{e}_1, \mathbf{e}_2, \mathbf{e}_3)$ to the specimen coordinates $r = (\mathbf{x}, \mathbf{y}, \mathbf{z})$. g is taken to be positive for a rotation that is counterclockwise when viewed along the corresponding rotation axis towards the origin. g is a 3×3 matrix comprised of the angles between every crystal coordinate $(\mathbf{e}_1, \mathbf{e}_2, \mathbf{e}_3)$ with every specimen coordinate $(\mathbf{x}, \mathbf{y}, \mathbf{z})$. Misorientations m are transformations between two crystal reference frames h_1 and h_2 , taken to have orientations g_1 and g_2 . It follows that

$$m = g_2^{-1}g_1, \quad (2.34)$$

$$mh_1 = g_2^{-1}g_1h_1 = g_2^{-1}r = h_2. \quad (2.35)$$

Fig. 2.14 shows a schematic representation of an orientation map.

Orientations and misorientations can be represented in numerous ways, covered in great detail in textbooks on crystallographic texture analysis.^{45,46} It is common to describe the direction of any vector in a crystal as a point on the *unit reference sphere*. The sphere with radius 1 is centred on the crystal, and the intersection of the sphere with the crystallographic plane normals are known as *poles*. A crystal orientation can be described in a *pole figure* by projecting its poles onto the sphere with angles (α, β) between one pole and two of the three axes in r , respectively. Vice versa can the orientation of r be projected into h in the *inverse pole figure* (IPF). The poles on the 3D unit sphere is projected onto the 2D equatorial plane in the *stereographic projection*. A 2D projection along with intersections of the unit sphere with the major crystallographic axes in a cubic system is shown in Fig. 2.15. The symmetry of the crystal itself is carried

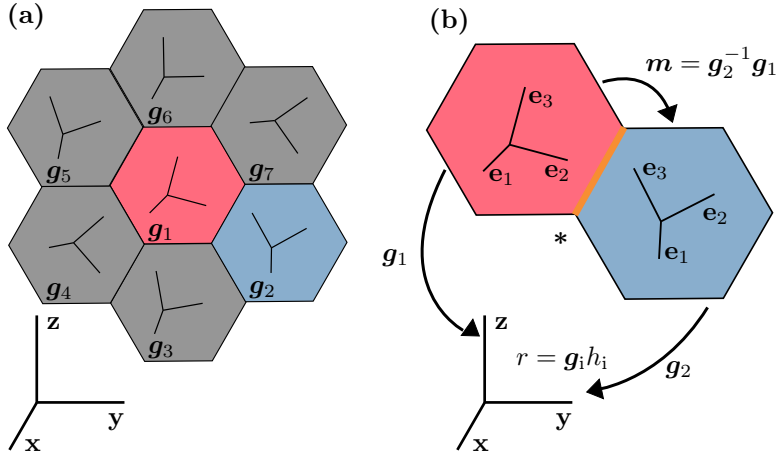


Figure 2.14: Schematic of (a) orientations g_i of crystallographic axes in e.g. a pixel or a grain with respect to an external reference frame. (b) Transformations of orientations g_i from the crystal reference frame h_i into the specimen reference frame r . A misorientation m describes a transformation between crystal reference frames across a boundary element (*).

through to the representation of the unit sphere, meaning that the sphere is divided by the symmetry planes into spherical triangles. The triangle corners are marked by that specific planes' symmetry elements. The projection of these triangles in 2D together for the cubic system is shown in Fig. 2.2. A single triangle spanned by the major crystal planes $[001]$, $[011]$ and $[\bar{1}11]$ is commonly used for an IPF representing orientations of a cubic system.

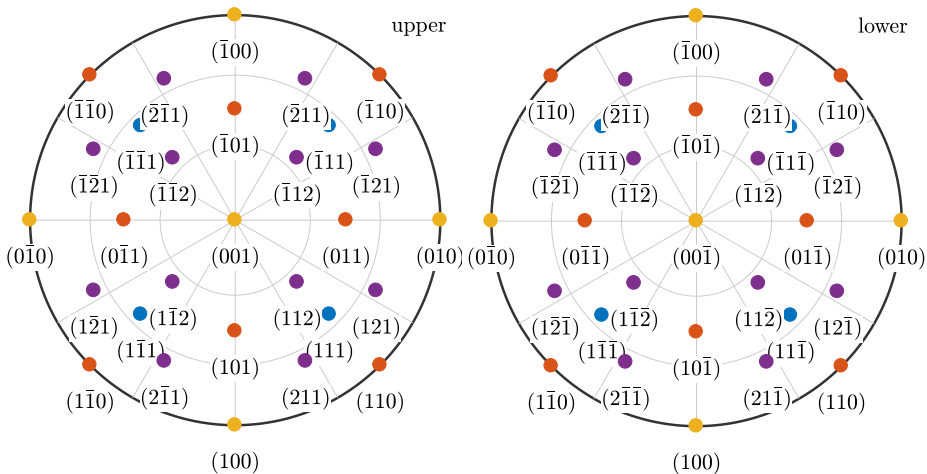


Figure 2.15: 2D projection showing upper and lower hemispheres of intersections between major crystallographic axes in a cubic system and the unit sphere.

2.4.2 Orientation mapping

To illustrate the resulting texture and grain size information obtainable from PED patterns and ACOM-TEM, a data set of gold (Au) nanoparticles³⁹ was acquired. Their crystal structure, belonging to space group $225 \text{ Fm}\bar{3}\text{m}$ with a lattice parameter of approximately 4.08 \AA , was used to simulate diffraction patterns to create a so-called *template bank* to compare to the experimental PED patterns. This procedure is known as template matching. Template banks from multiple phases can be compared to the experimental patterns in the sample template matching process. Fig. 2.16 shows a BF TEM image of the specimen, along with maps of the correlation index Q and reliability R . Every comparison of simulated and experimental patterns gets a score Q , and the simulated pattern with the highest score, i.e. the best match, is selected as that experimental pattern's or pixel's crystal orientation. R denotes the reliability of this orientation. The ACOM-TEM approach thus gives every probe position a phase, orientation, index Q and reliability R . The orientation is given in the common representation of Euler angles, which are three successive rotations about independent specimen coordinate axes through angles (ϕ_1, Φ, ϕ_2) , according to the Bunge definition.⁴⁶ A detailed explanation of the template matching is covered in §3.4.4. Low Q -scores (blue) are seen in the vacuum and between the particles. It is common to filter orientation maps based on Q and R to enhance the visibility of the structural features.

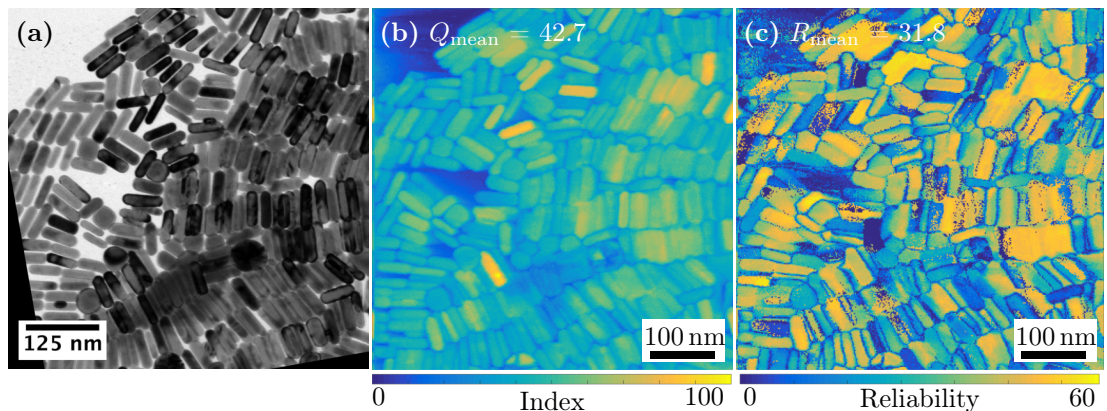


Figure 2.16: TEM BF image (a) of Au nanoparticle seeds dispersed on a carbon film.³⁹ Orientation data was acquired from the same area showing maps (0-100, blue-yellow) of the correlation index Q (b) and the reliability R (c) in each pixel.

Filtered orientation maps along the indicated specimen coordinates \mathbf{z} , \mathbf{x} and \mathbf{y} are shown in Fig. 2.17, coloured according the IPFs. Since one IPF only represents one direction of the 3D orientation information, rotations about this axis are not seen. All three maps are therefore needed for a complete interpretation. A subset of all crystal coordinates viewed along each specimen coordinate is also plotted into the IPFs, indicating texture. E.g., almost all particles has some crystal plane between (001) and (011), like (013) and (012), parallel to the \mathbf{z} coordinate. The fast growth direction of the particles have been reported to be along the [111] direction,³⁹ seen here by the lack of particles with their (111) planes parallel to \mathbf{z} . No notable difference in the \mathbf{x} and \mathbf{y} IPFs indicate no clear texture in-plane, although some clusters are seen due to the particles aligning with their short axes parallel to the alignment direction.

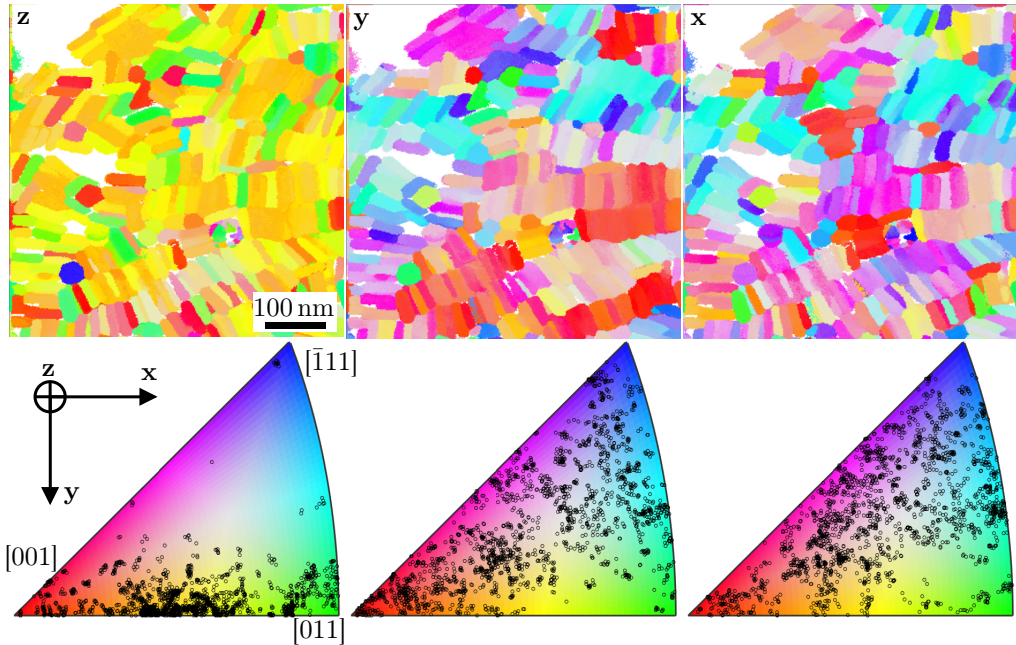


Figure 2.17: Orientation maps and corresponding IPFs (below map) of the Au specimen in the indicated specimen coordinates z , y and x . A subset of all crystal coordinates viewed along each specimen coordinate is also plotted into the IPFs.

Orientation distribution functions (ODFs) describe the probability of finding orientations within a given angular distance to a given axis. Fig. 2.18 shows the orientation of crystal planes normals $[001]$, $[011]$ and $[\bar{1}11]$ with respect to the specimen coordinates in pole figures and calculated ODFs based on these figures. The same texture information as in the IPFs can be discerned from these representations, e.g. by considering the low probability of $[111] \parallel z$ shown in the $[\bar{1}11]$ ODF. Also, no clear texture in-plane is seen as near continuous angular distributions around z , apart from some higher probabilities of planes oriented almost parallel to y .

2.4.3 Grain size analysis and misorientations

Grain boundaries are commonly found by thresholding the misorientations between adjacent data points,⁴⁹ typical thresholds in the range of 1° to 10° . When boundaries consist of gradual changes in orientation of $< 1^\circ$, there is no thresholding value or range that captures important boundaries between regions without including many irrelevant boundary segments. A fast multiscale clustering (FMC) algorithm⁵⁰ can be used to create boundaries in these structures. The algorithm is explained in detail in §3.4.5. Segmenting the Au specimen data set using the FMC algorithm produces the grain boundaries of 251 reliably reconstructed grains in Fig. 2.19 (a). Coloured grain boundary misorientations between particles are shown in (b), the maximum possible misorientation angle allowed by symmetry being 62.8° . Note the wrongly reconstructed grain in the upper left corner due to the inherent problem of afterglow of the recording system, as was discussed in §2.2.3. The equivalent diameter of the projected area of each grain can be

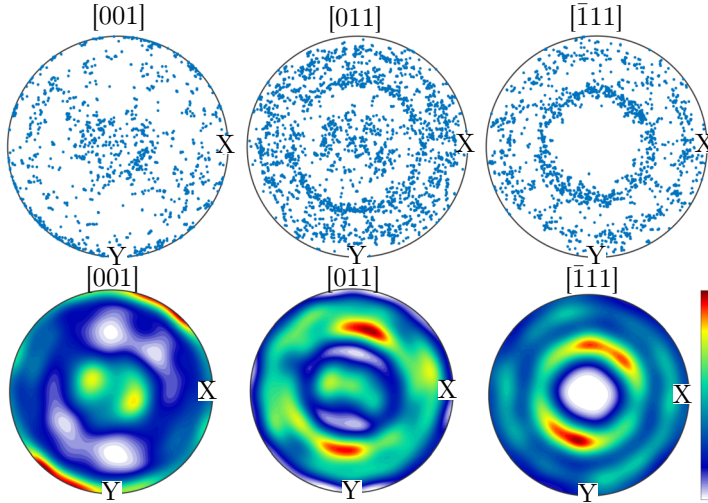


Figure 2.18: $[001]$, $[011]$ and $[\bar{1}11]$ pole figures of a subset of all crystal coordinates and calculated ODFs of the Au specimen relative to the specimen coordinates. The colour bar indicates probability density from low (blue) to high (red).

calculated from a circle with the same area as the grain, as shown in (d). A grain diameter distribution is shown in (c) with a commonly used lognormal distribution fit to the data. The average equivalent diameter of the grain projections is found to be (31.3 ± 0.6) nm using two standard deviations, equivalent of a projected area of 769 nm^2 . A manual calculation of 30 particles in the BF image estimates the projected area to 991 nm^2 , indicating either that the FMC algorithm underestimates the area by 22% or that the scalebar in the data set or the BF image is wrong.

While a crystal in 3D space is mostly represented in the Euler angles, other neo-Eulerian mappings have been suggested,⁵¹ among them the *Axis-Angle* of rotation. A (mis)orientation is in this mapping described by the smallest of rotation angles ω among equivalent rotations ξ relating two given orientations h_1 and h_2 .⁵² The misorientation angle distribution of the Au grain boundaries is shown in Fig. 2.20 (a), indicating high densities at low angles $< 10^\circ$ and from 30° to 45° . A random distribution is included for comparison, and the correlated distribution follows this random one nicely. Since the particles are discrete and not connected in any other way than aligning on the carbon film, the higher density of low angle misorientations is expected. The misorientation axis distribution is shown in Fig. 2.20 (c) plotted into the IPF, with a random distribution in (b) included for comparison. A strong preference of orientations connected by rotations about the $[001]$ crystal axis is found.

Although this SPED data set of Au particles illustrate nicely the concepts of texture and grain size analysis, grains in a polycrystalline material have no space between them and the grain boundaries might not be perpendicular to the incoming electron beam. This results in poor template fitting due to overlapping grains. However, the general principle of template fitting, representation of orientation and possible texture and quantification of misorientation and grain size for materials with overlapping grains is similar. A wealth of information on crystallographic

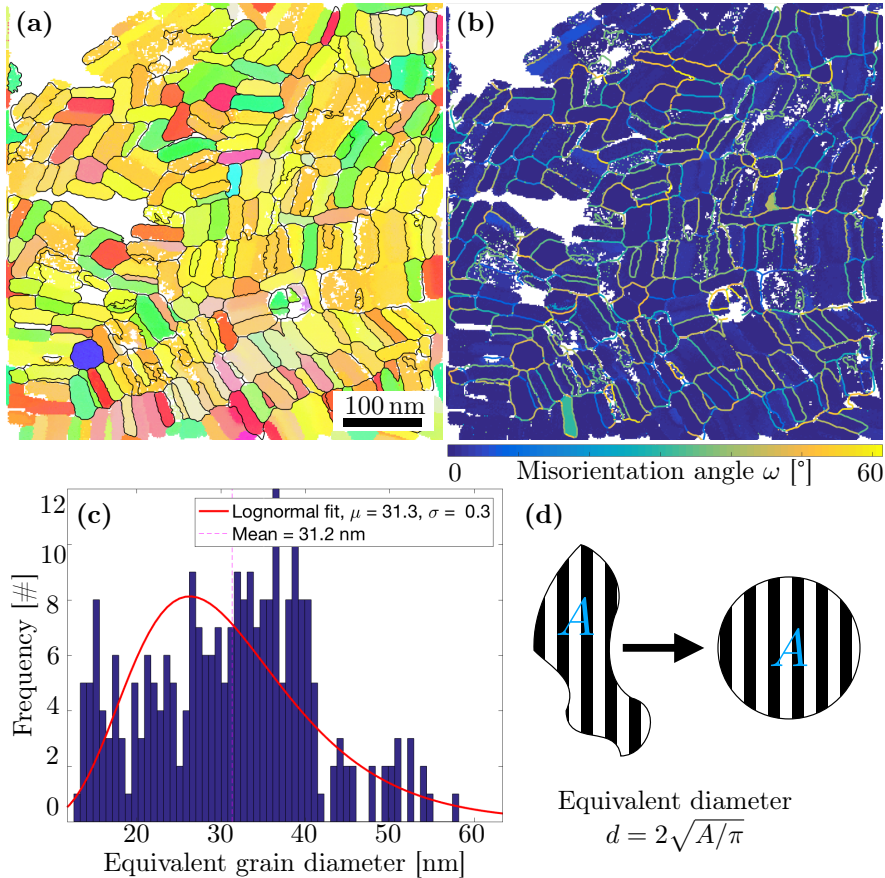


Figure 2.19: Boundaries of filtered grains on top of the orientation map of the Au specimen (a), colour coded by the z IPF. The grain boundaries colour coded according to the misorientation angle (b), on top of an orientation map showing the grains coloured according to the misorientation of each pixel to the mean orientation within each grain.

orientations and phases within a material is extractable from these large data sets of tens of thousands of DPs. Although the SPED technique is powerful, it is important to keep in mind the inherent limitations imposed by the recording method and the subsequent data analysis.

2.5 Multivariate statistical analysis

An unbiased, robust method to separate the diffracted intensities for each orientation or phase in a 4D data set comprised of ‘mixed’ PED patterns is necessary. The goal is to learn the underlying eigenvectors or *component patterns* that make up the data, together with their associated score or *loading* at each real space pixel. Perhaps the simplest way to visualise a multi-dimensional data set is through the *principal component analysis*⁵³ (PCA) algorithm. It does not take any parameters besides the data itself as input and outputs component patterns arranged from most to least information dense, the respective loading maps associated with each

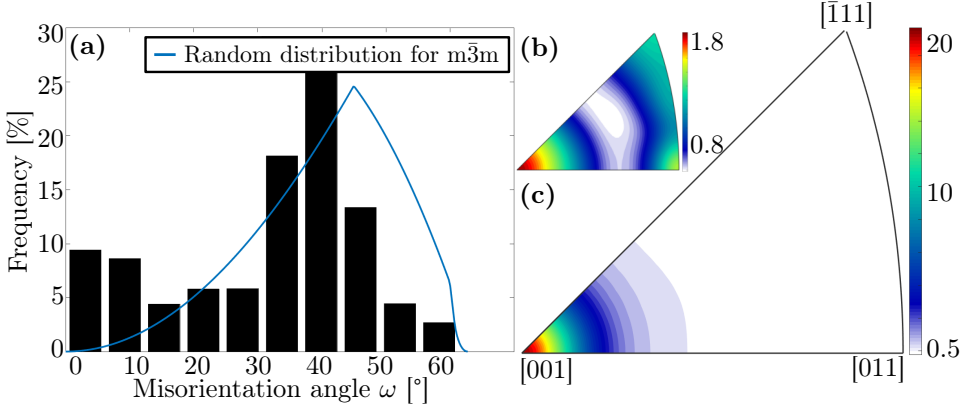


Figure 2.20: The misorientation angle distribution (a) and misorientation axis distribution (c) for the Au specimen. A random distribution (b), assuming no orientation relationships between grains, is included for comparison.

pattern and a Scree plot that represents the information content as a function of component pattern number. However, PCA suffers from difficulty of interpretation of patterns and loadings since they allow for subtractive combinations.

Non-negative matrix factorisation (NMF)⁵⁴ is another algorithm in multivariate statistical analysis which only allows additive combinations. It has previously proved valuable for a variety of image and spectral processing. For example, it enabled the successful reconstruction and ‘segmentation’ of the reciprocal lattice geometry of three phases inherent in a nanoscale Ni-based superalloy volume.⁵⁵ The use of NMF in SPED data analysis is motivated by comparing the as obtained data to the general problem the method tries to solve: Given a non-negative matrix V , find non-negative matrix factors W and H such that

$$V_{ij} \approx (WH)_{ij} = \sum_{a=1}^r W_{ia}H_{aj}. \quad (2.36)$$

V is a $n \times m$ matrix, where each column contains n non-negative pixel values of one of the m acquired DPs. V can e.g. consist of $m = 300^2$ DPs or real space pixels, each consisting of $n = 144^2$ reciprocal space pixels. NMF then approximates V by a linear combination of r component patterns in W that make up the data. Each pattern is weighted by a loading in H . The dimensions of the matrix factors W and H are $n \times r$ and $r \times m$, respectively. The number of component patterns r of the factorisation is ideally limited to the number of orientations and phases in the volume studied, and the product WH can be regarded as a compressed form of the data in V . When the appropriate number of component patterns to represent the data is not easily found, performing PCA to study the Scree plot can aide in deciding this number before performing NMF. The non-negativity constraint enables easier physical interpretation of the decomposition results and their use directly in understanding the crystallography of the studied volume. However, acquired DPs comprising signals from overlapping crystals lead to the question of whether the factorisation returns unique component patterns or a combination of multiple orientations and phases.

To illustrate the overlap problem, results from a NMF decomposition of a subset of the SPED data set of the Au specimen is shown in Fig. 2.21. These results can be directly compared to the DP and VDF images shown in Fig. 2.12 (b,e). The same DP, here shown in Fig. 2.21 (a) acquired from the area indicated in the squares in (f,g), shows reflections from two particles overlapping in a small area of approximately 50 nm^2 . The overlap is clearly visible as rotational moiré fringes in the HRTEM image in (e), indicating a 10° misorientation, close to the 8° misorientation calculated directly from the moiré fringes in §2.2.3. The decomposition results include the two component patterns in (b,c) and corresponding loading maps in (f,g), showing two groups of particles with comparable in-plane orientation. Where the loadings are brightest indicates where the components are most dominant. The patterns lack intensity in the direct spot because this is separated by the decomposition as another component. The decomposition has also isolated the noise not inherent to any particular DP to another component, which can be understood by considering the reduced noise in the component patterns compared to the acquired DP in (a). A sum of the two patterns is shown in (d). A sum of the two loadings is shown in (h) with the overlap region indicated. Although the two particles overlap, the NMF decomposition manage to reconstruct the shapes of the particles.

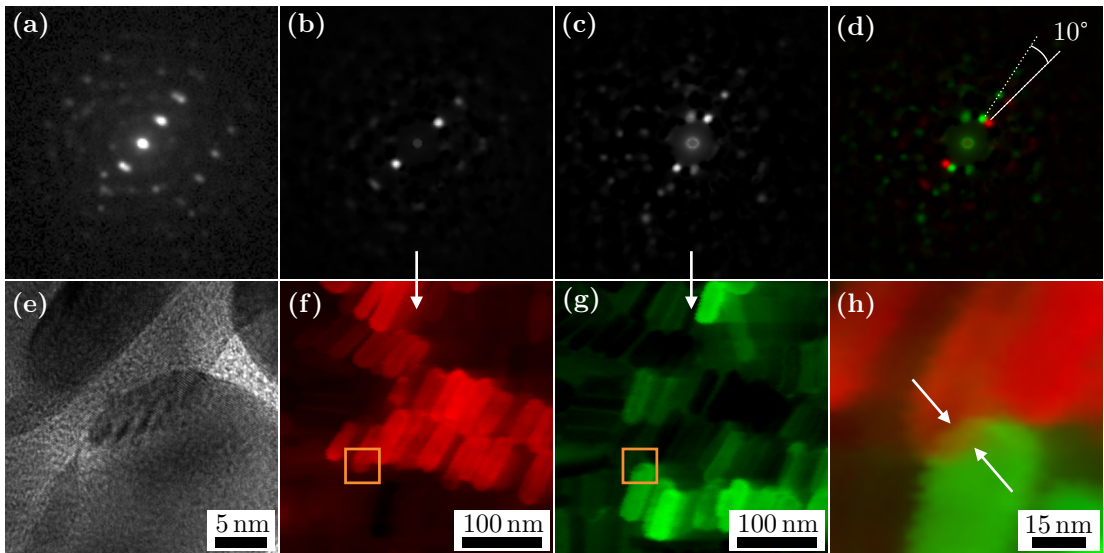


Figure 2.21: PED pattern (a) from two overlapping Au particles, comprised of at least two component patterns (b,c) resultant from a NMF decomposition. The patterns' corresponding loading maps (f,g) show two groups of particles with a 10° misorientation, indicated in the sum of the two patterns (d). The overlap is easily seen in the HRTEM (e) and VDF (h) images. The VDF image is reconstructed from the two loadings.

2.6 Photochromism

When electromagnetic radiation impinges on a material, fractions can either be transmitted, reflected or absorbed. Energy conservation yields, at each wavelength, that

$$T(\lambda) + R(\lambda) + A(\lambda) = 1, \quad (2.37)$$

where T , R and A denote transmittance, reflectance and absorptance, respectively.¹² *Photochromism* is defined as a reversible change of a single chemical phase between two states having distinguishably different absorption spectra, the change being induced in at least one direction by electromagnetic radiation.⁸ Thus, a photochromic material is one which undergoes a reversible colour change in response to light. The definition can be represented as



where h is the Planck constant, ν is the frequency of the absorbed photon and A is a single chemical phase. The photoproduct B may also be a single chemical phase, or it may represent more than one phase, provided that they recombine to give A . Fig. 2.22 (a) shows a typical reversible photocoloration where a phase A , which absorbs light at a certain wavelength range centred on λ_1 , changes into a phase B , which absorbs light at another range centred on λ_2 , when absorbing photons of energy $h\nu$. When the source of photons is stopped, the photoproduct B returns to its initial phase A .⁸

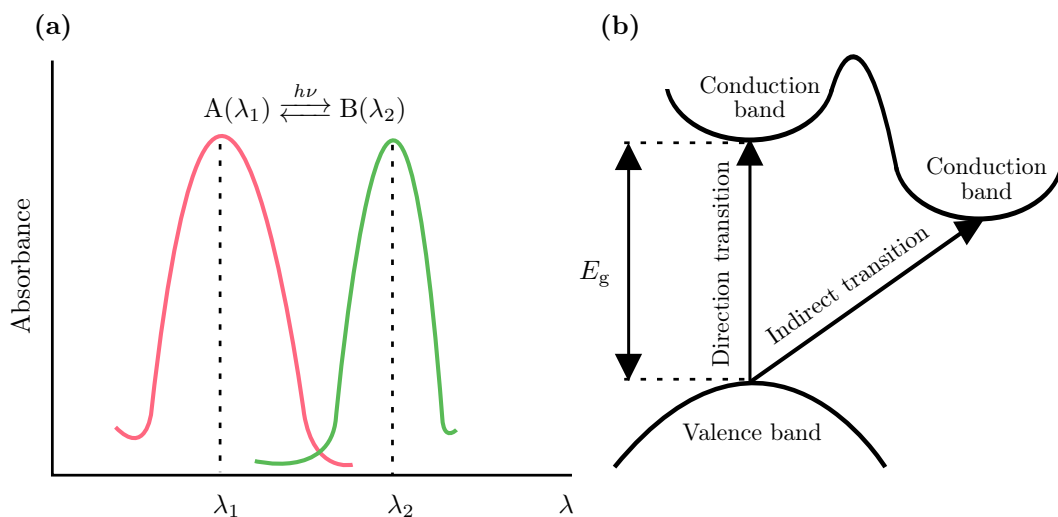


Figure 2.22: A typical reversible photocoloration (a) of phase A when absorbing photons of energy $h\nu_1$. In materials this absorption is a result of direct or indirect electron transitions (b) across a band gap E_g if the photon has sufficient energy.

Both organic and inorganic substances in the solid state or in solution may exhibit photochromic behaviour. The types of inorganic solids that exhibit photochromic phenomena are for the most part insulators or semiconductors and have a large band gap E_g between 3 eV to 12 eV. This corresponds to wavelengths λ between 100 nm to 400 nm. Since the visible light region $\Delta\lambda_{\text{vis}}$ of the electromagnetic spectrum is between 400 nm to 700 nm, a material's ground state has negligible optical absorption in this region. When photons of energies corresponding to E_g optically excite these materials, metastable bands that can absorb light in the visible region of the spectrum form. This results in a characteristic colour change. Direct and indirect band transitions are illustrated in Fig. 2.22 (b).⁸

2.6.1 Photochromism in oxygen-containing yttrium hydride

In semiconducting transparent YHO thin films, up to 50% of the optical transmittance is reduced over the wavelength range between 500 nm to 900 nm, after one hour of illumination.¹⁸ This range encompasses most of the visible light range $\Delta\lambda_{\text{vis}}$. This particular observation was made in a 520 nm thick film deposited on a soda lime glass substrate. The variation in the optical transmittance is shown in Fig. 2.23 (c). Before illumination the YHO thin film has a yellowish transparent appearance because of absorption of blue ($\lambda_{\text{blue}} \approx 450$ nm) and violet ($\lambda \approx 400$ nm) light, shown in Fig. 2.23 (a). The photodarkening, i.e. the reduced transmittance, is observed after illumination with a solar simulator, shown in Fig. 2.23 (b). When the illumination is turned off, the film bleaches back to the initial transparent state in (a). The band gap of the depicted thin film was $E_g = 2.6$ eV $\propto \lambda_{\text{blue}}$. Accompanying the variation in the optical transmittance is an almost identical variation in the electrical resistivity. When subjected to radiation of similar intensity with either a blue wavelength λ_{blue} , green wavelength $\lambda_{\text{green}} \approx 530$ nm or a red wavelength $\lambda_{\text{red}} \approx 620$ nm, the change in resistivity is strongest for the blue, lower for the green and substantially lower for the red. This observation that illumination with wavelengths above E_g gives a stronger variation in the resistivity suggests that excitation of charge carriers from the valence band is essential to obtain a photochromic response in YHO.¹⁸

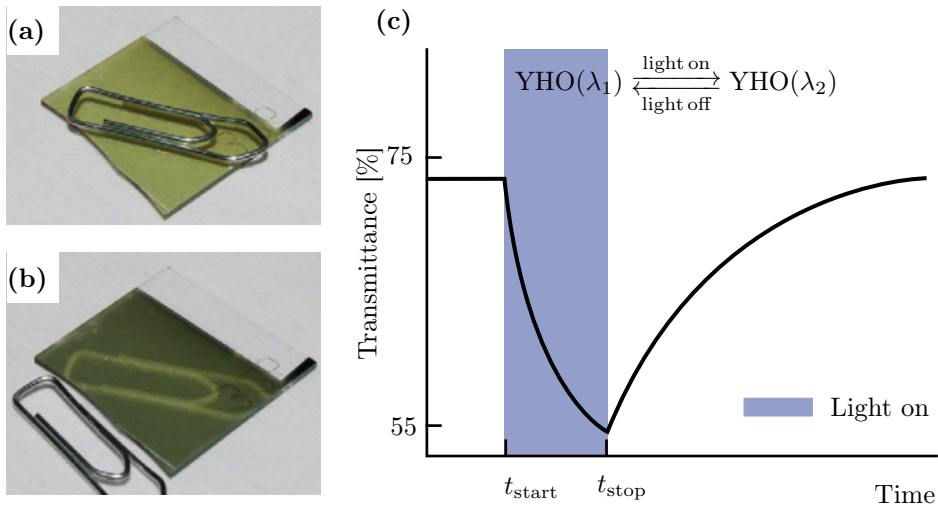


Figure 2.23: The YHO thin film before illumination (a) and after illumination (b), taken from Mongstad *et. al.*¹⁸ Optical transmittance of a YHO sample (c) as a response to a solar simulator for a certain time.¹⁸

Changes in the band gap E_g in YHO thin films are linked to the oxygen content of the films. As-deposited oxygen-free yttrium hydride films capped with an aluminium layer to prevent the film from absorbing oxygen are shown to have a dark and opaque appearance with metallic properties, while oxygenated films are transparent and photochromic²⁰ (sputtering deposition is covered in §2.7). The band gap has been found to increase from 2.8 eV to 3.7 eV for films grown at deposition pressures of 1.2 Pa and 6 Pa, respectively,²³ and the oxygen to yttrium ratio was recently found to increase from 1 to 1.7 when the going from 1 Pa to 6 Pa.²² Simultaneously, the hydrogen to yttrium ratio was found to decrease from 2.2 to 0.6, i.e. concentrations of oxygen and hydrogen are anti-correlated. Moreover, the higher deposition pressures led to the formation

of high porosity of the film at the surface, which might result in faster oxidation. These findings have been supported by density functional theory calculations, where it was found that the band gap value is straightforwardly dependent on an incorporated oxygen amount that is irreversibly trapped by yttrium atoms.⁵⁶ The calculations also suggested that the YHO structure is a direct band gap semiconductor. The preferred oxygen position in the expanded fcc $\text{YH}_{2.5}\text{O}_{0.25}$ cell were found to be a slightly distorted tetrahedral site (0.747, 0.747, 0.747) that is very close to the nominal site $(\frac{3}{4}, \frac{3}{4}, \frac{3}{4})$. To make room for the oxygen atom, the structure had one less hydrogen atom in another tetrahedral site $(\frac{1}{4}, \frac{1}{4}, \frac{1}{4})$. However, no experimental results so far have come close to explain the exact role and location of the oxygen atoms in the structure.

Recently, two films deposited at different partial hydrogen/argon pressures of 0.18 and 0.13 were found to be respectively of a oxygen-rich, transparent, semiconducting character and opaque, metallic yttrium hydride phase.²⁴ The latter had a lattice parameter of 5.4 Å, while the former had one of 5.2 Å, matching very well stoichiometric YH_2 . The crystal cell of YH_2 is shown in Fig. 2.24. The same explanation of an increased oxygen content was given for the high transparency. However, the optical properties of the photodarkened films is explained by a gradual formation of small domains metallic domains in the semiconducting lattice upon illumination.

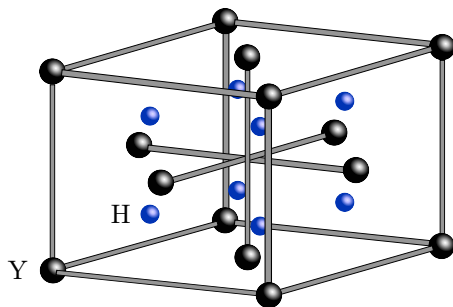


Figure 2.24: The fcc structure of yttrium hydride YH_2 with one Y atom (0, 0, 0) and two H atoms $(\frac{1}{4}, \frac{1}{4}, \frac{1}{4})$ and $(\frac{1}{4}, \frac{1}{4}, \frac{3}{4})$ as the basis.

2.7 Thin film synthesis

Thin film materials exhibit unique material properties resulting from the atomic growth process.⁵⁷ A group of thin film processes termed *physical vapour deposition* (PVD) processes involve three main steps: (1) production of the appropriate atomic, molecular or ionic species, (2) transport of these species to the substrate through a medium, and (3) condensation on the substrate, either directly or via a chemical reaction, to form a solid deposit. The properties of thin films are often affected by the properties of the substrate and can vary through the thickness of the film.⁵⁸ PVD processes can take place in a vacuum, plasma or gaseous environment. They are typically used to deposit films with thickness in the range of a few nm to thousands of nm. Substrates can range in size from very small to very large, for example (25 × 30) cm glass panels used in buildings.

2.7.1 Reactive sputtering deposition

Sputtering deposition is a type of PVD process involving non-thermal vaporisation of surface atoms from a solid. This is achieved by momentum transfer from an atomic-sized, energetic, bombarding particle. The particle is usually a gaseous ion, typically argon (Ar), accelerated from a plasma. The most common form of sputtering is plasma-based sputtering. One way to create a plasma is with a direct current, diode discharge. A material, known as the target, is placed at the cathode and the substrate to be deposited on is placed at the anode. The goal is to deposit the target material, for example Y, on the substrate. The positive ions created are accelerated toward the target, which is at a negative potential with respect to the plasma. To enhance the sputter yield, a magnetron sputtering configuration is often used. By applying a magnetic field at the target, the electrons ejected from it are deflected to stay near its surface. The resultant high flux of electrons creates a high density plasma from which ions can be extracted to sputter the target material. The most common magnetron source is the planar magnetron, where the sputter erosion path is a closed circle on a flat surface. It is common to introduce a reactive gas like hydrogen (H_2) into the sputter chamber to create multicomponent and/or multiphase films. The target atoms can then react with the gas in travel, and on the substrate, creating a compound material. In combination, the total process is termed *reactive magnetron sputtering deposition*. An example of a sputtering chamber can be seen in Fig. 2.25. Among the parameters to control to achieve a reproducible process and product are substrate surface cleaning, sputtering rate, pressure of mixture of sputtering and reactive gas, sputtering target voltage and substrate temperature.⁵⁸

Formation of a thin film takes place via nucleation and growth processes. The general picture can be presented in six steps:⁵⁷ (1) incident species, on impacting the substrate, lose their velocity component normal to it and are physically adsorbed on the substrate surface. (2) The species are initially not in thermal equilibrium with the substrate and move over the surface, interacting amongst themselves, forming bigger so-called nuclei. (3) The nuclei are thermodynamically unstable and may collide with other adsorbed species before desorbing and hence grow in size. When a critical size is reached, the nuclei becomes thermodynamically stable. (4) The critical nuclei grow in number as well as in size until a saturation nucleation density is reached. They can grow both parallel to the substrate by surface diffusion of the adsorbed species, as well as perpendicular to it by direct impingement of the incident species. However, the rate of lateral growth is at this stage much higher than the perpendicular growth. The grown nuclei are called islands. (5) The small islands start to coalesce in an attempt to reduce the surface area, the tendency termed agglomeration. (6) Larger islands grow together, leaving channels and holes of uncovered substrate. The structure of a film at this stage changes from discontinuous island type to porous network type.

2.7.2 Column growth morphology

Atomically deposited films generally exhibit a unique *column growth morphology* that resembles logs aligned and piled together.⁵⁸ The morphology of a deposited film is determined by the substrate surface roughness, the surface mobility and surface diffusion of the depositing atoms, or *adatoms*, and geometrical shadowing. The latter effect is stronger if the incident flux of adatoms is off-normal so that valleys between the columns are in 'deeper shadows' than when the flux is normal to the surface. The substrate influence in general the film growth near the

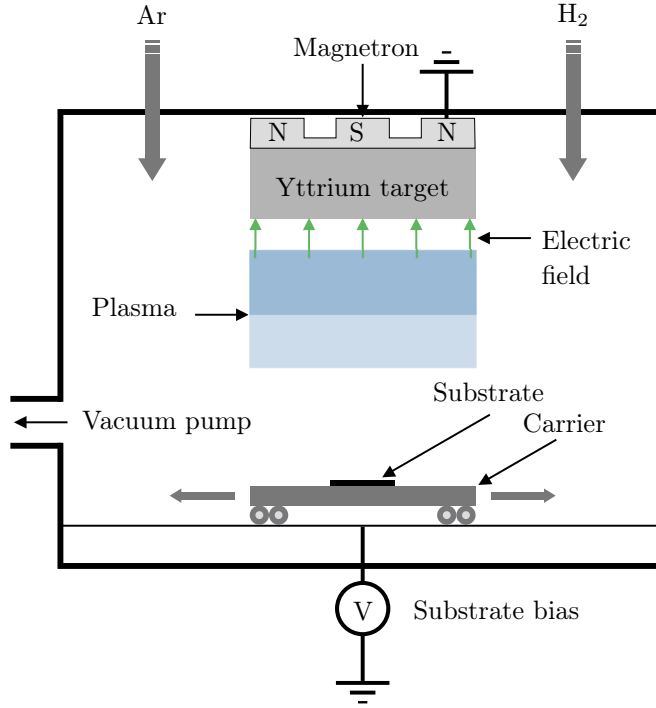


Figure 2.25: Schematic of a reactive magnetron sputtering deposition chamber. Ar ions created in a plasma sputter Y atoms off a Y target on top of a magnetron. An electric potential accelerates the Y atoms towards a substrate placed on a moving carrier while reacting with hydrogen atoms both in travel and on the substrate. To achieve a homogeneous film, a carrier oscillates the substrate back and forth in front of the target. The result is deposition of a YH_x thin film on the substrate.

interface. The film morphology can be described by a *structure zone model*⁵⁹ (SZM) when it is of a certain thickness and has established a particular growth mode. The structure of sputtering deposited films can in this model be divided roughly into four zones, termed *I*, *T*, *II* and *III*. An illustration adapted from Ref. 59 is shown in Fig. 2.26. In *zone I* the adatom surface diffusion is insufficient to overcome the geometrical shadowing by the surface features, meaning that open boundaries between the columns are formed. This morphology produces a film with a high surface area. In *zone T*, the film has a fibrous morphology. Here, high energy neutral atoms from the sputtering target erode the column peaks and fill in the valleys to some extent. The growth process in *zone II* is dominated by adatom surface diffusion, allowing densification of the intercolumnar boundaries while the basic column morphology remains. The grain size increases and the surface features tend to be faceted. Bulk diffusion in *zone III* allows recrystallization, grain growth and densification. The highly modified column morphology is often detectable, with the columns being single crystals of the material. Preferential crystallographic orientation, i.e. texture, is often observed in sputtering deposited films.

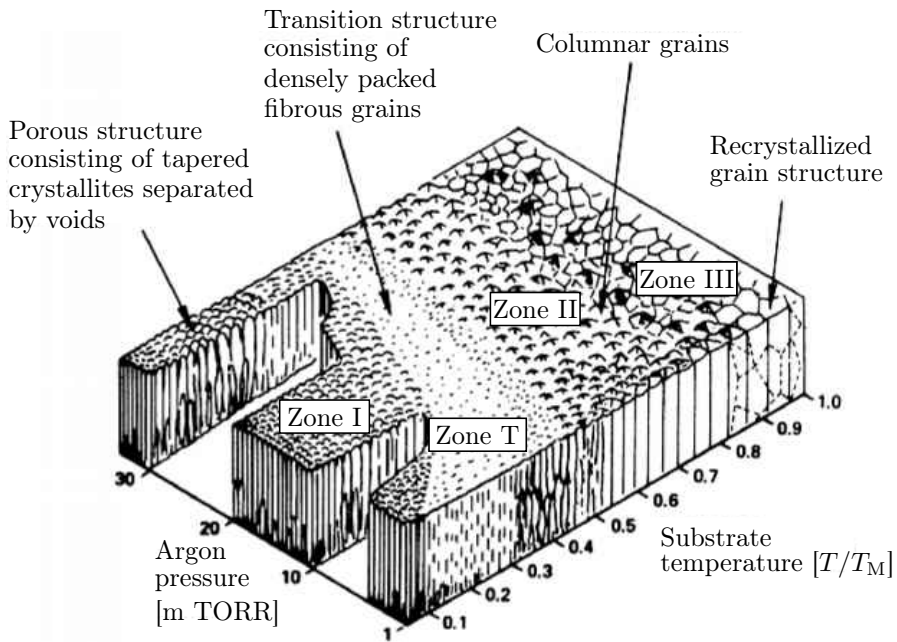


Figure 2.26: Illustration of the SZM with four structural zones as a function of the Ar pressure in the deposition chamber and of T/T_M , where T is the substrate temperature and T_M is the melting point of the sputtering target. Adapted from Thornton.⁵⁹

3 | Experimental methods and data processing

3.1 Thin film synthesis

The YHO thin films studied in this work were synthesised at the solar cell laboratory at IFE, Kjeller by researcher Fredrik Martinsen. The steps discussed here are also presented in an article by Montero *et al.*²⁰ in the IFE group. A reactive magnetron sputtering deposition process, discussed in §2.7, was used. The author did not participate in synthesising the particular films studied in this work, but worked as a research assistant on thin film synthesis within the smart window project in the laboratory at IFE during the summer months of 2016.

Oxygen-free, metallic YH₂ films of thickness 100 nm and 650 nm were deposited using a *Leybold Optics A550V7* in-line sputtering machine operated with a power density of 1.33 W cm⁻². A schematic of a sputtering chamber is shown in Fig. 2.25. A commercially available Y target of dimensions (125 × 600 × 6) mm with a purity of 99.99% was used. The base pressure in the sputtering chamber prior to film deposition was $\sim 10^{-4}$ Pa. Deposition was performed at a pressure of 1 Pa. No O was intentionally introduced into the sputtering chamber. The 650 nm films were deposited on (001) gallium arsenide (GaAs) and (001) silicon (Si) substrates, while the 100 nm film was directly deposited on a holey carbon (C) and copper (Cu) TEM grid. The substrates were cleaned prior to film deposition using ethanol, isopropanol and de-ionised water. The substrate and grid were placed on a carrier that oscillated in front of the target so thin films of even thickness were deposited. After deposition the films were exposed to air where they oxidised. The 100 nm film was deposited in one sputtering process, while the 650 nm films were deposited in another.

3.2 Sample preparation

All sample preparation for the TEM and SEM was conducted by the author at the TEM Gemini Centre sample preparation lab at NTNU, except for the 100 nm film deposited directly on a TEM grid. The samples studied are presented in Tab. 3.1 showing the sample name, film thickness and preparation technique used. Following conventions, all samples for the TEM are termed ‘specimens’.

Table 3.1: Parameters of the samples studied in this work. The sample names are chosen only for convenience, so that they are easy to spot in the text. CS – cross-section, PV – plan-view.

Sample name	Substrate	Thickness [nm]	Preparation	Form	Support grid
AA	Si	650	Ultramicrotomy	CS	Holey-C Cu
BB	-	100	Direct deposition	PV	Holey-C Cu
CC	GaAs	650	Scratching	CS/PV	Holey-C Cu
DD	GaAs	650	Tripod polishing	CS	Omniprobe Cu

3.2.1 Transmission electron microscopy specimen preparation

The goal of the TEM specimen preparation is to obtain an electron transparent side view of the thin film attached to the substrate. The 100 nm film deposited on a TEM grid can directly be inserted into the TEM specimen holder for a top view. When preparing a TEM specimen it is important to consider that the preparation technique must not affect what is to be measured, unless the effect is known. Also, in addition to being electron transparent, it should be representative of the material, uniformly thin, stable under the electron beam and in the laboratory environment and non-magnetic. A study of variations in microstructure and elemental composition along the thickness of a material involves cross-sectioning the sample. One way to prepare a cross-section specimen is by using accelerated ions in an ion milling technique, but bombardment of high energy ions can degrade the crystal structure or even amorphise the specimen.⁶⁰ To avoid this problem mechanical thinning can exclusively be used, e.g. by ultramicrotomy or tripod polishing. Both techniques were used to prepare the TEM specimens in this work, however the former was by far the most successful for preparing sputtering deposited YHO thin films for TEM studies.

Ultramicrotomy. The 650 nm thick specimen AA deposited on an Si substrate was prepared using ultramicrotomy. A brief description of the preparation procedure follows, while a detailed scheme is included in §A. Ultramicrotomy uses a knife to cut sections of the specimen embedded and oriented in epoxy, while controlling the thickness of the sections.⁶¹ It is the main technique for biological materials and polymers. One benefit of the technique is that consecutive sections of a structure can be imaged to recreate it in 3D, however this was not done here.

The thin films were found to delaminate from the Si and GaAs substrates. Although it is preferable to keep a crystalline substrate on the specimen as a reference to calibrate the camera length in diffraction experiments, the 0.5 mm thick Si or GaAs substrate would have damaged the diamond knife under ultramicrotomy sectioning. It was thus the delamination that enabled ultramicrotomy sectioning of large areas of thin film. *Epofix* resin and hardener, from now on termed epoxy, was applied on top of the film and substrate with a paper clip placed inside the epoxy. A summary of the preparation procedure is shown in Fig. 3.1. After being cured, the epoxy was removed by a scalpel. The faint, yellow hue of the film was transferred from the substrate to the epoxy, leading to the conclusion that the film was attached to the epoxy. The epoxy/film was oriented inside a plastic, embedding capsule, and the capsule was filled with more epoxy to create a manageable epoxy/film stub. After being cured, the capsule was removed from the stub. The stub was subsequently placed in the moving arm of a *RMC Boeckeler PowerTome XL*.⁶² The stub face was cut flat and smooth into a (100 × 200) μm rectangle with the film cross-section in the middle along the 200 μm by a razor blade and then

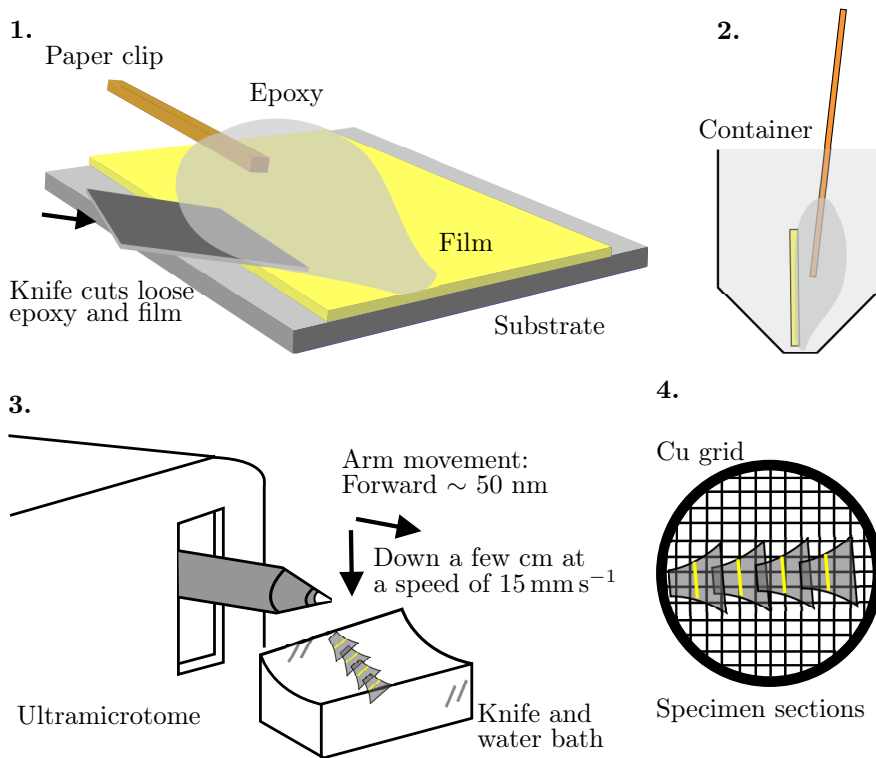


Figure 3.1: TEM specimen preparation by ultramicrotomy. The delamination of the thin film from the substrate (1) was exploited to orient the thin film within the embedding epoxy (2). The epoxy/film was then placed in the tip of the arm on the ultramicrotome. The computer controlled arm was advanced towards a diamond knife in 50 nm increments at a speed of 15 mm s^{-1} to cut electron transparent sections of the epoxy/film (3). The sections were absorbed inside a water droplet onto a holey-Cu TEM grid (4).

a glass knife. The arm was advanced in 50 nm increments at a downward speed of 15 mm s^{-1} to cut (100×200) μm , electron transparent sections by a diamond knife. Different sections were made where the knife cut either perpendicular or parallel to the thin film growth direction. The knife is located at the start of a water trough where the sections float on the surface. Finally, multiple sections were absorbed on the film side of *Pelco 300 Mesh Grid holey-Cu TEM grids*. Cu TEM grids without a holey-C film were also used.

Tripod polishing. Although multiple specimens were prepared using tripod polishing in this work, they were not of the same quality as specimens prepared by ultramicrotomy. Details of the preparation procedure is therefore omitted here, while they are included in §B as a reference for later comparisons of specimens prepared using this technique and ultramicrotomy.

Plasma cleaning. Carbon, coming primarily through the airlock with the insertion of a specimen holder in the TEM, can polymerise on the specimen surface when it is subjected to a high

energy electron beam. This can leave stains in the regions investigated by the beam, rendering the beam immobile to study the underlying material. Hence, additional cleaning was sometimes necessary before a TEM session. Contaminated specimens were cleaned by a low energy, high frequency plasma using a *Fischione Instruments Model 1020 Plasma Cleaner* for 2×30 s. The plasma is created with a 1:4 O:Ar gas mixture within a vacuum chamber. The energy of the plasma ions are about 20 eV. Hence, they remove the weakly bonded contamination on the specimen surface while not altering the crystal structure of the specimen. The contamination particles are then pumped out of the chamber. The specimens were already placed in the TEM specimen holder when plasma cleaned, to be ready for subsequent, immediate insertion into the TEM for investigation.

3.2.2 Scanning electron microscopy sample preparation

Since bulk samples of sizes up to $(4 \times 5 \times 12)$ mm can be studied in the SEM, the sample preparation usually requires less time and effort compared to the preparation for TEM. SEM investigations of specimen *CC* were conducted to study the column growth morphology of the thin films both from the top and side. To obtain a cross-section view of the films, a fast and simple preparation technique⁶³ was used, in which film and substrate fragments are scratched off the substrate surface and dispersed on a TEM mesh grid. First, a droplet of de-ionised water was put on the film surface in the region where scratching was intended. A *Pelco 300 Mesh Grid* holey-C Cu TEM grid was positioned nearby having the C film on the top. The 3 mm-diameter grid has 300 square windows of width 54 μm , and the C layer transmits 40% of the incoming electrons. A fine diamond tip was gently scratched parallel to the GaAs (001) direction of the substrate. Small fragments of film and substrate scratched off were then confined in the water drop. Next, the grid was gently slid under the water drop with a tweezer. When the water drop had dried, the grid contained fragments suitable for SEM observations.

3.3 Characterisation

3.3.1 Transmission electron microscopy studies

The theoretical background on the conventional TEM operation modes covered in §2.2.3 are sufficient to understand the presented results. The acquisition and processing of PED patterns by the novel SPED technique are however covered here in more detail.

Operation modes. The two TEMs *JEOL JEM-2100F* and *JEOL JEM-2100*, part of the Norwegian Centre for Transmission Electron Microscopy (NORTEM) infrastructure at the TEM Gemini Centre, NTNU, Trondheim, were used in this work. The instruments are respectively equipped with a tungsten FEG and a LaB₆ thermionic electron gun, and both were operated at an accelerating voltage of 200 kV. Specimen *AA* was characterised in the 2100F microscope using the operation modes SPED, SAD, BF and DF TEM, HRTEM, BF and ADF STEM and EDS and in the 2100 microscope using the EELS and EFTEM operation modes. The 2100F is fit with an *Oxford X-Max 80 SDD EDX* Si-detector operated via the *AZtec* software for EDS analysis. It has an *2k UltraScan* CCD camera from *Gatan Inc.* for collecting HRTEM, BF and DF TEM images and SAD patterns via the *Digital Micrograph* software. Also available is the *NanoMegs ASTAR* hardware and software package for performing SPED. An *Allied Stingray*

046B ASG camera is mounted in the binocular stand outside the microscope column to collect PED patterns from the microscope viewing screen. The utilized hardware on the 2100 was the *Gatan Image Filter* system for thickness measurements, although it also has an EDS detector, CCD camera and two ADF detectors and one BF detector for STEM imaging. The specimen holders used were a *JEOL EM-31640 Specimen Tilting Beryllium holder* with possibilities for tilting both parallel and orthogonal to its axis up to $\pm 35^\circ$, a *Gatan Model 648 Double tilt analytical holder* and a *JEOL EM-31650SRH31 Specimen Rotation Holder* enabling rotation in the specimen plane. All holders have beryllium closest to the specimen, used because of its weak interaction with X-rays and thus not contributing to the EDS signal.

All BF and DF TEM images were obtained using an electron beam semi-convergence angle of $\alpha = 0.83^\circ$, a medium condenser aperture of $70 \mu\text{m}$ diameter and the smallest available objective aperture of $20 \mu\text{m}$ diameter. SAD patterns were obtained using the same condenser aperture, camera lengths varying from approximately 20 to 50 cm and two different SAD apertures of diameters $70 \mu\text{m}$ and $10 \mu\text{m}$. All BF and ADF STEM images were obtained using a condenser aperture of $50 \mu\text{m}$ and respective camera lengths of 40 cm and 12 cm, while an objective aperture of $20 \mu\text{m}$ was used for the BF images.

Acquisition of scanning precession electron diffraction data. SPED data was acquired while operating the TEM in NBD mode, covered in §2.2.3. To ensure acquisition of localised PED patterns, alignment of the double-rocking movement of the precessing electron probe in the microscope was done following a procedure reported by Barnard *et. al.*⁴¹ It is performed entirely in diffraction mode. The effects of the rocking and precessing movement on the direct beam disk and the ‘shadow’ image of the illuminated area within this disk are minimised, enabling collection of high spatial resolution SPED maps. The goal of the alignment is to coincide both the focal plane of the probe and the pivot point plane of the precessing movement with the specimen plane at the eucentric height. A summary of the procedure in their work, after aligning the microscope in NBD mode, is repeated here:

1. A large illumination aperture was inserted, and the electron probe was over-focused using the condenser lens.
2. A region with highly visible features, e.g. the thin film edge, was found and the precession angle ϕ and precession frequency ω was introduced.
3. A static direct beam CBED disk was obtained by adjusting the de-rocking adjustment below the specimen.
4. The motion of the shadow image within the BF disk was minimised by adjusting the pivot point of the precessing movement above the specimen.
5. The defocus was reduced and steps 3 and 4 were repeated until no further improvement was seen.
6. The probe was refocused using the condenser lens, and the smallest condenser aperture of $10 \mu\text{m}$ was inserted.

Following the above procedure, the precession probe is aligned with typical values for ϕ and ω of respectively $0.5\text{--}1.0^\circ$ and 100 Hz . It is then scanned in a raster, similar to a STEM probe, across a rectangular region of interest of typically $(1 - 500 \times 1 - 500)$ probe positions. A spatial sampling of typically $1\text{--}10\text{ nm/px}$ is chosen, depending on the size of the features under study, like small grains in a polycrystalline material. A suitable exposure time of the external camera is chosen to match an integer number of complete precessions. The probe dwell time equals the exposure time. A PED pattern of (144×144) px and 8 bits per px is then recorded per probe position. The reciprocal space PED patterns are rotated $\sim 16^\circ$ clockwise with respect to the real space rectangular region of interest, due to the projection by the TEM lenses of the PED diffraction patterns onto the viewing screen. Values for the considered parameters, used to acquire a SPED dataset from specimen *AA*, are shown in Tab. 3.2.

Table 3.2: Parameters used to acquire a SPED dataset from specimen *AA*.

Parameter	Value
Probe spot size	1.0 nm
Semi-convergence angle α	1.0 mrad
Camera length	30 cm
Precession angle ϕ	0.5°
Precession frequency ω	100 Hz
Probe positions	333×365
Probe step length	2.4 nm
Exposure time	10 ms

3.3.2 Scanning electron microscopy studies

A *Hitachi S-5500* SEM was also used in this work. The instrument is equipped with a cold, tungsten FEG electron source and was operated at an accelerating voltage of 5.0 kV and a beam current of $10\text{ }\mu\text{A}$. It is located in the NTNU NanoLab cleanroom, one of four cleanrooms within the Norwegian Micro- and Nanofabrication Facility (NorFab). Although also equipped with BF, DF and STEM detectors, only the SE detector was used to investigate the column growth of the 100 nm thick specimen *CC*. The sample holder used is made for TEM specimens with possibilities for tilting orthogonal to its axis up to $\pm 27^\circ$.

3.4 Data processing

A world of information of a material can be extracted from the localised diffraction patterns in a SPED dataset. NanoMegas' ASTAR software was used to acquire the PED patterns, create a template bank of simulated diffraction patterns and perform template matching. The matching resulted in a map of one orientation per diffraction pattern or real space pixel and a correlation index Q and its reliability R . This map was analysed in the open source, Matlab texture toolbox MTEX^{49,64} to obtain texture information and a grain size distribution. The localised PED patterns were analysed in the open source, Python multi-dimensional data analysis toolbox HyperSpy⁶⁵ to obtain virtual images and perform decomposition. An acquired EDS map was also analysed using the HyperSpy software. In order to extract interplanar lattice spacings of crystalline phases present in the thin films, the camera length used when acquiring SAD patterns needs to be calibrated. An SAD pattern from the known Au nanoparticle specimen was therefore

acquired at the same nominal camera length and lens voltages in the same session as when acquiring a pattern from specimen *AA*. An SAD pattern from the particles has already been shown in Fig. 2.7 (a), and a BF TEM image and texture information from the same specimen was used in §2.4 in the theoretical discussion of crystal texture analysis. The processing steps are discussed here, while relevant source code is included in the appendices §C.

3.4.1 Crystal structure determination

To enable acquisition of two separate SAD patterns from Au particles and a YHO thin film with the same lens voltages, the grid with particles was placed underneath the grid with film in the same specimen holder. Only the height of the specimen holder in the microscope was changed between the acquisition of the two patterns. By providing the pixel coordinates of the direct beam (000) reflection, the 2D patterns were radially integrated to give 1D patterns. Since the interplanar spacings d in the Au particles are known, the position of the diffraction beams \mathbf{g} can be measured in pixels from the direct beam. By considering that electrons are scattered through an angle 2θ at the specimen, this distance (R) as measured in the pattern can be related to the camera length L , i.e. the distance from the specimen to the camera, as $R/L = \tan 2\theta \sim \theta$. The Bragg law in Eq. (2.13) gives $\lambda/d = 2 \sin \theta \sim 2\theta$, yielding the relation $Rd = \lambda L$. Since L and λ are the same for both patterns, the interplanar spacings d in the pattern from YHO can be calculated. A code snippet showing how 1D diffraction patterns were constructed in this work is included in §C.1.

3.4.2 Virtual imaging

Virtual BF or DF images were formed by integrating intensities inside virtual apertures or annuli placed in a PED pattern stack. Examples from the Au nanoparticle dataset were shown in Fig. 2.12 (b,c,d,e). The HyperSpy software enables integration inside an arbitrary number of apertures or annuli of arbitrary pixel size. Hence, once the SPED dataset is acquired, any VBF or VDF images can be formed to highlight features of interest.

3.4.3 Multivariate statistical analysis

The HyperSpy software also facilitates multivariate statistical analysis of multi-dimensional data through decomposition algorithms like PCA, blind source separation or NMF.⁶⁵ Theoretical discussions of PCA and NMF were covered in §2.5. PCA was used in this work to describe the proportion of variance of principal components, i.e. component patterns, in the SPED dataset from specimen *AA*. Based on a lower threshold of the variance proportion, the number of principal components in the dataset considered as signal was set, discarding the principal components below this threshold as noise. A subsequent NMF decomposition was then performed, only keeping the signal components. Examples of component patterns and loading maps from the Au nanoparticle dataset were shown in Fig. 2.21 (b,c,f,g,h).

3.4.4 Crystal orientation determination

Using NanoMegs' ASTAR hardware and software package,⁶⁶ maps of one PED pattern per probe position was acquired. The local crystallographic orientation and phase are identified by

comparison of the recorded spot patterns with simulated spot patterns for all possible orientations and phases,^{38,67} as shown in Fig. 3.2. To create a template bank, a crystal structure is described by providing the type of atoms, atom positions and crystallographic space group. The template bank is stored as projected sections of the kinematically simulated reciprocal space of the crystal structure.

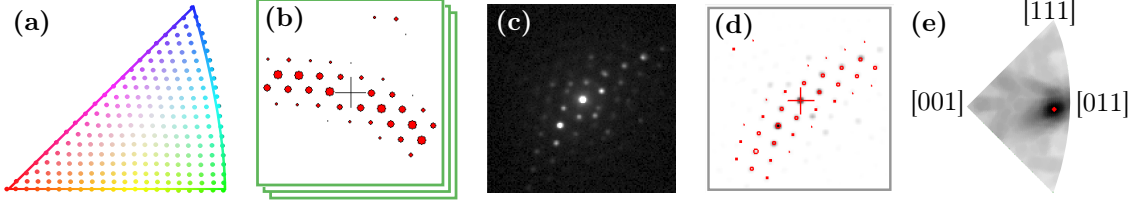


Figure 3.2: Example of pattern matching of the Au nanoparticles. Templates (a,b) are generated for all orientations over the stereographic triangle. An experimental pattern acquired per pixel (c) is compared to every simulated template (d). The correlation index density map shows the best match, i.e. the most probable orientation, in the double IPF. Adapted from Rauch et. al.³⁸

The template approach reduces the identification process to an image recognition problem similar to human fingerprint indexing. Each reflection in the experimental pattern or template is characterised by a position (x, y) and an intensity. The image *correlation index* Q is calculated for every template as

$$Q_i = \frac{\sum_{j=1}^m P(x_j, y_j) T_i(x_j, y_j)}{\sqrt{\sum_{j=1}^m P^2(x_j, y_j)} \sqrt{\sum_{j=1}^m T_i^2(x_j, y_j)}}, \quad (3.1)$$

where the diffraction pattern is represented by the intensity function $P(x, y)$ and every template i is given by the function $T_i(x, y)$. The highest Q value is selected as the solution. However, the validity of the proposed orientation/phase is questionable in particular for overlapping grains, since the template matching always provides a solution. The *reliability* parameter R given as

$$R = 100 \left(1 - \frac{Q_{\text{next best}}}{Q_{\text{best}}} \right), \quad (3.2)$$

is designed to address this issue. The ACOM-TEM approach thus gives every probe position a phase, orientation in Euler angles, index Q and reliability R . This approach was used to create orientation maps of specimen AA. The orientation data was exported from the ASTAR software for subsequent processing in the MTEX software.

3.4.5 Orientation data filtering and grain reconstruction

MTEX was used to inspect and represent texture information from the SPED dataset of specimen AA. Examples of explorable phenomena directly linked to texture are grain size, shape and location, misorientation between grains and the distribution of grain boundary geometry, orientation variations within individual grains and phase relationships.⁴⁵ The orientation data from the acquired SPED dataset of specimen AA consist of $333 \times 365 = 121\,545$ orientations in Euler angles. First, the dataset was cropped to only contain the region of interest, so the number of orientation measurements were reduced from 121 545 to 91 168. In order to filter the

measurements, all measurements with an index score Q_i below half of the mean index Q_{mean} were excluded, and 90% of the 91 168 measurements passed the filtering.

The FMC algorithm,⁵⁰ as mentioned in §2.4, was used in this work for grain reconstruction in both the datasets from specimen *AA* and from the Au nanoparticle example dataset. The algorithm separates data points into some number of groups and determines boundaries by searching the dataset for adjacent points that belong to different groups, also allowing for the segmentation sensitivity to be set by the user in a parameter C . As the value of C is increased, the number of clusters or grains in the final segmentation increases and the average variance within the grains decreases. As C increases the grains start at some point to be oversegmented, so determining an optimal C value is not a simple variance minimization problem. Since the decrease in average variation within a grain when it is segmented is much smaller than the decrease that results from separating two distinct grains, diminishing returns in the increase of cluster quality are expected as C is increased beyond its optimal value. So, by computing the clustering solution for a range of C values and calculating the average variance of orientations within clusters for each C , a plot of average variance versus C can be examined. This was done for both datasets, and the plot created for the Au particle dataset is shown in Fig. 3.3. Subsequently, two line segments, meeting at a breakpoint are fit to the data, indicating the best combination of linear fits. The C value at the location of the breakpoint is selected as the optimal orientation cluster segmentation sensitivity. The filtered, reconstructed grains in Fig. 4.17 (a) are calculated from the obtained optimal value of $C = 1.3$.⁵⁰

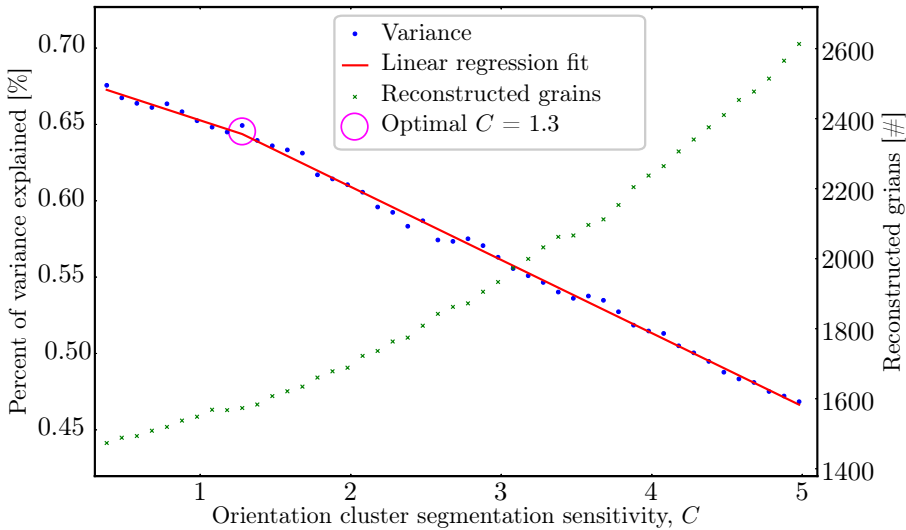


Figure 3.3: The average variance of orientations within clusters calculated for each segmentation sensitivity value C of the Au specimen dataset. A slight ‘elbow’ of the segmented linear regression fit, indicated by the circle, determines the optimal segmentation sensitivity of $C = 1.3$.

The reconstructed grains were filtered by excluding grains at the image boundary as their areas were considered to be underestimated. Also excluded were grains where less than 25% of measurements had a reliability higher than 15%. That measurements with a reliability above 15% are reliable was suggested by Rauch *et. al.*⁶⁷ Longer code snippets showing the aforementioned steps to process and analyse the orientation data of specimen *AA* are included

in §C.2 and §C.3.

3.4.6 Energy-dispersive X-ray spectroscopy quantification

Processing and analysis of an EDS map acquired from specimen *AA* was done in the HyperSpy software. It allows for quantification of at.% through the Cliff-Lorimer ratio technique⁴² or the ζ -factor method.⁴³ Only the yttrium and oxygen signals were considered in the Cliff-Lorimer quantification. The theoretical k factors used for the O K_α and Y L_α peaks in the quantification were obtained from the Oxford *AZtec* software. They were respectively 1.997 and 1.754. Code snippets showing how this quantification was done are included in §C.4 and §C.5.

3.4.7 Image processing

All images from the SEM and TEM were ‘de-speckled’ in the image analysis software *ImageJ*⁶⁸ by smoothing out pixels considered to have extreme values. For easier comparison of features in different DF TEM images obtained from the same region of interest, each image was coloured either red, green, blue or yellow and then summed to give one image. The colouring and summation was done in Python using the image processing package *scikit-image*.⁶⁹ Also, FFTs of HRTEM images were created using the FFT function in Gatan’s Digital Micrograph.⁷⁰ The 2D plotting library *Matplotlib*⁷¹ implemented in Python have been used extensively in this thesis, and all figures have been created using the vector graphics editor *Inkscape*.⁷²

4 | Results

The column growth morphology of YHO films *CC*, *BB* and *AA* are shown in SE, BF TEM, DF TEM, BF STEM and ADF STEM images. The crystal structure of *AA* is then presented in SAD and SPED patterns, VBF and VDF images and decomposed component patterns and corresponding loading maps. The film texture and grain size distribution are presented from analysis of the crystal orientation information from the same SPED dataset. Elemental composition along the film thickness from EDS analysis of *AA* is then given. Differences in the quality of TEM specimens obtained via ultramicrotomy and tripod polishing are presented last. The results are discussed in §5.

4.1 Column growth morphology

SE images from YHO specimen *CC* in the SEM, shown in Fig. 4.1, were obtained to get an overview of the material and study its top (a, c) and cross-section (b) morphology. The top surface is rough and faceted with voids between the ~ 75 nm wide column tops. The column tops exhibit smaller features (c). The film cross-section shows a smooth film bottom where it has delaminated from the substrate during sample preparation. The column growth seems to dominate from 200-300 nm and up. The dark streak across the cross-section (b) is an image artefact in the fast scan direction.

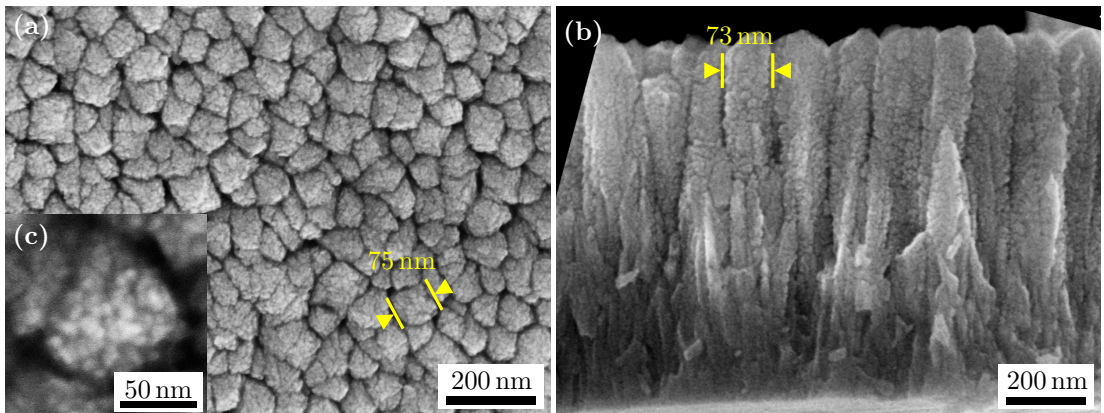


Figure 4.1: Column growth morphology in SE images of the top (a) and side (b) of fragments from YHO sample *CC* with the column width indicated. The column tops (c) exhibit smaller features.

Specimen *BB* was directly deposited on a holey-C Cu grid to study the top-bottom projection of the film in the TEM, shown in BF (a) and coloured DF (b) TEM images in Fig. 4.2. The BF image shows contrast from difference in mass, thickness or diffraction strength. Some dark regions have defined edges, and the regions are in general smaller than the column tops in Fig. 4.1. The diffracted electrons from multiple crystals in the same area are shown in the inset SAD pattern (c) (results from studies of the crystal structure are presented in §4.2). Three DF images were constructed by selecting two (111) reflections (red) and one (200) reflection (green) with a 20 μm objective aperture. The coloured sum of these three images (b) shows that there is no 1-1 correspondence between dark regions in the BF image and light regions in the DF images, highlighted by the yellow circle around the same region in the two images.

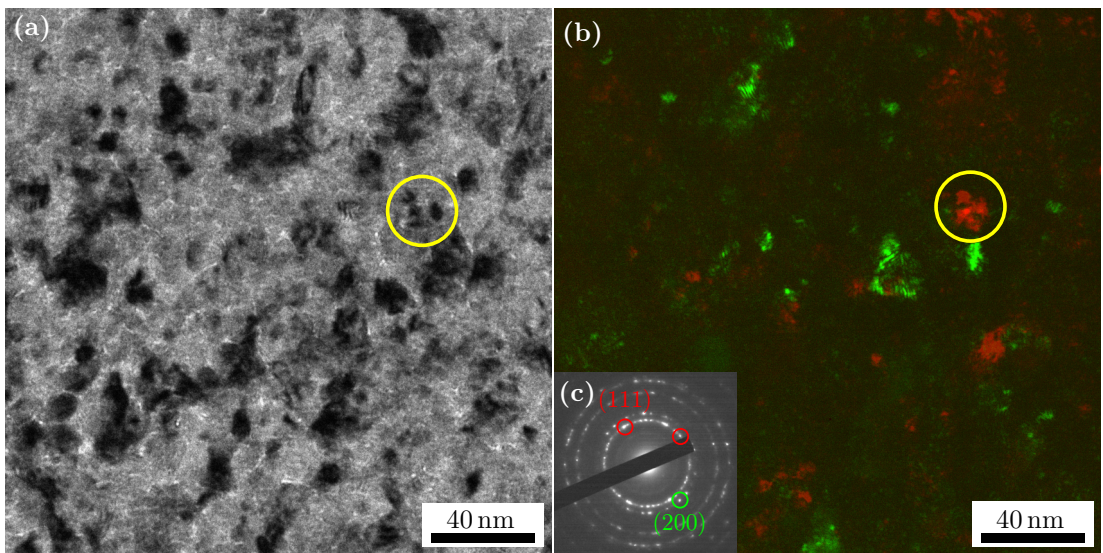


Figure 4.2: Top-bottom projection of the same area of YHO plan-view specimen *BB* in a BF TEM image (a) and a stack of three coloured DF TEM images (b). The DF images are constructed by selecting two (111) reflections (red) and one (200) (green) in the SAD pattern (c) from the same area.

The 650 nm thick, ultramicrotomed YHO specimen *AA* that easily delaminated from its Si substrate enables studies of large electron transparent regions, as shown in BF (a) and coloured DF (b) TEM images in Fig. 4.3. Most results presented in this work were obtained from studying the particular depicted film, including the film's crystal structure, texture, grain size distribution and elemental composition. The BF image (a) shows how the film is attached only to the embedding epoxy from ultramicrotomy sectioning at the top, while the bottom is free. The full as-deposited film seems to have survived specimen preparation without notable artefacts in a 700 nm wide region. Defined columns comprised of multiple crystals are seen in the sum of four coloured DF images (b) constructed by selecting reflections (111) (red), (200) (green), (220) (blue) and (311) (yellow) in turn with the 20 μm objective aperture. The bottom shows a finer crystal structure with a strong (200) reflection. As interpreted from the SE images in Fig. 4.1 is the column growth dominant from 200-300 nm and up. The darker region in the middle of the film seen in the BF image most likely comes from a non-crystalline, contaminating carbon particle, since the same region shows contrast from diffuse scattering in the DF image.

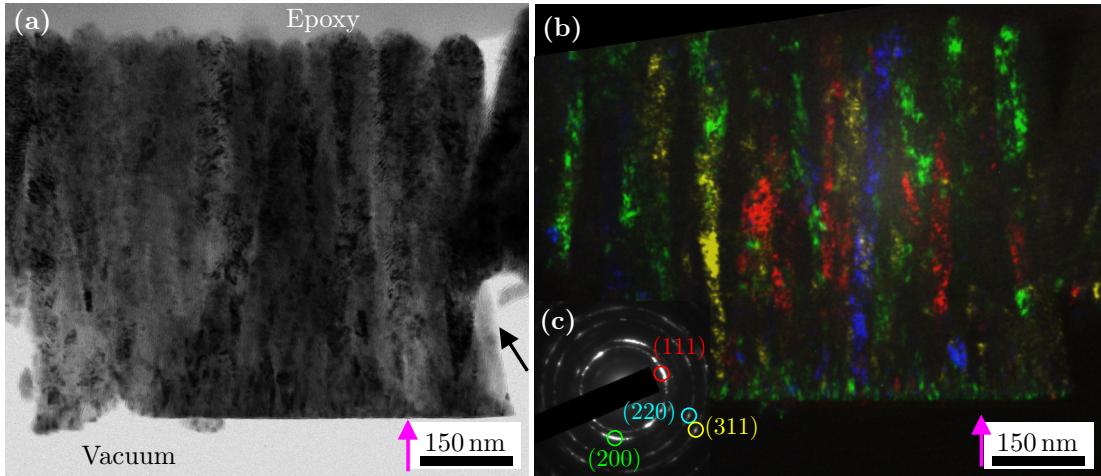


Figure 4.3: Column growth morphology of YHO specimen AA in BF TEM image (a) and stack of four coloured DF TEM images (b). The DF images are constructed by selecting reflections (111) (red), (200) (green), (220) (blue) and (311) (yellow) in the SAD pattern (c) from the same area. Most results presented in this work were obtained from studying this particular film region. The pink arrows point to a column and column boundary imaged in BF and ADF STEM mode shown in Fig. 4.4, while the black arrow points to a thin area imaged in HRTEM mode shown in Fig. 4.5.

The black arrow in Fig. 4.3 (a) points to a thin region imaged at a high resolution as shown in Fig. 4.5, while the pink arrows (a,b) point to a particular column and column boundary between two columns imaged in STEM mode in detail in Fig. 4.4. Seven stitched BF (a) and ADF (b) STEM images in Fig. 4.4 show respectively bright and dark lines inside what seems to be a single column. These lines, highlighted by red arrows at the bottom and towards the top, are indicative of voids in the structure, but do not follow the column growth direction. It is difficult to discern if the lines at the bottom and top are the same type of structures. As is also evident from the BF TEM image in Fig. 4.3 (a) there is less material between the columns than inside the columns, as seen in the ADF STEM image. Also, the morphology of the column tops and side seems almost ‘dendritic-like’ in nature. The column boundary left of the column in (a,b) is shown in eight stitched BF (c) and ADF (d) STEM images. It is difficult to say if more than two columns are imaged, however it looks like only two columns. The dendritic-like growth mode where the columns seem to try to fill in the voids between them is evident from 200-300 nm and up, the onset highlighted by the green arrows. However, both columns seem to have started growing from 100 nm or so. The first 10 nm of the film bottom look denser and seem to have less voids than the film just above it.

4.2 Crystal structure

To study the polycrystalline nature of specimen AA, high resolution images, SAD patterns and a SPED dataset was acquired. The HRTEM image in Fig. 4.5 (c) was acquired from the lower right part of the film indicated by the black arrow in Fig. 4.3 (a). Both translational and rotational moiré fringes, described in §2.2.3, can be seen all over the film, meaning that the electron beam has penetrated multiple, differently oriented, nanoscale crystals in one of the

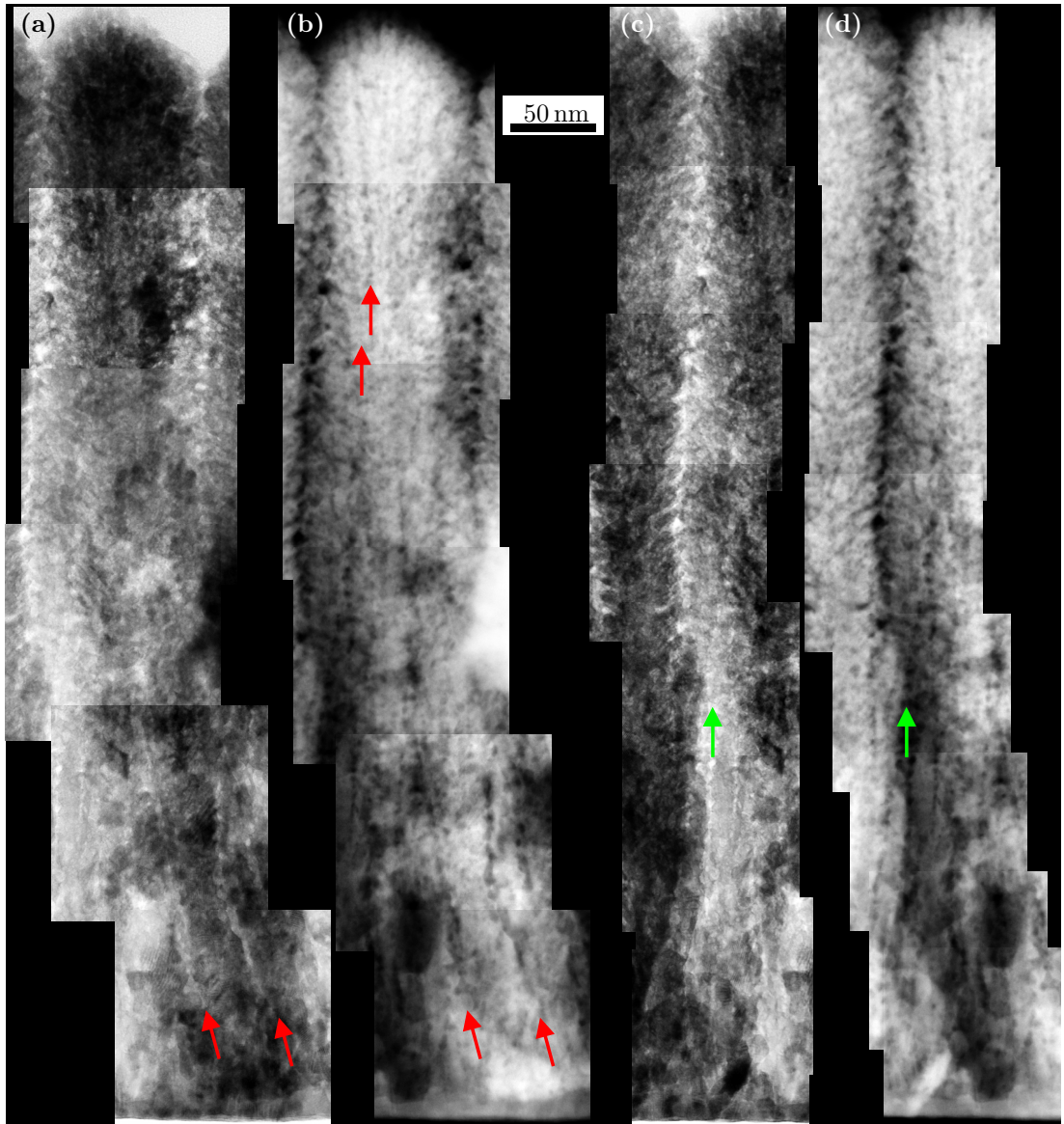


Figure 4.4: Voids and dendritic-like morphology in a column (a,b) and column boundary (c,d) of specimen AA in seven stitched BF (a) and ADF (b) STEM images and eight stitched BF (c) and ADF (d) STEM images. The particular column and column boundary imaged is highlighted by the pink arrows in Fig. 4.3. The BF and ADF images were not stitched together to give two images because of a too large difference in contrast, again because of different acquisition parameters.

thinnest regions of the film. The lower, white arrow in (a) highlights, in addition to indicate the film growth direction, a line resembling the lines in the STEM images in Fig. 4.4 and a bright, faceted structure. Whether this is an amorphous oxide phase or just a thinner region than

the surrounding material is difficult to say from the image. It has an approximate diameter of 10 nm. The uppermost, pink arrow in (a) highlights another line similar to the lines in the STEM images of much smaller features than the faceted structure. A difference in frequencies or reflections in the FFTs from the upper (b) and lower (c) 25 nm² squares in the image support the assumption of nanoscale crystals. The six-fold reflections in the blue circles in (b) are not present in the same circles in (c). Also, the yellow circles highlight reflections resembling a [212] fcc structure, showing that moiré fringes from multiple sets of crystals contribute to the FFT reflections.

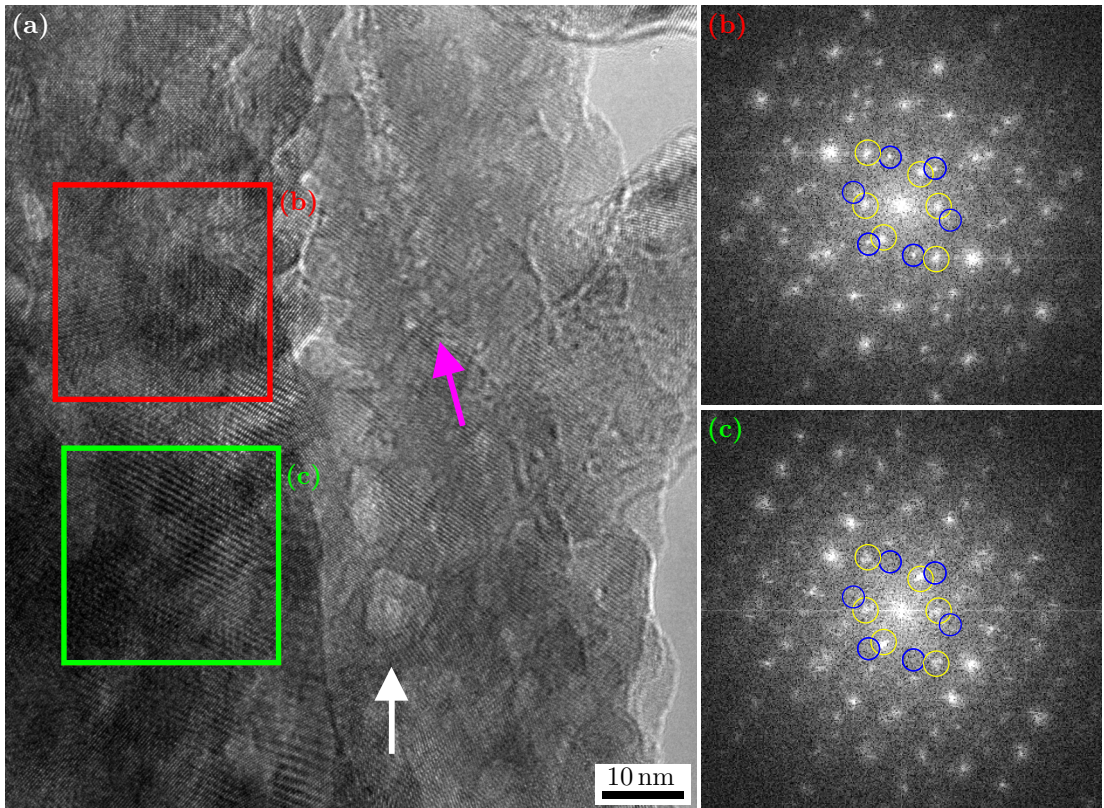


Figure 4.5: Moiré fringes and other phase contrast mechanisms in an HRTEM image (a) of a lower, right region of specimen AA indicated by the black arrow in Fig. 4.3 (a). FFTs (b,c) of the two squares in the image show different sets of reflections. The white arrow highlights a faceted structure of a 10 nm diameter and the pink arrow highlights a line of smaller features.

An SAD pattern of diffracted electrons from the full film region of AA was acquired in an attempt to determine the crystal phases present. The results are presented in Fig. 4.6. An SAD pattern from the Au nanoparticle specimen (a) with an fcc structure and lattice parameter $a = 4.0782 \text{ \AA}$, as discussed in §3.3.1, was used as calibration of the camera length in the same microscope session with similar lens voltages. The four closest packing lattice planes of this structure are highlighted in (a). A 1D plot of diffraction intensity was produced by radially integrating the intensities in the YHO ring pattern (b). The peaks possible to identify, above the background from diffuse electron scattering, are listed in Tab. 4.1. A kinematically simulated

SAD pattern for fcc YH_2 with a lattice parameter of $a = 5.2055 \text{ \AA}$, as reported by Daou and Vajda,⁷³ is included for comparison. Values for the first ten of these lattice planes are also found in Tab. 4.1, in addition to values of $1/d$ for fcc Y_2O_3 with a lattice parameter of $a = 10.60 \text{ \AA}$, as reported by Antic *et. al.*⁷⁴

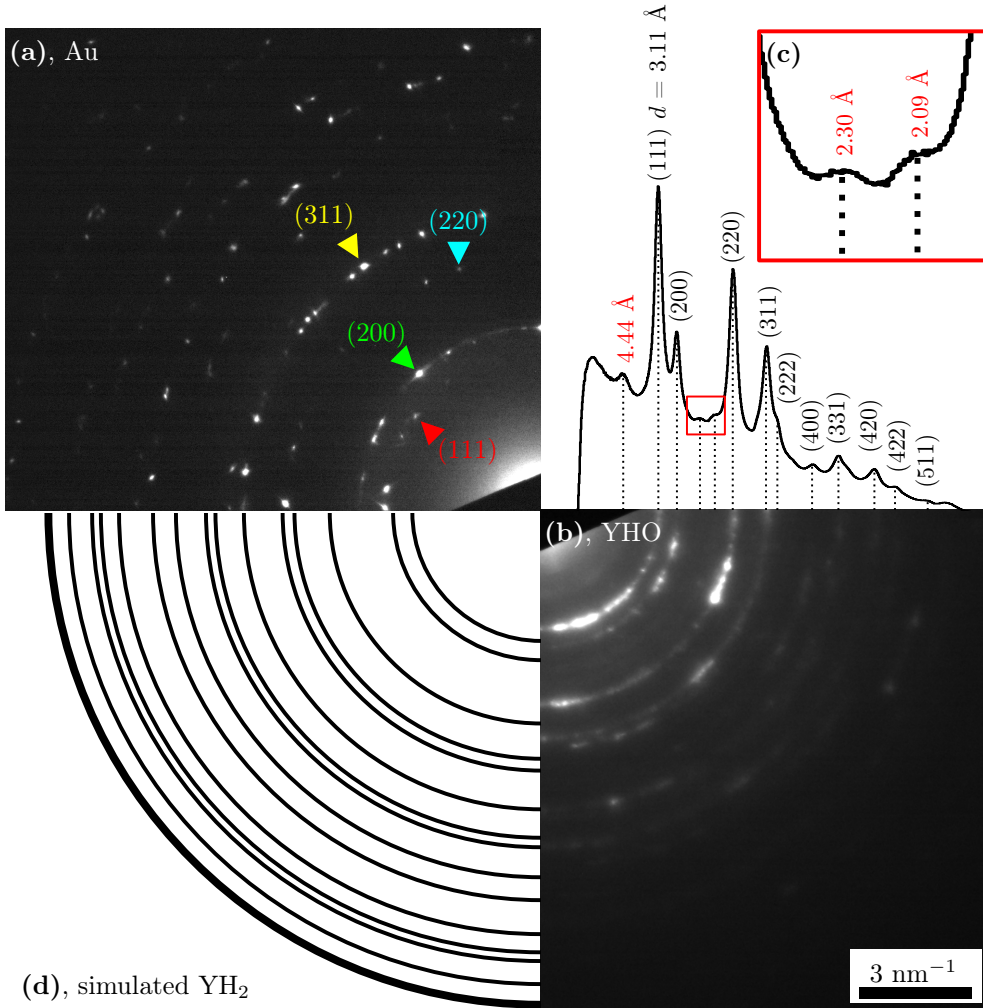


Figure 4.6: SAD patterns from the Au specimen (a) and thin film specimen AA (b). The Au pattern is used to calibrate the scale bar, which is the same for all patterns. A kinematically simulated DP for YH_2 (d) with $a = 5.20 \text{ \AA}$ is included for comparison. Three peaks not matching the YH_2 structure are found, highlighted in red text, two of them in (c).

Ten peaks in Fig. 4.6 (b,c) are identified as an expanded YH_2 fcc lattice with an average lattice parameter of $a_{\text{mean}} = (5.39 \pm 0.04) \text{ \AA}$. The error is two standard deviations of the normal distribution of the ten peaks. Three peaks not matching this structure are highlighted in the 1D pattern with red text and in the zoomed in inset (c). The ratio of the first and second peak $4.44/2.3 = 1.93$ matches the ratio of the principal spot spacings $\{111\}$ and $\{311\}$ of the fcc

structure. The YHO rings exhibit brighter regions indicating a strong thin film texture.

Table 4.1: Identified diffraction peaks in the SAD pattern acquired from the YHO specimen AA shown in Fig. 4.6 (b,c). Also listed are interplanar spacings d , lattice parameters a and corresponding lattice planes (hkl) calculated from the identified peaks in the YHO pattern. Tabulated values for relevant interplanar spacings d for fcc YH_2 ⁷³ and fcc Y_2O_3 ⁷⁴ are included for comparison.

Peak d [Å]	YH_2 d [hkl] (Å)	Y_2O_3 d [hkl] (Å)	YHO a [(hkl) Å]
4.44	—	—	—
3.11	(111) 3.01	(311) 3.20	(111) 5.39
2.68	(200) 2.60	(400) 2.65	(200) 5.36
2.30	—	(420) 2.37	—
2.09	—	(511) 2.04	—
1.90	220 (1.84)	—	(220) 5.37
1.62	311 (1.57)	—	(311) 5.37
1.57	222 (1.50)	—	(222) 5.44
1.35	400 (1.30)	—	(400) 5.40
1.23	331 (1.19)	—	(331) 5.36
1.21	420 (1.16)	—	(420) 5.41
1.10	422 (1.06)	—	(422) 5.39
1.04	511 (1.00)	—	(511) 5.40
			(5.39 ± 0.04) Å

By focusing the probe in NBD mode as discussed in §3.3.1, localised PED patterns was acquired in a (364 × 332) nm square with a step size of 2.4 nm to cover the full region of interest. Fig. 4.7 shows a VBF image (a) constructed by integrating the intensities inside a virtual aperture of a 10 px radius in all 120 848 acquired PED patterns (real space pixels). The aperture is seen in the summed PED pattern stack (b) around the direct beam, removed from the image to enhance the contrast of dimmer reflections. The epoxy is brighter than the vacuum in the VBF because the direct beam pixels are saturated and the diffuse scattering of electrons from the epoxy adds to the intensity around the direct beam inside the aperture.

The small grains in the film bottom and the column growth seen in the DF TEM image in Fig. 4.3 (b) can also be seen in the VDF image in Fig. 4.8 (a). It was constructed from integrating the intensity inside two apertures of a 3 px radius on the (111) ring in all patterns, indicated in the selected pattern (b). This pattern was acquired from the top of the film indicated by the oversized red square in (a). The best matching simulated pattern (c) shows that the most dominant reflections in the experimental pattern belong to a crystal oriented with its [101] plane normal parallel to the beam direction. The patterns are simulated based on an expanded YH_2 fcc lattice with a lattice parameter of $a = 5.39$ Å, as determined from studying the SAD pattern in Fig. 4.6. No oxygen was included in the simulated structure. The patterns were also compared to simulated patterns from the tabulated structures of the YH_2 fcc lattice and the Y_2O_3 fcc lattice. However, these comparisons returned much lower matching results. Note the very small, lone grains like the ones highlighted by the green circle in (a), indicating a varying grain size in the film.

Similar examples of VDF images (a-c), selected PED patterns (d-f) and best matching simulated patterns (g-i) are shown in Fig. 4.9. Two VDF images constructed from two (220) reflections

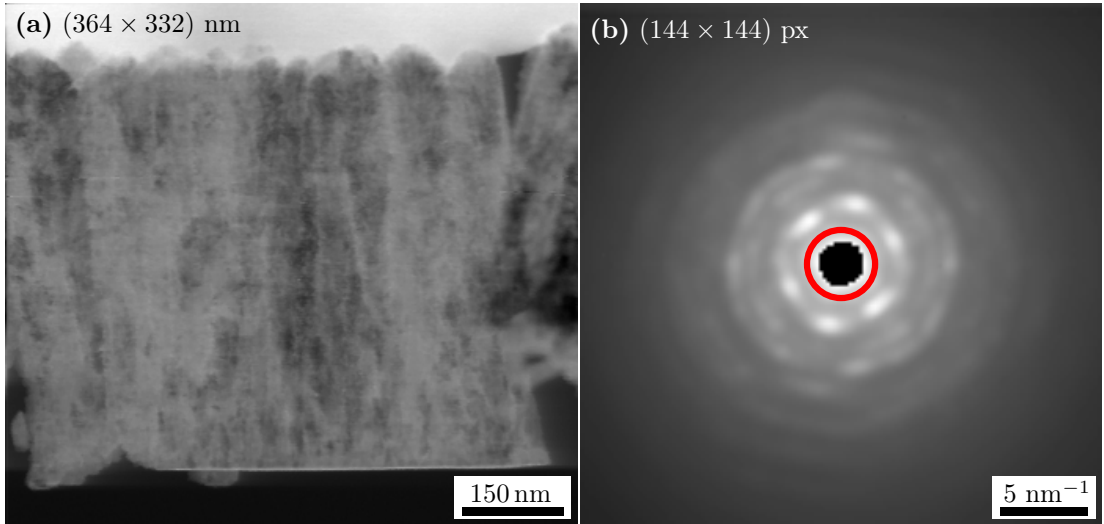


Figure 4.7: VBF image (a) of specimen AA constructed from integrating the intensity inside the virtual aperture of a 10 px radius in the summed PED pattern stack (b). The direct beam is masked out to enhance the intensity of dimmer reflections.

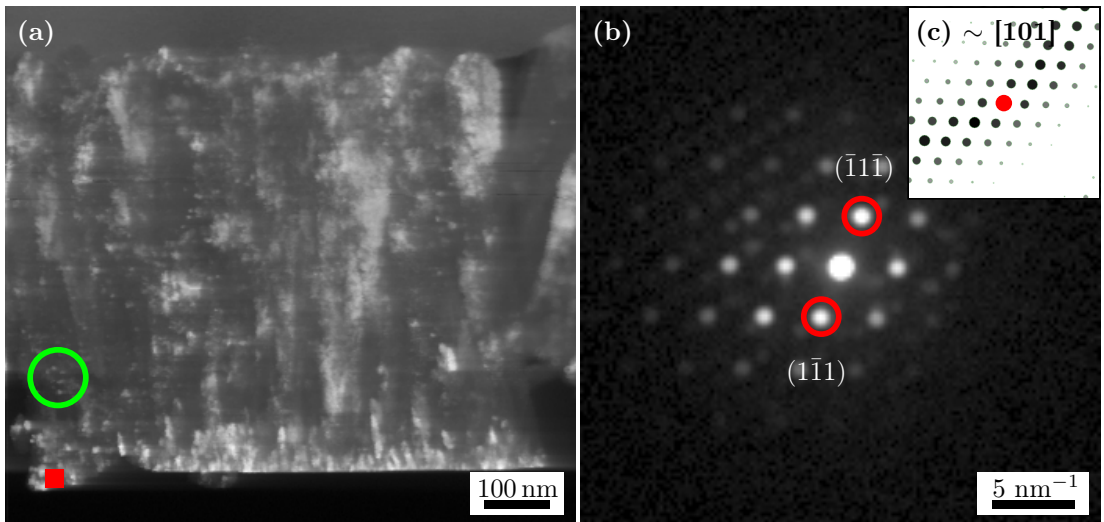


Figure 4.8: Columns and grains in a VDF image (a) constructed from integrating intensities inside the virtual apertures of a 3 px radius in all PED patterns, indicated in the selected pattern (b). A kinematically simulated DP (c) show the best crystal orientation match to the recorded pattern. The pattern was acquired from the region indicated by the oversized red square in the VDF image.

(a,c) show overlapping columns highlighted by the pink triangles near the film top. Two other overlapping columns can be seen in one of those VDF images (c) and another VDF image (b) constructed from two (111) reflections, highlighted by the green triangles.

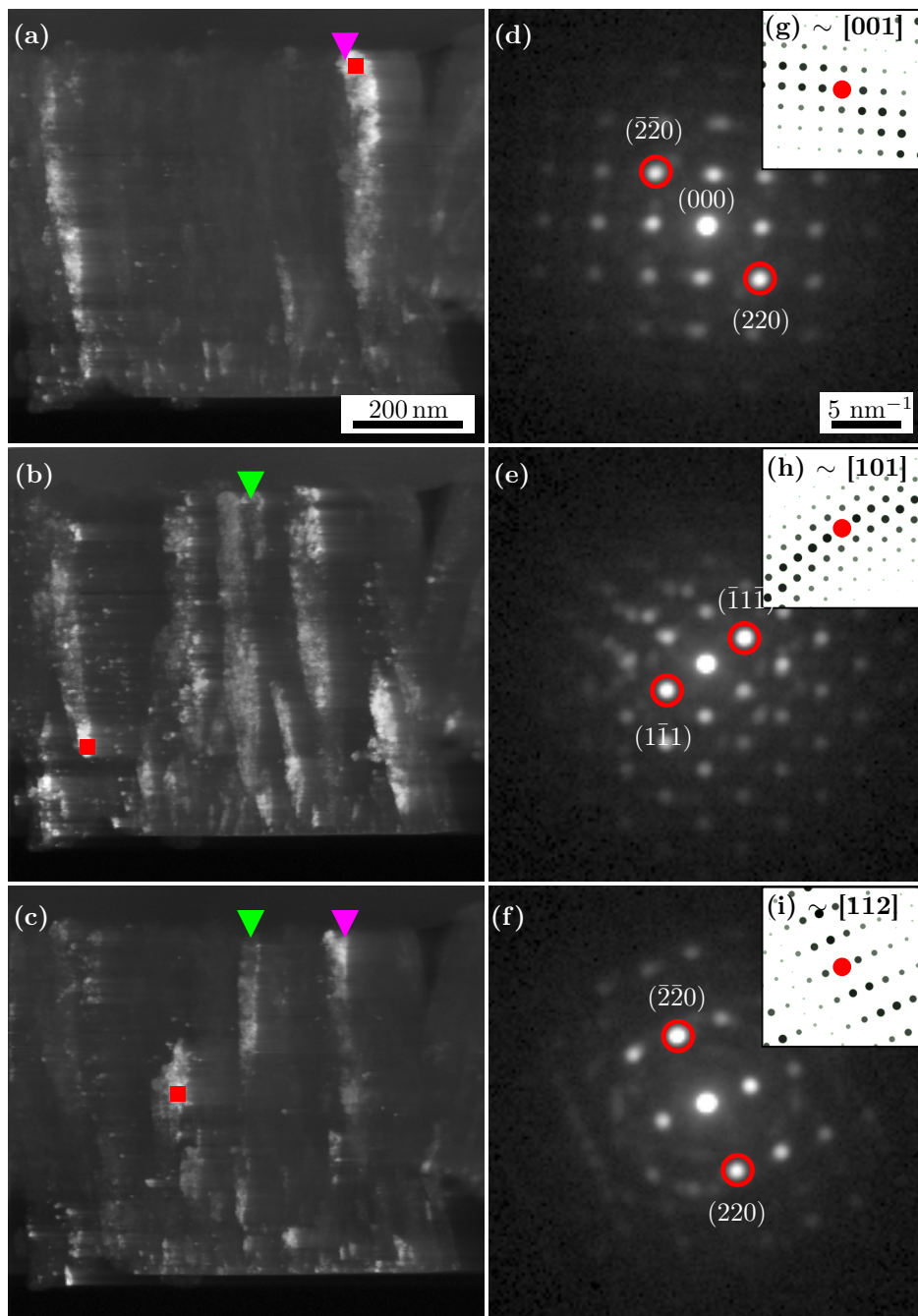


Figure 4.9: Columns and grains shown in VDF images (a-c) constructed from integrating intensities inside virtual apertures of a 3 px radius in all PED patterns, indicated in the selected patterns (d-f). Kinematically simulated DPs (g-i) show the best crystal orientation match to the recorded patterns. Scale bars in (a) and (d) apply to (a-c) and (d-f), respectively. The patterns (d-f) were acquired from the regions indicated by the oversized red squares in the VDF images.

In an attempt to separate the diffracted intensities for each orientation and/or phase in the SPED dataset, it was decomposed using PCA and NMF algorithms. A plot of the proportion of variance as a function of principal components returned by the PCA decomposition, known as a Scree plot, is shown in Fig. 4.10. A lower threshold for explained variance was set to 10^{-3} for the subsequent NMF decomposition, thus keeping the first 40 components and discarding the rest as noise. Component patterns #0 (a) and #40 (b) from the PCA decomposition are included as examples to show the difficulty of a physical interpretation of PCA components, compared to NMF components as will be shown below. The brighter disk in the #0 component above the direct beam is an inherent consequence of damage to the fluorescent viewing screen of the microscope.

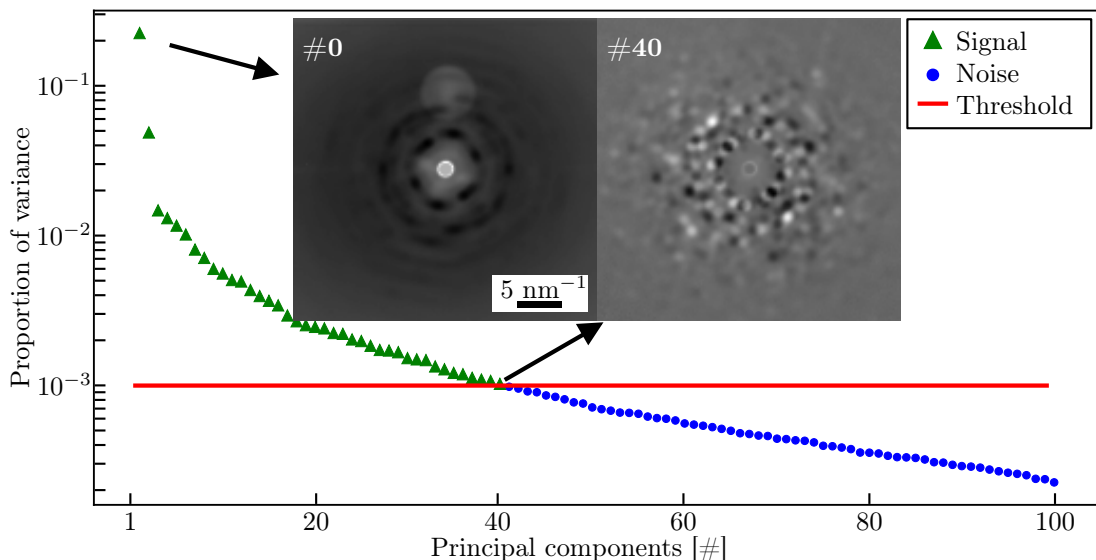


Figure 4.10: Proportion of variance as a function of principal components from a PCA decomposition, known as a Scree plot, of the SPED dataset from AA. Component patterns #0 (a) and #40 (b) are shown. The lower threshold for explained variance was set to 10^{-3} .

The NMF decomposition approximated the SPED dataset by a linear combination of non-negative component patterns and corresponding loading maps, only keeping the first 40 components. In addition to try to separate orientations and phases, another motivation for the decomposition was to learn the ‘true’, underlying component patterns in an unbiased manner, meaning that the decomposition shows what information ‘really’ is in the 120 848 patterns. Fig. 4.11 shows component patterns #8 (c) and #24 (d) and corresponding loading maps (a,b), while Fig. 4.12 shows component patterns #26 (c) and #28 (d) and corresponding loading maps (a,b). All patterns, selected because of the loading maps’ clear outlines of column growth and structures of different sizes and shapes, show dominant (111) reflections. This is representative for most of the 40 decomposed patterns. Note the resemblance between loading map #8 and the VDF image in Fig. 4.9 (b). This is perhaps not surprising when considering that the virtual apertures and the intensities assigned to component pattern #8 are in the same pixel positions. As explained in §2.5 has the NMF decomposition reduced the noise in the component patterns, and their loading maps show columns and grains more clearly than VDF

images.

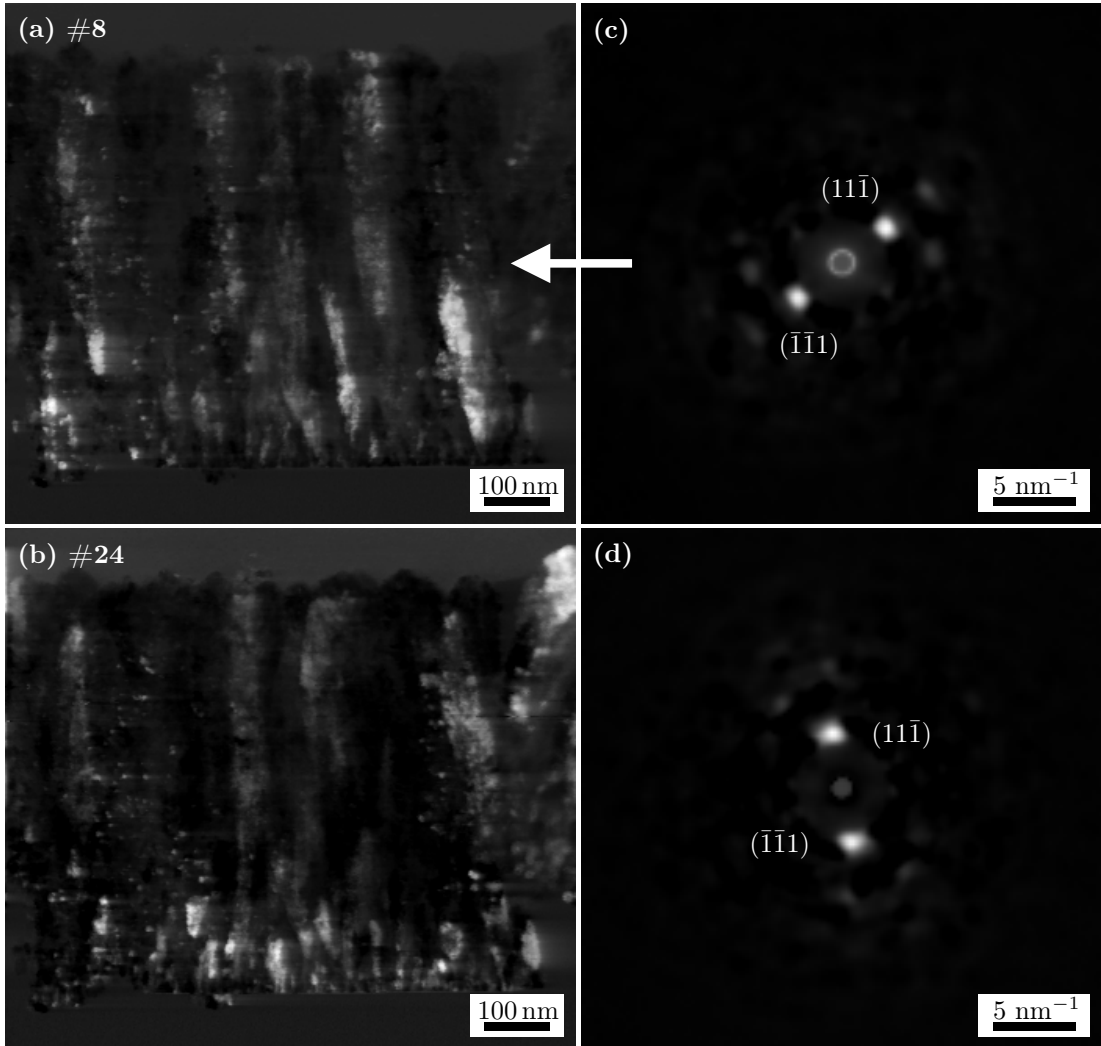


Figure 4.11: Columns and grains in loading maps (a,b) and component patterns #8 (c) and #24 (d) from an NMF decomposition of the SPED dataset acquired from AA.

4.3 Thin film texture

The localised PED patterns acquired from specimen AA enables determination of the orientation of the crystals giving the brightest reflections in each probe position. Thus, maps of crystal orientation relative to the thin film growth direction can be created. Similar orientations can also be clustered into grains, enabling studies of grain size and the misorientations between grains. The quality of the dataset is presented first, followed by the orientation maps and a subset of orientations plotted into IPFs, PFs and calculated ODFs. The reconstruction of grains

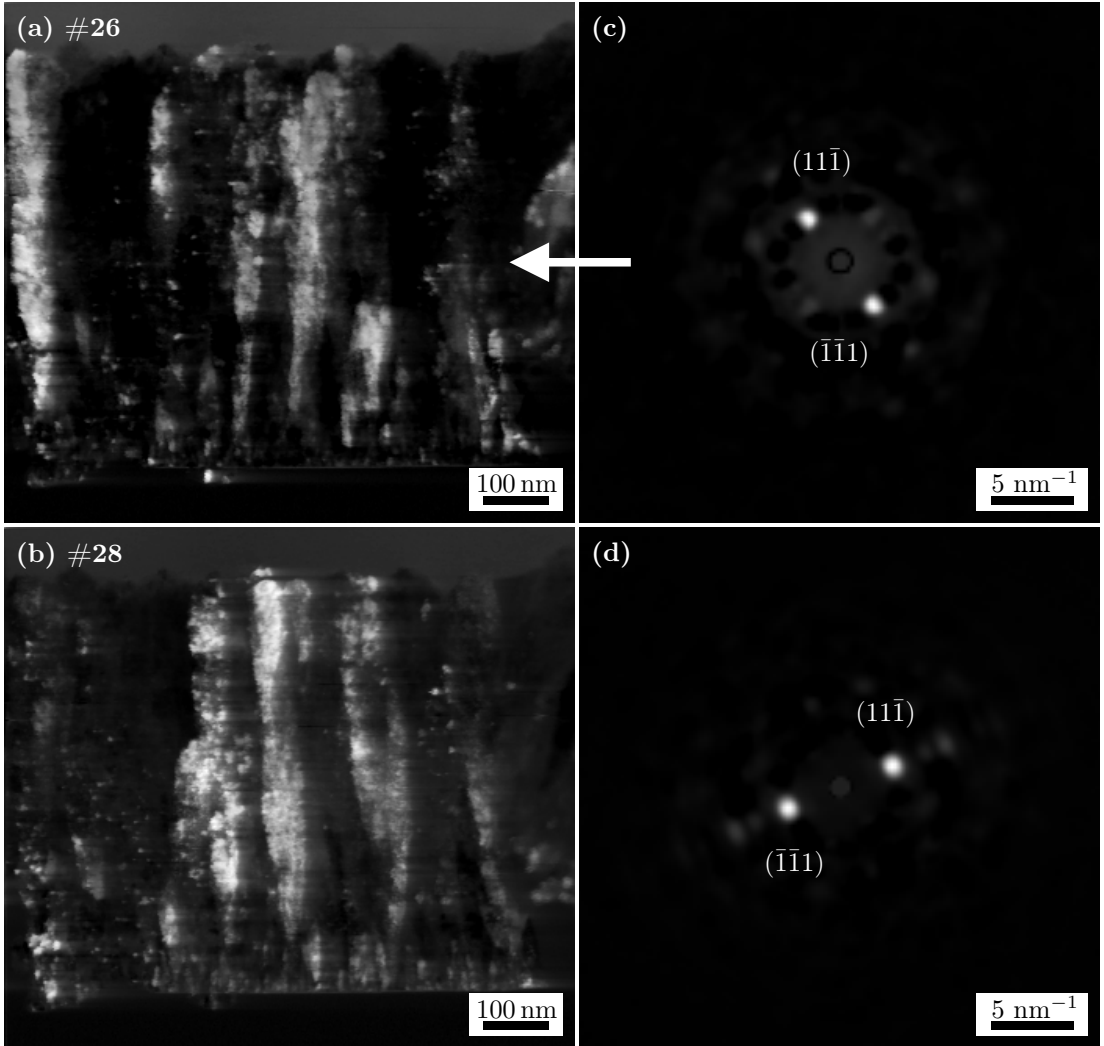


Figure 4.12: Columns and grains in loading maps (a,b) and component patterns #26 (c) and #28 (d) from an NMF decomposition of the SPED dataset acquired from AA.

and misorientation analysis is then presented in §4.4.

As explained in §2.4.2 is each pattern or real space pixel, after matching to simulated patterns, assigned a correlation index Q of the best match and a reliability R comparing the best and second best match. Maps of these values normalised to 100 are shown in Fig. 4.13, with mean values of $Q_{\text{mean}} = 40.20$ and $R_{\text{mean}} = 22.75$. Values of Q and R seem in general to correlate well, with low values in the film bottom where there are multiple, smaller grains and high values in the columns. This is however not the case in a middle region of the film, indicated by the pink triangle in both maps. Two PED patterns from regions of low reliability highlighted by the red (c) and green (d) oversized squares in the reliability map (b) are included in Fig. 4.13.

The match between the simulated and the experimental patterns, plotted as a density map in the IPF, show multiple dark regions indicating a good match, leading to a low reliability.

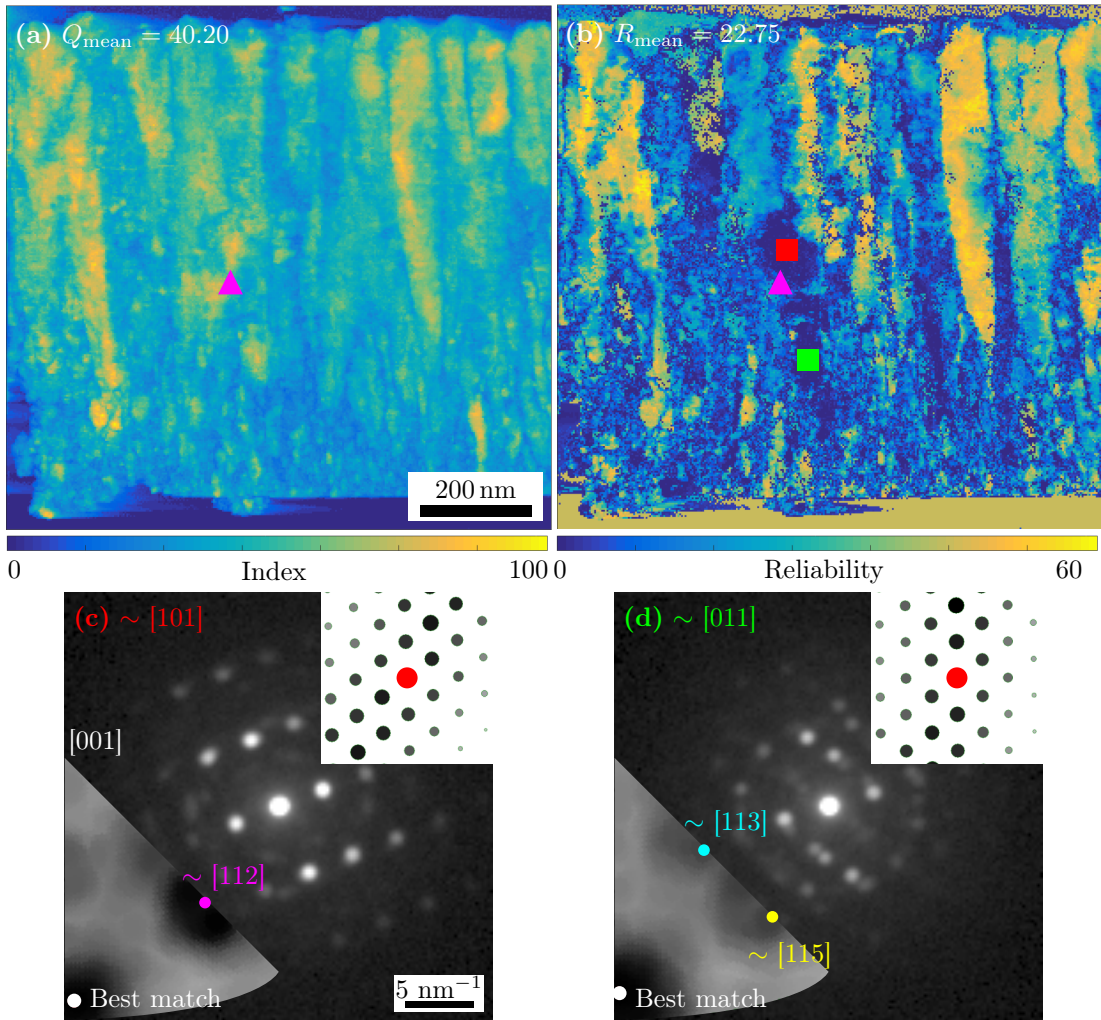


Figure 4.13: Quality of template matching in maps (low-high, blue-yellow) of the correlation index Q (a) and the reliability R (b) in each pixel of AA. The match between simulated and two experimental PED patterns (c,d), plotted as density maps in IPFs, show multiple dark regions indicating a good match, leading to a low reliability. The best match is indicated with a white dot in the IPF with the simulated pattern also inset.

Filtered orientation maps in Fig. 4.14 show a clear trend in thin film texture. Subsets of all crystal coordinates viewed along each specimen direction ($\mathbf{x}, \mathbf{y}, \mathbf{z}$), indicated in the figure, are also plotted into one IPF for each orientation map. Crystals in an approximate region from 0-50 nm have their [111] plane normals stacked near parallel to the growth direction, i.e. the specimen direction \mathbf{y} . No column growth seems to start in this region. In an approximate region from 50-250 nm, some larger structures, of similar orientation within the structures, start to

grow. However, the large column structure with similar orientations dominate only from 250 nm and up. The z orientation map show that most grains have their $[011]$ planes oriented near parallel to the beam direction, but the systematic clustering in the corresponding IPF suggests that this might be an artefact from the template matching rather than a preferred orientation.

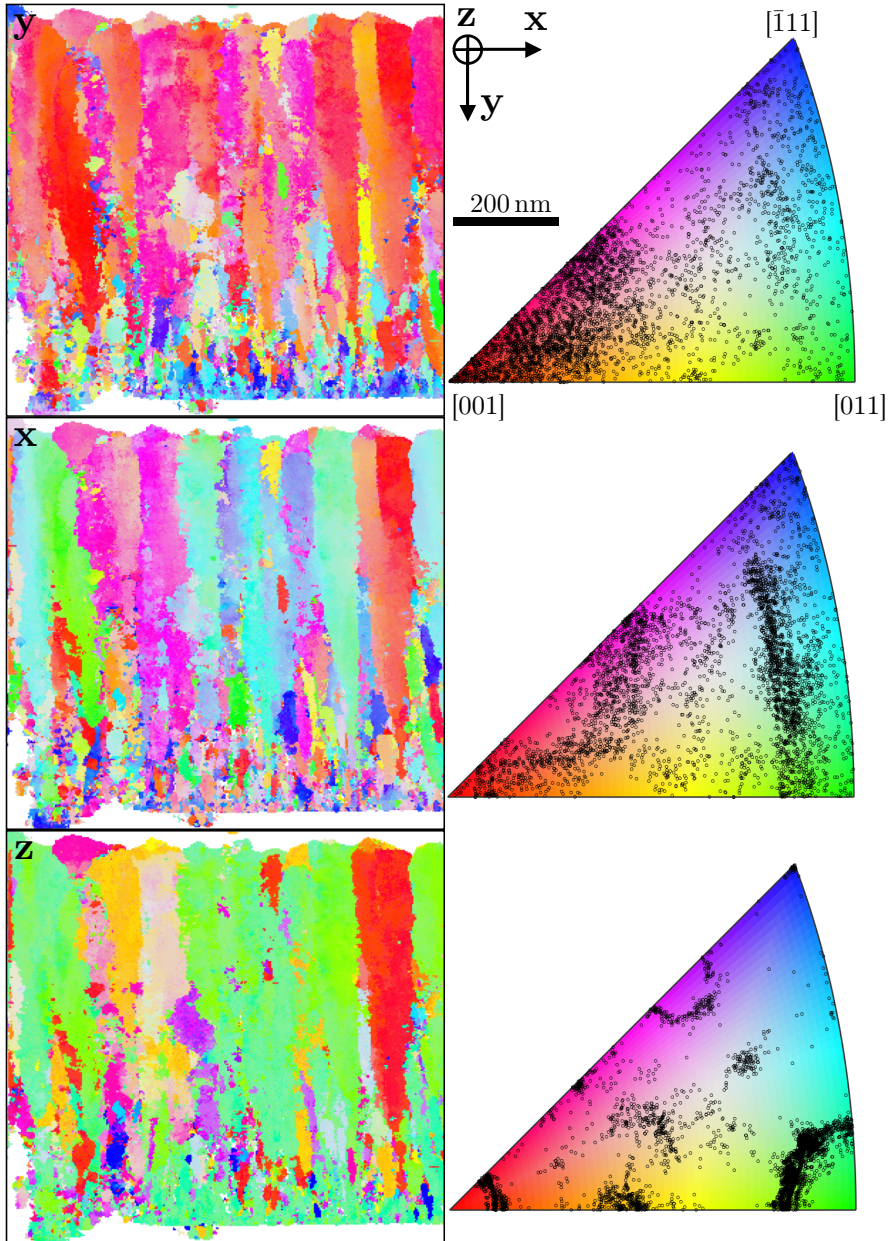


Figure 4.14: Filtered orientation maps and corresponding IPFs of specimen AA in the indicated specimen coordinates y , x and z . Subsets of all crystal coordinates viewed along each specimen coordinate are plotted into one IPF for each orientation map.

Subsets of crystal coordinates are also plotted into $[001]$, $[011]$, $[\bar{1}11]$ and $[\bar{1}12]$ pole figures with the specimen coordinates indicated, shown in Fig. 4.15. ODFs, also shown in the figure, are calculated from all crystal coordinates to ease the interpretation of the pole figures. The probability densities in the colour bars show multiple, preferable orientation directions for each major, lattice plane normals. A pronounced symmetry along a line at a low angle to the growth direction Y is observed for all pole figures and ODFs, as expected when considering the $[001]$ texture in this direction. The low angle to the growth direction Y comes from the misalignment between the recorded PED patterns and the rectangular region of interest, as explained in §3.3.1.

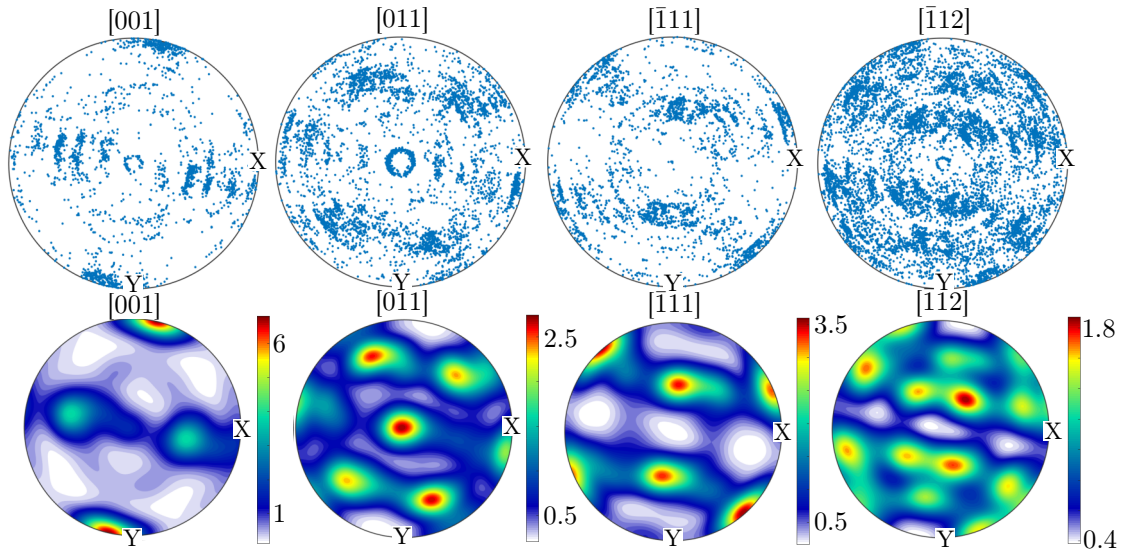


Figure 4.15: $[001]$, $[011]$, $[\bar{1}11]$ and $[\bar{1}12]$ pole figures of subsets of all crystal coordinates and calculated ODFs of AA relative to its specimen coordinates indicated in Fig. 4.14. The colour bars indicate probability density from low (blue) to high (red).

4.4 Grain size and misorientations

Grains are reconstructed using the FMC algorithm in MTEX as explained in §3.4.5. The search for the optimal segmentation sensitivity C is shown in Fig. 4.16, with the optimal value being $C = 2.6$. This segmentation leads to a total of 3421 grains, but the subsequent filtering of grains at the boundary and grains with a low reliability resulted in 1699 reliably reconstructed grains. Grain boundaries of the filtered, reconstructed grains are shown in Fig. 4.17 (a), on top of the y orientation map. Due to the low reliability of crystal orientation mapping in the bottom region of the film, these grains have been discarded from the dataset. Regions of similar orientations, like the columns with a $[001]$ texture, have been reconstructed into multiple grains both large and small. The mean grain size is (14.8 ± 1.6) nm with two standard deviations, calculated from a lognormal distribution fit to the equivalent diameter of the projected grain areas (b). Grains as large as 250 nm in diameter are reconstructed, however the largest portion of grain sizes are between 0 and 40 nm.

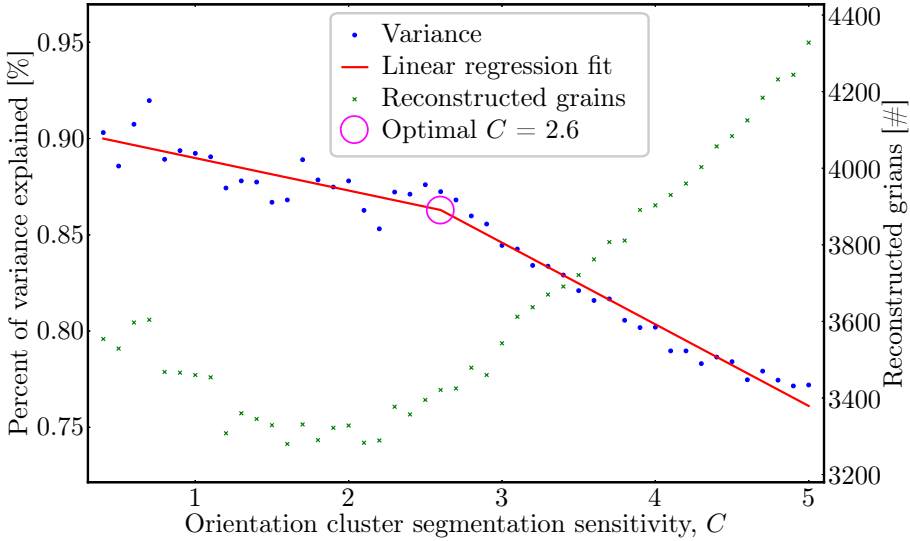


Figure 4.16: The average variance of orientations within clusters calculated for each segmentation sensitivity value C for AA. The ‘elbow’ of the segmented linear regression fit, indicated by the circle, determines the optimal segmentation sensitivity of $C = 2.6$.

The misorientations of adjacent grains are shown in Fig. 4.18 (a). The grain boundaries are coloured according to the misorientation angle in ranges, plotted on top of a black and white correlation index map (black-white, low-high). The ranges are $< 20^\circ$ (blue), 20° to 40° (green) and $> 40^\circ$. Regions of high index show low misorientation angles, both within and between column grains. Grains in the bottom lack misorientation angles in the medium range, while this range is more prominent in grains in the region from 100-300 nm, at least in the right part of the film. The misorientation of each measurement to the mean orientation of the grain it is assigned to are shown in Fig. 4.18 (b) with grain boundaries in white. Large misorientation to mean orientations (blue-yellow, low-high) are prominent in reconstructed grains in the film bottom, and these grains have been discarded from the dataset almost without exception.

The distribution of misorientation angles is shown in Fig. 4.19 (a), with a random distribution assuming no orientation relationships between grains included for comparison. A high density of misorientations between grains from 10° to 20° can be seen, and a fairly continuous distribution of all other misorientations. That the two distributions are so different indicates an orientation relationship between the reconstructed grains. The misorientation axis distribution, i.e. which axes these misorientation angles are transformed around to map one grain into the adjacent grain, is shown in Fig. 4.19 (c) together with a random distribution in (b). The experimental distribution shows a higher density around the $[001]$ and $[\bar{1}11]$ axes and a lower density around the $[011]$ axis than the random distribution.

To assess variations in orientations across column boundaries, inside columns and across the smaller structures in the film bottom, misorientations in measurements along lines across the regions of interest are shown in Fig. 4.20. The variation in orientation of measurements relative to the first measurement is plotted (a,e,h) as well as the gradient of change. The correlation

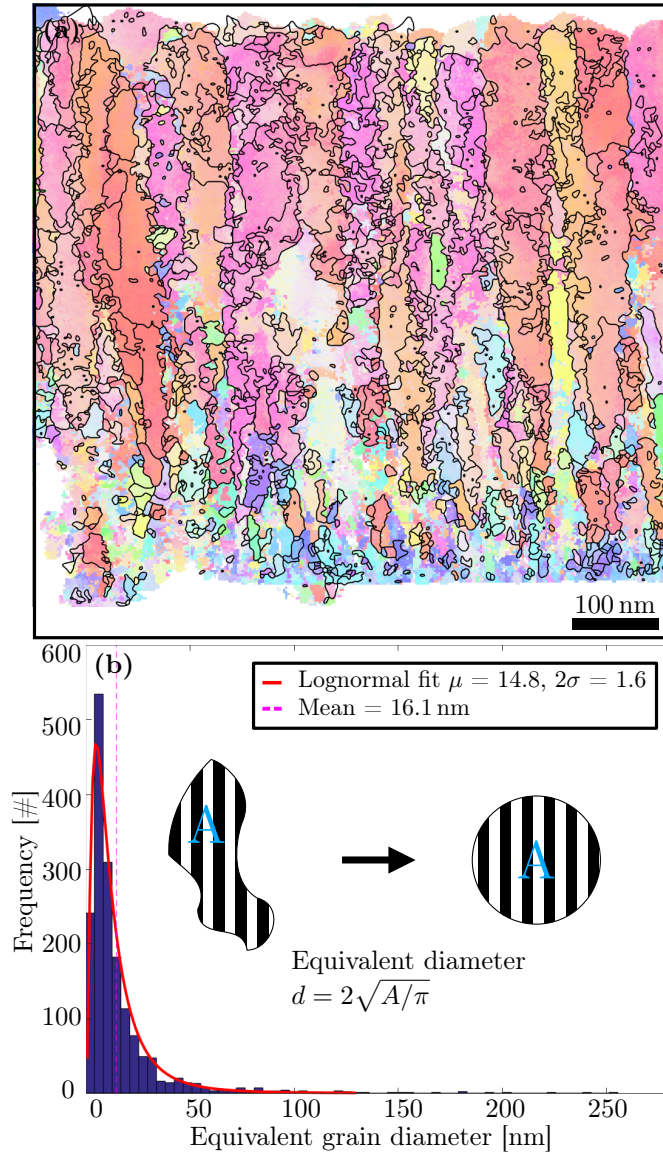


Figure 4.17: Reconstructed grain boundaries (a) using the FMC algorithm, on top of the y orientation map for AA. Grains with a low reliability from crystal orientation mapping have been discarded from the dataset. A lognormal distribution is fit to the grain size distribution (b), showing a mean grain size of (14.8 ± 1.6) nm.

index Q_i and reliability R_i is also plotted for each measurement. The plotting lines are shown on top of BF TEM images (b,c,i) and y orientation maps. The plots show a misorientation of up to $\sim 40^\circ$ across the column boundaries and $\sim 10^\circ$ to 20° inside the column. Both these lines are ~ 100 nm long. Many, abrupt changes in orientations of up to 60° are observed across the film bottom, in a line of length ~ 120 nm. Both the index and reliability can be seen to drop

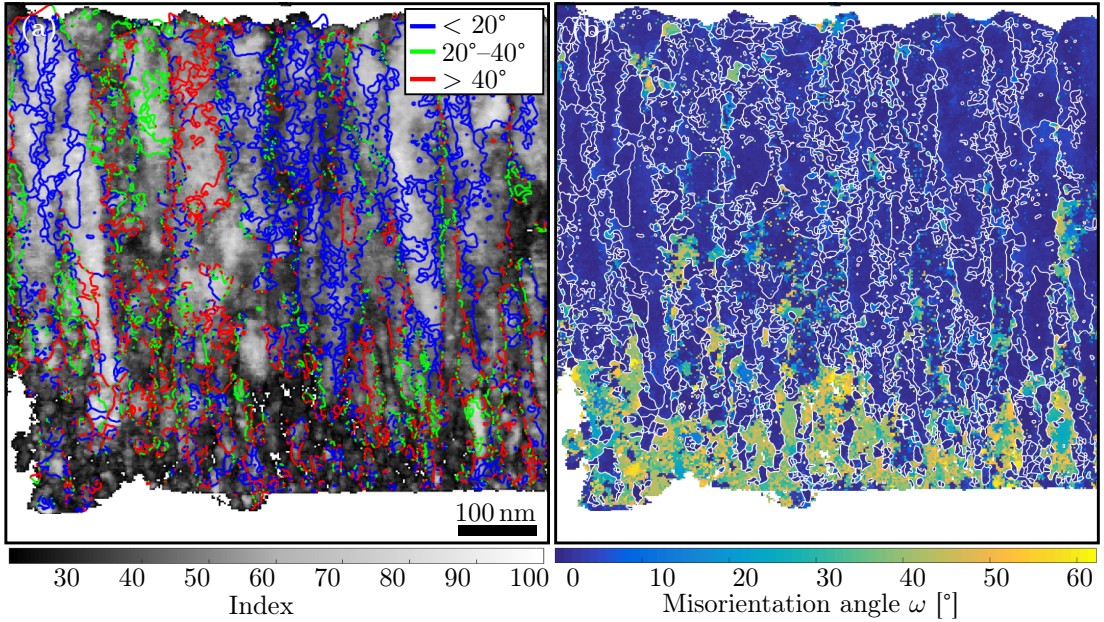


Figure 4.18: Grain boundaries coloured according to misorientation angle ranges on top of the correlation index map (a) for AA. The regions with highest index top left and right exhibit lowest misorientation angles (blue) between grains. The misorientation to mean orientation of measurements within reconstructed grains (b) are largest for those in the film bottom. Grain boundaries coloured white in (b).

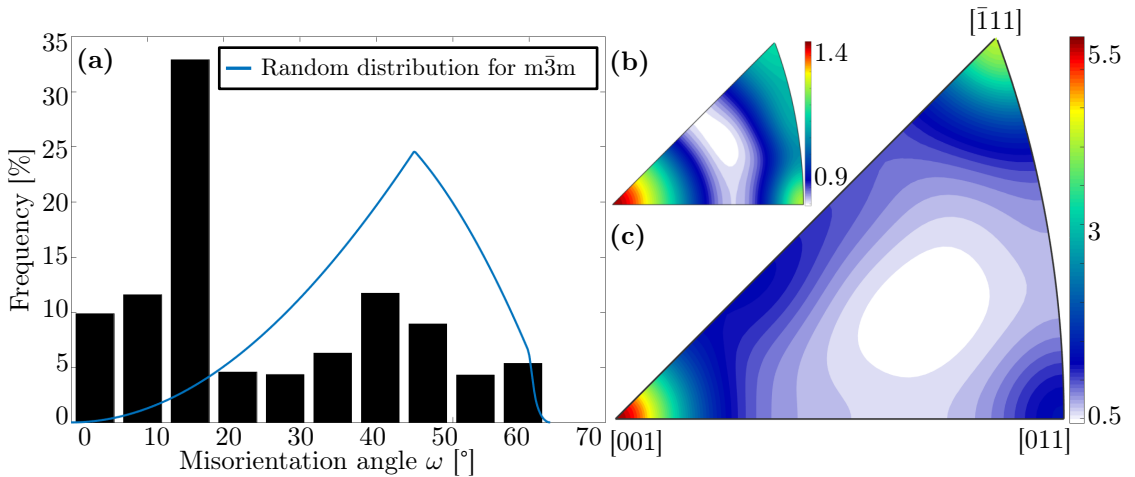


Figure 4.19: The misorientation angle distribution (a) and misorientation axis distribution (c) for AA. A random distribution (b), assuming no orientation relationships between grains, is included for comparison.

at changes in orientation along all three lines. They are however lowest in the film bottom.

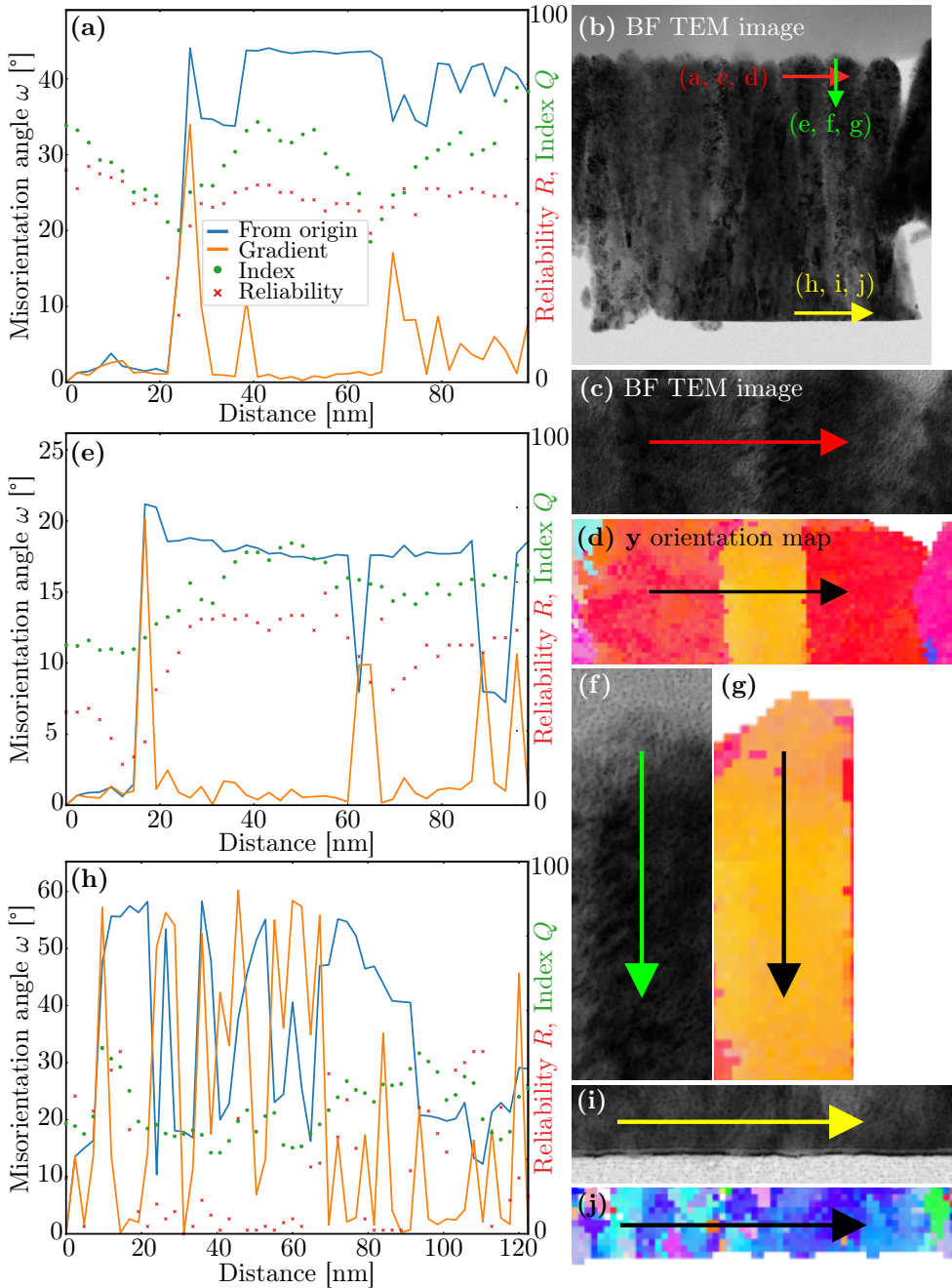


Figure 4.20: The variation in orientation of measurements relative to the first measurement across two column boundaries (c,d), inside a column (f,g) and across the grains in the film bottom (i,j) for AA is plotted (a,e,h) as well as the gradient of change. The correlation index Q_i (green) and reliability R_i (red) is also plotted for each measurement. The misorientation lines are indicated in the BF TEM images and y orientation maps.

4.5 Elemental composition

Since theoretical studies⁵⁶ have suggested that a change in the band gap of the film is related to the increased oxygen concentration in the films, an analysis of the elemental composition is of importance. Hence, characteristic X-rays emitted from specimen *AA* were detected. The electron beam was focused to a probe in STEM mode and scanned across the region of interest in a raster, while an EDS spectrum was acquired for each probe position. The resulting map is of 512^2 probe positions or a region of 922^2 nm, with a total of 7 110 538 X-rays detected. A sum of all spectra is shown in Fig. 4.21 with peak intensities labelled. Also shown is a map of the density of X-rays counted per probe position with a maximum of around 350. The Cu peaks are expected as these come from the microscope itself and the TEM grid, while the C peak can come from both the epoxy from specimen preparation and the film in the grid windows. The Si peak can come from both the detector and the substrate, but the fact that it is rather low suggest that the film is almost completely free of the substrate. Of interest are the O and Y signals, at respectively 0.52 keV and 1.92 keV.

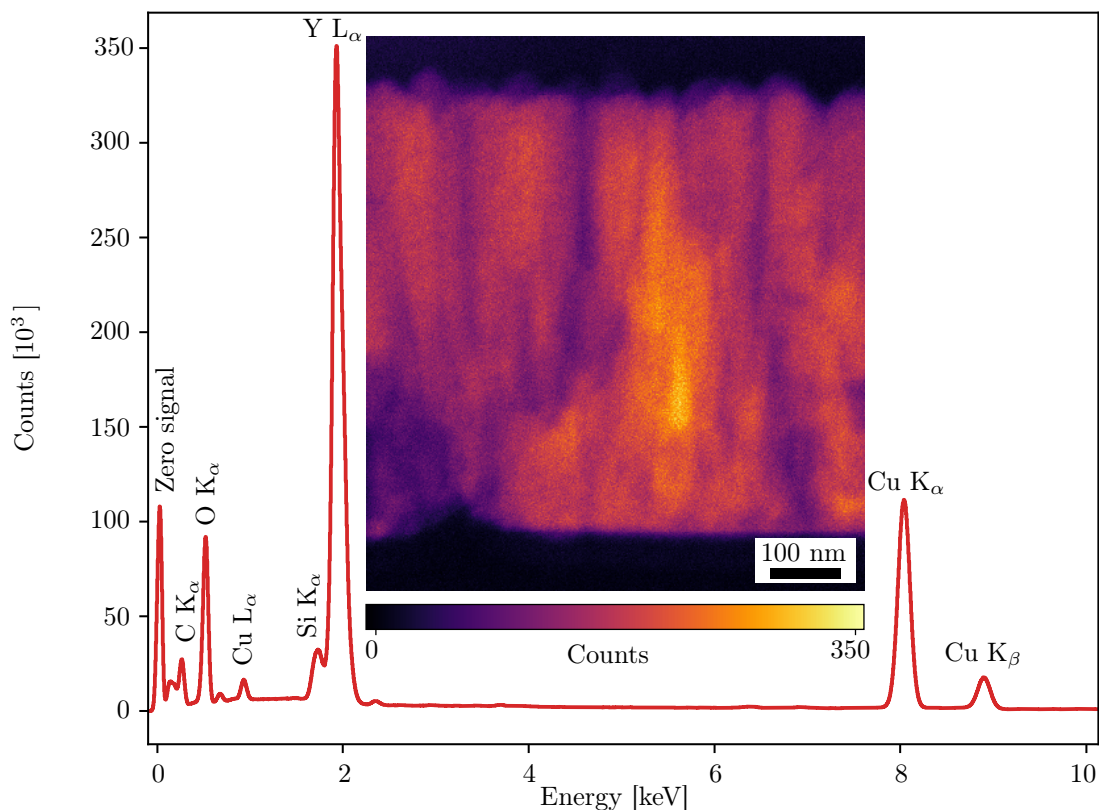


Figure 4.21: EDS spectrum acquired from *AA* with a map of X-ray counts per probe position.

To get a thickness resolved, relative composition of the O and Y signals, the spectra were first summed horizontally in lines to give one spectrum per line. Then followed a Cliff-Lorimer quantification enabled by HyperSpy from k factors as explained in §2.2.3, using theoretical values for the factors given in §3.4.6. The signals from Cu and C were not included in the

quantification. A plot of atomic percent for the peaks of interest O K $_{\alpha}$ and Y L $_{\alpha}$ as a function of distance from film bottom to top was produced, as shown in Fig. 4.22 (a). More material results in more X-rays emitted, so a thickness map, by subtracting a zero-loss EFTEM image from an unfiltered image using energy filtering, was constructed to give an impression of relative thickness parallel to the incident beam direction as t/λ , where λ is the mean free path of the material. Maps of peaks Y L $_{\alpha}$ (b) and O K $_{\alpha}$ (c) and a thickness map (d) of approximately the same region are also shown. Values for t/λ were summed similar to the X-ray peaks, and a plot of t/λ as a function of approximately the same distance as the X-ray peaks are also included in Fig. 4.22 (a). The oxygen signal from the film can be seen to vary in roughly three regions: (i) highest in the film bottom from 0-50 nm, (ii) somewhat lower from 50-250 nm and (iii) slowly declining from 300 nm and towards the top. The yttrium signal on the other hand can be seen to increase from bottom to top, and abruptly going to zero as the oxygen and carbon signal dominates due to the epoxy or grid film. The relative thickness follows a similar trend to the yttrium signal. Both the Y and O element maps show less signal in vertical lines in the growth direction, presumably in column boundaries.

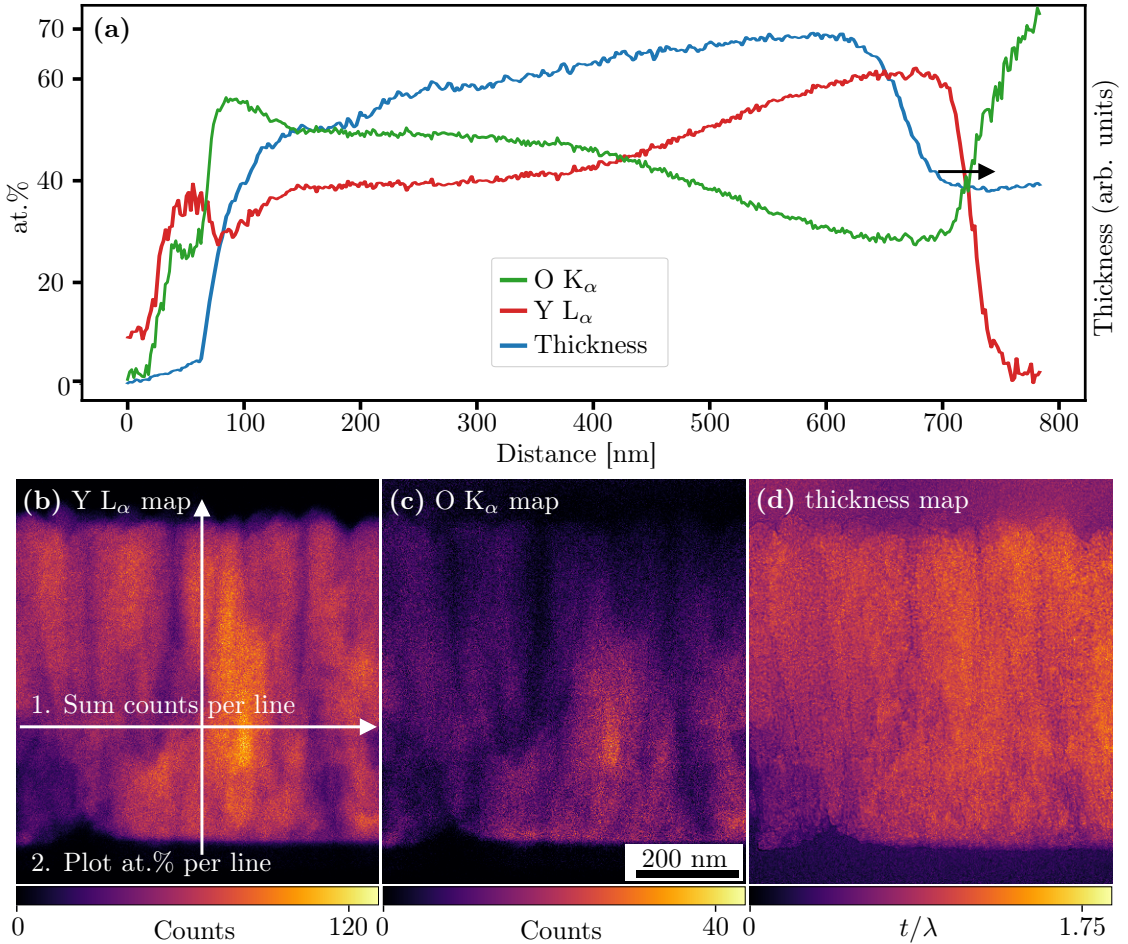


Figure 4.22: At.% as a function of distance from the film bottom to top (a), quantified using the Cliff-Lorimer method with theoretical values for the k factors. Maps of the Y L α (b) and O K α peak signals per probe position show lower signal in column boundaries and/or in thinner regions, while a relative thickness map (d) shows that the specimen thickness varies little in the film.

4.6 Specimen preparation

Almost all results presented here were obtained from specimen *AA* prepared by ultramicrotomy, and none from specimens such as *DD* prepared by tripod polishing. This is because specimens prepared by tripod polishing showed varying thickness in the beam direction and hardly any electron transparent regions compared to those prepared by ultramicrotomy. Fig. 4.23 (a,b) shows two examples of electron transparent regions from *DD*, while (d) shows one of many electron transparent regions available from an ultramicrotomed specimen similar to *AA*. Only a handful of columns can be imaged in the tripod polished specimens, while relatively vast regions can be studied from ultramicrotomy specimens. An example of one of many such regions are highlighted in (c) shown in the middle of an ultramicrotomy section of embedding epoxy, inside a window on the TEM grid. However, the ultramicrotomed specimen in (d) was sectioned with

the cutting direction of the knife perpendicular to the growth direction, leading to break-up of the film in groups of a few columns per group. This break-up, visible in (d), was representative for the films on such specimens. Specimen *AA* was made with the cutting direction parallel to the growth direction. Although break-up was seen on this specimens as well, larger intact regions, like the one studied in this work, were easily found. The wave-like opening in the section of embedding epoxy in (c) came about because of charging of the epoxy, caused by the electron beam. This grid had no carbon film on it, and switching to a film that did substantially decreased the charge build-up.

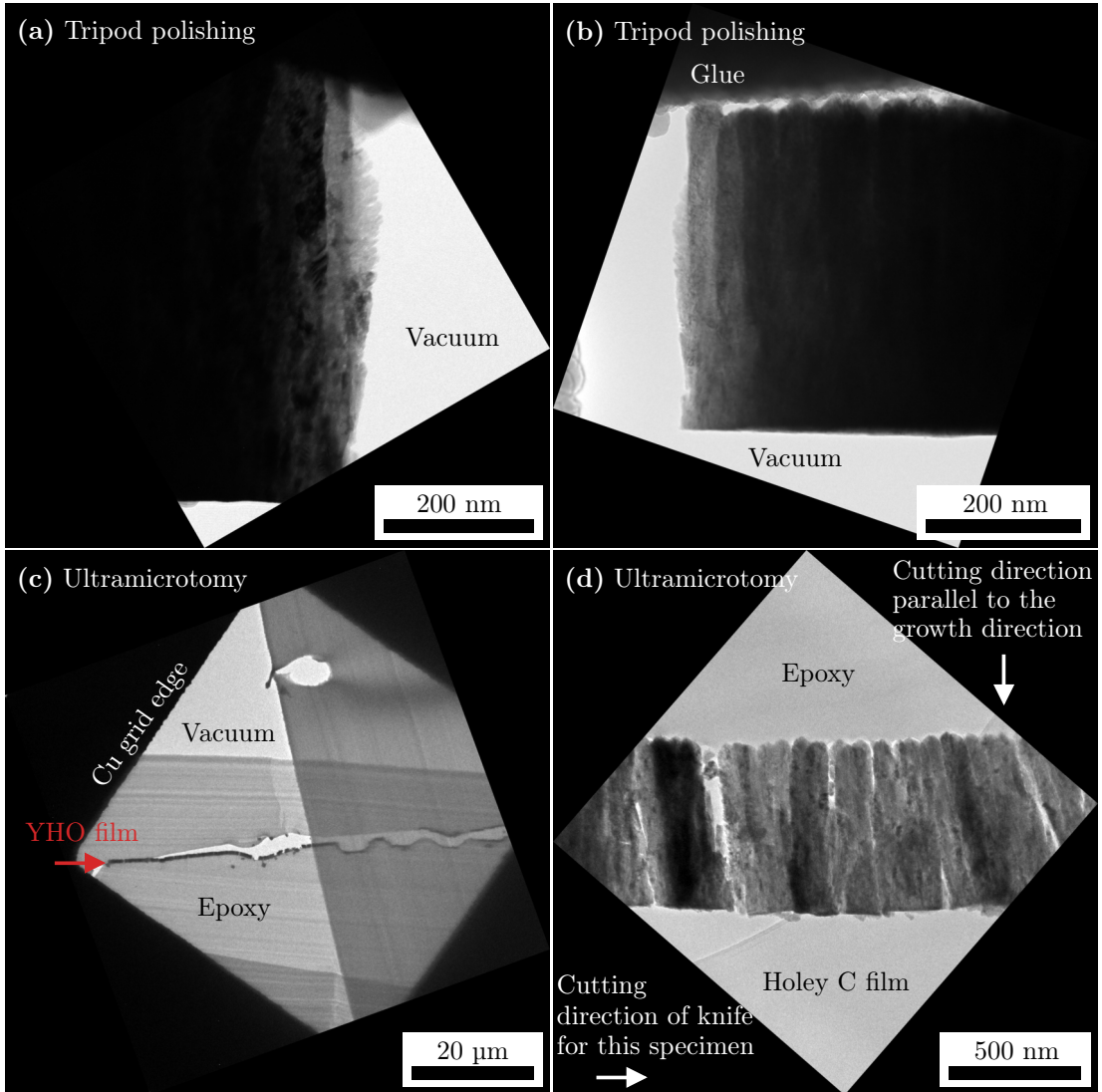


Figure 4.23: Comparison of electron transparent regions from films of tripod polished specimen *DD* (a,b) and two ultramicrotomed specimens (c,d), the latter resulting in much larger regions.

5 | Discussion

The goal of this work was to study the evolution of the microstructure and oxygen concentration with film thickness of sputtering deposited, oxygen-containing yttrium hydride thin films. The observed crystal phases in the films, the average grain size and technical aspects of the quantification of the oxygen and yttrium signals are discussed first. Then, the microstructure is correlated to the oxygen signal along the film thickness. A model is proposed to explain the growth of the microstructure and subsequent diffusion of oxygen into the structure. Since the relatively recent scanning precession electron diffraction technique in combination with automated crystal orientation mapping were used in order to construct this model, aspects of data acquisition and processing are discussed. The problem of assigning *one* crystal orientation to a diffraction pattern with reflections from multiple, overlapping grains is also addressed. Lastly, the optimal way to prepare the YHO films for TEM studies is considered.

5.1 Microstructure and oxygen concentration

Before discussing the variations in the microstructure and O signal, it is of interest to compare detected phases in the films to previous findings by the research group at IFE of photochromic YHO thin films similar to the ones studied here. The structure's grain size and technical aspects of the quantification of the O and Y signals are also commented on. In the proposed growth and reaction model below, the film thickness is divided into three regions with distinct differences in microstructure and O signal. These are termed from substrate to film surface **i** (0-50 nm), **ii** (50-250 nm) and **iii** (250-650 nm) and are discussed before the model is presented.

5.1.1 Crystal phases

The SAD pattern in Fig. 4.6 (b) shows an expanded YH_2 fcc structure with a lattice parameter of $a = 5.39 \pm 0.04 \text{ \AA}$. No relative change in the lattice parameter was observed with thickness, from comparing distances between peak positions and the direct beam in six SAD patterns acquired at different thicknesses of the film. The patterns are not included here because no calibration pattern, like the Au patterns used to determine the lattice parameter in Fig. 4.6 (a), was acquired in the same session. This matches recent reports by Montero *et. al*²⁰ of a lattice parameter of $a = 5.4 \text{ \AA}$ for photochromic oxygen-containing yttrium hydride from grazing incidence XRD experiments. The expanded YH_2 lattice was explained by an increased oxygen content, possibly because of a higher surface area in the structure due to deposition at a higher partial hydrogen/argon than compared to metallic yttrium hydride. However, no other phases

were detected. The three unidentified peaks in Fig. 4.6 and Tab. 4.1, was systematically seen in all SAD patterns recorded from the films. The innermost peak at $d = 4.44 \text{ \AA}$ was the strongest among the three on average. The peaks must belong to one or more crystalline phases in the film not reported in previous studies. The fact that the ratio of the first and second d spacing matches the ratio of the principal spot spacings $\{111\}$ and $\{311\}$ of the fcc structure might indicate that at least those two peaks come from such a structure. Mongstad *et. al*⁷⁵ discussed briefly the presence of Y_2O_3 in its amorphous state as an explanation for where the oxygen resides in the structure. However, the optical behaviour of Y_2O_3 is very different from what they observed, hence they concluded that the transparent yttrium hydride is responsible for the observed optical properties. No crystalline Y_2O_3 has previously been reported in previous XRD studies, and none was observed in this work either. However, experiments with a greater angular resolution and less background noise in the signal, like synchrotron radiation XRD, could determine the origins of these unidentified peaks. The location of the oxygen in the fcc cell is still unknown, although a partial filling of the tetrahedral position $(\frac{3}{4}, \frac{3}{4}, \frac{3}{4})$ has been suggested by Pishtshev *et. al.*⁵⁶

5.1.2 Grain size and misorientations

It is obvious from considering DF TEM and VDF images and loading maps from the SPED dataset that each column consist of multiple grains. This is perhaps best seen in the VDF image in Fig. 4.9 (b) and loading map #28 in Fig. 4.12 (b), where a defined column structure in the middle (which looks to be the same column) clearly shows varying intensities inside it. The reconstruction of grains from the orientation data from the SPED dataset also results in multiple grains within column structures with similar orientations. The lower misorientations within a column compared to misorientations across column boundaries, shown in Fig. 4.20, also supports the conclusion that each column consist of multiple grains with similar orientations. Some larger parts of column structures are reconstructed as single grains further up in the film thickness, but apart from that no clear trend in the grain size with thickness can be interpreted from the grain reconstruction in Fig. 4.17 (a). The grain size of $(14.8 \pm 1.6) \text{ nm}$ has no comparison in the literature, but inspections of lone, intense features beside the column structures in the VDF images and the loading maps from the SPED dataset presented here supports the calculated grain size. A scanning step in the SPED dataset of 2.4 nm means that a grain's projected area of $\sim \pi(15/2)^2 = 176 \text{ nm}^2$ gives around 30 diffraction patterns, which is considered sufficient to determine a grain's orientation. The feature sizes observed in the HRTEM image in Fig. 4.5 also support the calculated grain size. No previous attempt has been made to determine the grain structure, however You *et. al*²¹ reported on the column sizes of four photochromic YHO films of thicknesses ranging from 490 to 790 nm. From AFM studies on the film surfaces they determined the column tops to be around 100-200 nm for all films. This is somewhat larger than the $\sim 75 \text{ nm}$ column tops observed in the SE images in Fig. 4.1, however their films were deposited on substrates of glass and not GaAs as the films studied here, which might explain the discrepancy.

The distribution of misorientation angles between grains in Fig. 4.19 (a) shows that most grains are oriented at relatively low angles of up to 20° to each other, with a clear majority in the 10° - 20° range. The grain boundary misorientation map in Fig. 4.18 (a) shows many grain boundaries of misorientations $< 20^\circ$ within what seems to be columns. This result is consistent with the interpretation that a column consists of multiple grains of similar orientations.

5.1.3 Oxygen and yttrium EDS signals

Although the uncertainty in thickness determination from energy filtering in general is of the order of 20-30%,³² the observed trend of a weak, constant increase in specimen thickness along the film thickness in the profile in Fig. 4.22 (a) seems to be of a physical nature. Preferential absorption of characteristic X-rays with energies $< 1\text{-}2$ keV, including the O K_α peak at 0.52 keV, means that the detected X-ray counts are lower than the generated counts. Absorption is not a problem for the characteristic Y L_α X-rays. The detected O signal decreases with thickness in a non-linear fashion. Since the thickness increases in a close to linear fashion, the observed variation in the O signal cannot be due to absorption alone. The simple Cliff-Lorimer quantification to obtain at.% for O K_α and Y L_α only, without correcting for absorption or fluorescence, excludes interpretation of the EDS signals beyond their clear trends suggested in the growth and reaction model. If such an interpretation is of interest, e.g. to compare O signals for differently prepared YHO thin films, the ζ -factor method discussed in §2.2.3 should be pursued.

In summarising the last three paragraphs, the microstructure can be said to consist mostly of an expanded, oxygen-rich fcc YH_2 structure with a 5.39 Å lattice parameter and 15 nm grains. The oxygen signal varies with the film thickness, while no variation in the crystal structure except for texture is observed. A discussion of the microstructure and oxygen signal along three distinctly different regions of the film follows.

5.1.4 Region i: bottom

Although specimen *AA* was initially deposited on an Si substrate with its [001] planes parallel to the substrate surface, most sputtered atoms seem to have nucleated during growth into grains with a weak, closest packed [111] texture parallel to the substrate surface, i.e. in the growth direction. This is best seen from the **y** orientation map in Fig. 4.14, where diffraction patterns from this region have systematically been matched to simulated patterns from crystal orientations near [111]. No patterns from grains closest to the substrate are matched to [001], while some are matched to [011].

The misorientation line from measurements along the film bottom in Fig. 4.20 (h,i,j) shows rapid changes in orientation of up to 60° in 5-10 nm intervals. This supports the explanation of a finer structure with smaller groups of grains with similar orientations than higher up in the film where grains are grouped into larger structures. Misorientations to mean orientation of measurements within all reconstructed grains (including those with a low reliability) are also seen to be highest in the first 200-300 nm of the film from Fig. 4.18 (b). Although this can be attributed to the low reliability of orientation matching in this region, seen in the reliability map in Fig. 4.13 (b), the reason for the low reliability can still provide useful information on the microstructure. When considering that a diffraction pattern with reflections from multiple, overlapping grains is difficult to match to one specific orientation, a reasonable explanation for the low reliability in the film bottom is that it consists of multiple, smaller, more randomly oriented grains than higher up in the film structure. That the film bottom looks to be as thick as the rest of the film, evident from the thickness map in Fig. 4.22 (d), discards the explanation that more grains are illuminated by the probe because the film bottom is thicker.

The bottom features in the DF TEM image in Fig. 4.9 (a) and loading map #28 in Fig. 4.12

(b) also support the assumption of a finer structure in the film bottom compared to the rest of the film. Loading map #24 in Fig. 4.11 (b) shows some larger structures starting to grow from the bottom, however few seem to directly continue to grow into columns. The BF and DF TEM images and the SAD pattern from plan-view specimen *BB* in Fig. 4.2 may show how the first 50 nm of specimen *AA* would look in a plan-view sectioned specimen. The images show no column structures, and the [111] ring in the inset DP has the highest intensity, i.e. specimen *BB* shows a [111] texture in the growth direction. The (200) DF TEM image in Fig. 4.3 (b), coloured green, shows that the bottom structure has a strong (200) reflection into the paper plane, also evident when considering the *z* orientation map. Both Mongstad *et. al*⁷⁵ and You *et. al*²¹ reported on a [001] texture for transparent films and a [111] texture for opaque films from XRD experiments, the latter films prepared at lower hydrogen pressures. Based on previous findings of the correlation between an increase in the film's band gap and with oxygen content, this suggests that a film with a [111] texture absorbs less oxygen than one with a [001] texture. However, the plot of atomic ratio at.% as a function of film thickness in Fig. 4.22 (a) shows highest O signal in the film bottom, where a weak [111] texture is observed. Based on the finer structure in the bottom, a reasonable suggestion is that the surface area is larger in the bottom than higher up. It has been suggested by Moldarev *et. al*²² that the finer structure observed in the film might result in faster oxidation, a suggestion that fits the obtained results. But, further TEM studies of films prepared at different hydrogen pressures are needed to learn how the oxygen signal varies along the thickness of these films before a general picture can be drawn.

5.1.5 Region ii: lower middle

No clear texture in the growth direction is observed in the region from 50 nm to approximately 250 nm, as seen from the orientation maps in Fig. 2.17. The summed DF TEM images in Fig. 4.3 (b) show little intensity in this region, however VDF image (b) in Fig. 4.8 and loading map #24 in Fig. 4.12 (b) show that grains have grouped into larger structures extending in the growth direction. Some column growth seem to start in this region. The transition from a weak [111] texture in region **i** to a [001] texture in region **iii**, and the start of growth of larger structures, is believed to result from competitive growth⁷⁶ of grains. Growth conditions close to the substrate do not dominate, and the growth is instead determined by the orientation of the already present grains. The competition starts among the neighbouring grains, and the faster growing grains grow over slowly growing grains into V-shaped columns. It is terminated when only column structures exhibiting the same type of grain faces proceed to the surface. The larger structures are suggested to result in less surface area, and hence less of the structure can oxidise. This suggestion is reflected in the weak decline of the O signal and then an extended region of about 200 nm of constant O signal.

5.1.6 Region iii: top half

As suggested by all images and orientation mappings presented in the results, the growth of denser column structures with a strong [001] texture in the growth direction starts to dominate from approximately 250 nm and up. The intercolumnar boundaries imaged in the BF and ADF STEM images in Fig. 4.4 (c,d) seem to grow denser and fill the voids between the columns from 200-300 nm and up, indicating that the column tops in general, as also observed in SEM, grow and expand to fill these voids as the film thickness increases. The width of the column

tops in the orientation maps agrees with the one observed in the SE images. As the columns grow larger, the structure becomes more dense and the surface area decreases. This can explain the steady decline in the O signal from 250 nm and up. Previous findings^{21,75} have shown that photochromic, YHO thin films have a [001] texture. That this texture is only observed here in conjunction with the column growth suggests that the growth is important for the photochromic behaviour. However, the O signal is declining in this region and is highest in the bottom region. It might be that the combination of these two regions in the microstructure is of importance considering the films' photochromic behaviour.

The intracolumnar voids and 'dendritic-like' features highlighted in the BF and ADF STEM images in Fig. 4.4 show different features of the columns. The voids seem to part a column into narrower fibres that extend to the column top. The zoomed in view of a column top in the inset SE image in Fig. 4.2 (c) looks similar to these fibres. No conclusions as to what causes these voids and fibres to form can be drawn from the results presented here. The pink and white arrows in HRTEM image in Fig. 4.5 points to similar voids as those seen in the STEM images.

5.1.7 Thin film growth and reaction model

All SE images, BF, DF and VDF TEM images, BF and ADF STEM images and the EDS map show that the microstructure and oxygen concentration is inhomogeneous along the film thickness. The microstructure resembles the *zone T* in the structure zone model for sputtering deposited thin films, explained in §2.7. Barna and Adamik⁷⁶ summarises that a structure in this zone '... is fine crystalline at the substrate, composed of V-shaped grains in the next thickness range while can be columnar in the upper part of thick films.' Fig. 5.1 shows the proposed model for sputtering deposited, YHO thin film growth and subsequent diffusion of oxygen into the structure, based on the previous discussion.

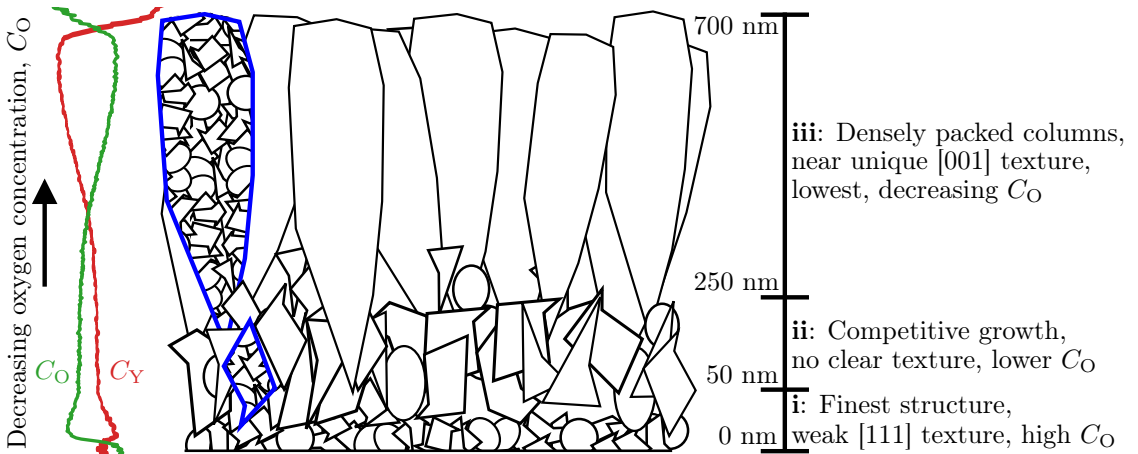


Figure 5.1: Growth and reaction model for sputtering deposited YHO thin films. All larger structures are polycrystalline, emphasised by the blue bordered structures. The at.% of O and Y are also shown. The at.% and film thickness bar are not on scale.

The overall features of the different regions of the microstructure can be summarised as follows,

which is also done in the figure:

- i 0-50 nm. Finest grouping of grains of similar orientations into structures, with a weak [111] texture in the growth direction, large surface area and a high oxygen signal.
- ii 50-250 nm. Competitive growth of larger structures with no clear texture, smaller surface area and a lower oxygen signal.
- iii 250-650 nm. Tightly packed, larger column structure with a near unique [001] texture, a decline in surface area and a decreasing oxygen signal.

5.2 Methods

5.2.1 Problem of overlapping grains

The need to deconvolve the detected signals produced by an electron beam penetrating different grains or materials is a challenge for TEM imaging and spectroscopy in general. This is most certainly also the case for the ACOM-TEM technique, when only one orientation is given to a PED pattern that always shows reflections from multiple grains. This problem is illustrated in Fig. 5.2, where an electron beam is scanning towards the right over two grains overlapping in the beam path, resulting in patterns showing reflections from both grains.

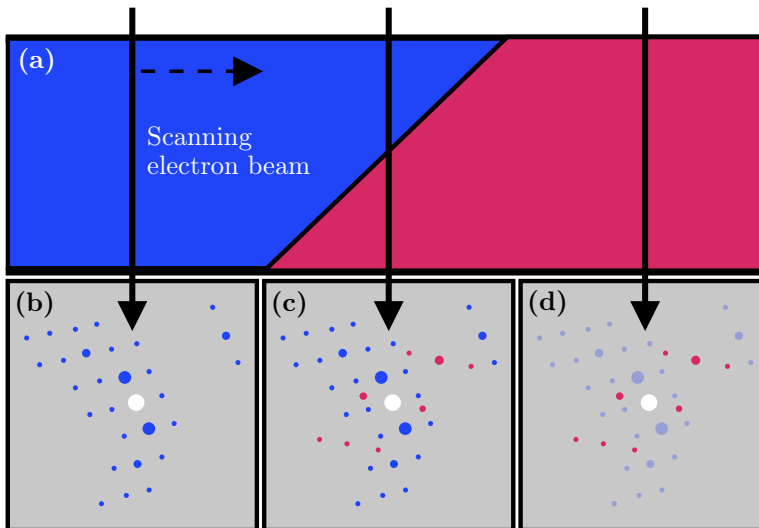


Figure 5.2: Overlapping grains (a) lead to PED patterns of reflections from more than one grain (c,d). The beam travels towards the right, and a remaining, weakened signal from the left (blue) grain is detected in (d) even when the overlap is surpassed.

If specimen AA is 100 nm thick, at least seven grains of 15 nm diameter was illuminated by the electron beam to create the PED patterns at each beam position. The correlation index density maps in IPFs in Fig. 4.13 (c,d), as well as the corresponding PED patterns, are clear examples of the overlap problem. In the case of (c), two candidate orientations corresponding

to $\sim [101]$ and $\sim [112]$ can be made out in the IPF. The $[101]$ orientation is given highest index score, although the simulated pattern does not intuitively match the clearest reflections in the PED pattern. Multiple approaches to improve the template matching can be considered. The simplest solution would be to create a thinner specimen so fewer grains are illuminated. Another solution could be to re-index patterns after subtraction of the reflections in the previous best matching simulated pattern. This approach would however be problematic if reflections from multiple grains directly overlap in the image pixels. A third approach could be to reduce the background by thresholding pixel values to enhance the contrast or by decomposing the dataset and exclude the components considered as noise. This last approach was attempted in template matching the SPED dataset from specimen *AA*. However, more ‘noisy’ patterns like those in vacuum were now assigned reflections from the more dominant components, hence leading to an increase in template matching scores for these patterns. This made it more difficult to filter out unreliable measurements. It might have been avoided had it been easier to distinguish signal from noise in Scree plot the PCA decomposition in Fig. 4.10. A last proposed improvement is to match the two-three highest scoring simulated patterns of one PED pattern to the surrounding patterns to decide which is most reliable. This might however lead to a lower spatial resolution due to an averaging of orientations.

5.2.2 Data acquisition and processing

The number of component patterns returned from an NMF decomposition is limited ideally to the number of orientations or phases in the volume studied. To prove that this is indeed the case for a material system of known orientations and phases, a SPED dataset was acquired from an epitaxially grown GaAs nanowire. It consists of two zinc-blend crystal structures and one wurtzite crystal structure, and the results of both VDF imaging, a PCA Scree plot and an NMF decomposition are included in the appendices §D. When comparing the Scree plots from the PCA decompositions of the datasets from specimen *AA* in Fig. 4.10 and the GaAs nanowire, it becomes clear that the former dataset is described by many more components than the latter. This is an effect of the many more crystal orientations present and also the overlapping grains.

Another inherent problem with the acquisition of the PED patterns is the slow ‘reset’ of the fluorescent viewing screen, i.e. the afterglow, illustrated in the pattern in Fig. 5.2 (d) as a remaining, weakened signal from the left (blue) grain. The effects of afterglow are seen in the VDF images in Fig. 4.9 and the index and reliability maps in Fig. 4.13. The problem of afterglow can be reduced by increasing the acquisition exposure time to give the viewing screen time to reset and the present illuminated grain time to dominate the screen. However, more diffuse scattering would be acquired simultaneously and the recorded patterns would be saturated, meaning fainter reflections could be lost. This would degrade both the angular resolution, worsening the template matching, and the spatial resolution, worsening feature edges in VDF images.

Although a specimen thickness > 75 nm allows for more than one column to be imaged in the TEM, the three-dimensional structure of the film is lost unless tomography experiments are conducted. The 3D reconstruction a TiN thin film prepared by magnetron sputtering was recently reported by Meng and Zuo.⁷⁷ The film has a similar column structure to the YHO film with column sizes of 50-100 nm. A diffraction pattern acquisition technique similar to SPED where the beam was not precessed, termed scanning electron nanodiffraction or SEND,

was used. Both the columns and their boundaries were reconstructed in 3D in addition to their orientation. Although the misorientation lines in Fig. 4.20 provide some insight into the orientation relationships between columns in the YHO thin film, performing SEND or SPED in combination with tomography⁵⁵ might produce clearer answers to these relationships.

5.2.3 Specimen preparation

A tripod polishing scheme is included in the appendices §B. The technique is cumbersome and time consuming with many periods of waiting for glue to cure. A close to extreme care is needed throughout the polishing procedure and the most critical steps are towards the end of the polishing when the specimen is at its thinnest. The fact that the YHO thin films delaminated from their Si and GaAs substrates enabled ultramicrotomy sectioning. As long as the specimen is conveniently oriented inside the embedding epoxy stub, a countless number of sections can be cut from the stub. These sections showed vast regions of electron transparent thin film, as shown in Fig. 4.23. The thin films break easily along the column boundaries under sectioning. However, by sectioning with the cutting direction parallel to the growth direction rather than perpendicular to it reduced this break-up was minimised. Ultramicrotomy is therefore recommended over tripod polishing for TEM specimen preparation of sputtering deposited YHO thin films on Si and GaAs substrates. A series of TEM specimens of films sputtering deposited at different process parameters could easily be prepared in a work week. This enables studies of the variation of microstructure and oxygen concentration with process parameters like the deposition pressure and substrate temperature.

6 | Conclusions

The column growth morphology, crystal structure, thin film texture, grain size and elemental composition of photochromic, oxygen-containing yttrium hydride thin films were studied in the SEM and for the first time in the TEM. A model for the thin film growth and subsequent reaction of oxygen in the microstructure has been created, based on the results from studies of two 650 nm thick films and one 100 nm thick film prepared by reactive magnetron sputtering deposition. Conclusions from the thin film studies are:

- ▶ The films have an expanded YH_2 fcc structure with a lattice parameter of $a = (5.39 \pm 0.04)$ Å, matching previous findings by XRD.^{18,24}
- ▶ Selected-area diffraction patterns from all films showed three unidentified peaks as evidence of other crystalline phases present in the films, not reported in previous studies. The peak position ratio of two of the peaks indicated an fcc structure.
- ▶ The microstructure of the films is dominated by a column growth structure, resembling *zone T* in the structure zone model for sputtering deposited thin films.
- ▶ The columns consist of multiple grains with an average size of (14.8 ± 1.6) nm. Grains within a column have similar orientations.
- ▶ The growth and reaction model divided the 650 nm thick film into three regions along the film thickness, based on variations in microstructure and oxygen signal:
 - i 0-50 nm. Finest grouping of grains of similar orientations into structures, with a weak [111] texture in the growth direction, large surface area and a high oxygen signal.
 - ii 50-250 nm. Competitive growth of larger structures with no clear texture, smaller surface area and a lower oxygen signal.
 - iii 250-650 nm. Tightly packed, larger column structure with a near unique [001] texture, a decline in surface area and a decreasing oxygen signal.

Thin film specimens have been prepared for TEM studies using ultramicrotomy and tripod polishing. Conclusions from the specimen preparation are:

- ▶ Films deposited on Si and GaAs substrates delaminated from their substrates.

- ▶ Ultramicrotomy produced specimens with vast, electron transparent regions, whereas only a handful of columns could be imaged in the tripod polishing specimens. Ultramicrotomy is therefore the recommended preparation procedure of delaminating YHO thin films.

7 | Further work

The ultramicrotomy scheme for preparing sputtering deposited, YHO thin films used in this work produces TEM specimens of a high quality, with no clear preparation artefacts, in a short time. The determination of grain size, texture and oxygen concentration along the film thickness can be done by acquiring one SPED map and one EDS map. This enables systematic studies of these features as a function of process parameters like the partial hydrogen/argon pressure, substrate and substrate temperature. This should be done in order to understand how variations in the oxygen concentration are connected to variations within the microstructure.

If to interpret more than just the trend in oxygen concentration along the film thickness is desired, an improvement to the Cliff-Lorimer quantification used in this work should be pursued. To perform an accurate quantification of the oxygen and yttrium signals along the film thickness, experimental k factors should be determined using standard specimens. Another approach to improve the accuracy could be to use the ζ -method.

In order to improve the determination of grain size and texture, it is obvious that to deconvolve mixed PED patterns from overlapping grains is of importance. One of the most promising approaches discussed in this work is to reduce the background noise by decomposing the SPED dataset and discard the background from the dataset. A recent open source Python library called PyCrystEM (Python Crystallographic Electron Microscopy), developed by a team of PhD students including Duncan Johnstone at the University of Cambridge, aims at facilitating among other things such noise reduction through decomposition of datasets. As the time of writing, the library is not available to the general public, although it will be available in the near future. A goal is to improve the template matching routines used in the commercial NanoMegas ASTAR software of SPED datasets through open collaboration and utilisation of existing, well established Python libraries, similar to what is done in HyperSpy. Use of the SPED technique is continuously increasing, and contributions to this package could benefit many.

As discussed, 3D reconstruction of the YHO film's column structure via SEND or SPED in combination with tomography can provide insight into orientation relationships between columns. Although the series study proposed above probably would produce results answering questions regarding the microstructure and oxygen concentration more so than a 3D reconstruction, the novelty of a reconstruction of this column structure should not be underestimated.

References

- ¹ INTERNATIONAL ENERGY AGENCY. World Energy Outlook 2015 Factsheet. https://iea.org/media/news/2015/press/151110_WEO_Factsheet_GlobalEnergyTrends.pdf.
- ² PETERS, GP, ANDREW, RM, BODEN, T, CANADELL, JG, CIAIS, P, LE QUÉRÉ, C, MARLAND, G, RAUPACH, MR and WILSON, C. The challenge to keep global warming below 2 C°. *Nature Climate Change*, **3**(1):4–6, 2013.
- ³ UNITED NATIONS. Adoption of the Paris Agreement. <http://unfccc.int/resource/docs/2015/cop21/eng/l09r01.pdf>.
- ⁴ POPULATION REFERENCE BUREAU. 2016 World Population Data Sheet. <http://prb.org/pdf16/prb-wpds2016-web-2016.pdf>.
- ⁵ PÉREZ-LOMBARD, L, ORTIZ, J and POUT, C. A review on buildings energy consumption information. *Energy and buildings*, **40**(3):394–398, 2008.
- ⁶ COX, S. *Losing Our Cool: Uncomfortable Truths About Our Air-Conditioned World (and Finding New Ways to Get Through the Summer)*. The New Press, 2013.
- ⁷ BOEING. AERO Magazine QTR 4.06. 04 Boeing 787 From the ground up. http://boeing.com/commercial/aeromagazine/articles/qtr_4_06/AERO_Q406.pdf.
- ⁸ BROWN, GH. *Photochromism*, vol. 3. Wiley-Interscience, 1971.
- ⁹ EXELBY, R and GRINTER, R. Phototropy (or photochromism). *Chemical Reviews*, **65**(2):247–260, 1965.
- ¹⁰ NAKATANI, K, PIARD, J, YU, P and MÉTIVIER, R. Introduction: Organic photochromic molecules. *Photochromic Materials: Preparation, Properties and Applications*, pp. 1–45, 2016.
- ¹¹ GRANQVIST, CG. Solar energy materials. *Applied Physics A*, **52**(2):83–93, 1991.
- ¹² GRANQVIST, CG. Transparent conductors as solar energy materials: A panoramic review. *Solar energy materials and solar cells*, **91**(17):1529–1598, 2007.
- ¹³ KANU, SS and BINIONS, R. Thin films for solar control applications. In *Proceedings of the Royal Society of London A: Mathematical, Physical and Engineering Sciences*, p. rspa20090259. The Royal Society, 2009.
- ¹⁴ OHKO, Y, TATSUMA, T, FUJII, T, NAOI, K, NIWA, C, KUBOTA, Y and FUJISHIMA, A. Multicolour photochromism of TiO₂ films loaded with silver nanoparticles. *Nature Materials*, **2**(1):29–31, 2003.
- ¹⁵ CHEN, Z, GAO, Y, KANG, L, DU, J, ZHANG, Z, LUO, H, MIAO, H and TAN, G. VO₂-based double-layered films for smart windows: optical design, all-solution preparation and improved properties. *Solar Energy Materials and Solar Cells*, **95**(9):2677–2684, 2011.
- ¹⁶ OHMURA, A, MACHIDA, A, WATANUKI, T, AOKI, K, NAKANO, S and TAKEMURA, K. Photochromism in yttrium hydride. *Applied Physics Letters*, **91**(15):151904, 2007.

- ¹⁷ HUIBERTS, JN, RECTOR, JH, WIJNGAARDEN, RJ, JETTEN, S, DE GROOT, D, DAM, B, KOEMAN, NJ, GRIESSEN, R, HJÖRVARSSON, B and OLAFSSON, S. Synthesis of yttriumtrihydride films for ex-situ measurements. *Journal of Alloys and Compounds*, **239**(2):158–171, 1996.
- ¹⁸ MONGSTAD, TT, PLATZER-BJÖRKMAN, C, MAEHLLEN, JP, MOOIJ, LPA, PIVAK, Y, DAM, B, MARSTEIN, ES, HAUBACK, BC and KARAZHANOV, SZ. A new thin film photochromic material: Oxygen-containing yttrium hydride. *Solar Energy Materials and Solar Cells*, **95**(12):3596–3599, 2011.
- ¹⁹ EMSLEY, J. *Nature's building blocks: an AZ guide to the elements*. Oxford University Press, 2011.
- ²⁰ MONTERO, J, MARTINSEN, FA, LELIS, M, KARAZHANOV, SZ, HAUBACK, BC and MARSTEIN, ES. Preparation of yttrium hydride-based photochromic films by reactive magnetron sputtering. *Solar Energy Materials and Solar Cells*, 2017.
- ²¹ YOU, CC, MONGSTAD, TT, MAEHLLEN, JP and KARAZHANOV, SZ. Dynamic reactive sputtering of photochromic yttrium hydride thin films. *Solar Energy Materials and Solar Cells*, **143**:623–626, 2015.
- ²² MOLDAREV, D, PRIMETZHOFFER, D, YOU, CC, KARAZHANOV, SZ, MONTERO, J, MARTINSEN, F, MONGSTAD, T, MARSTEIN, ES and WOLFF, M. Composition of photochromic oxygen-containing yttrium hydride films. *Solar Energy Materials and Solar Cells*, 2017.
- ²³ YOU, CC, MONGSTAD, TT, MAEHLLEN, JP and KARAZHANOV, SZ. Engineering of the band gap and optical properties of thin films of yttrium hydride. *Applied Physics Letters*, **105**(3):31910, 2014.
- ²⁴ MONTERO, J, MARTINSEN, FA, GARCÍA-TECEDOR, M, KARAZHANOV, SZ, MAESTRE, D, HAUBACK, B and MARSTEIN, ES. Photochromic mechanism in oxygen-containing yttrium hydride thin films: An optical perspective. *Physical Review B*, **95**(20):201301, 2017.
- ²⁵ MAEHLLEN, JP, MONGSTAD, TT, YOU, CC and KARAZHANOV, SZ. Lattice contraction in photochromic yttrium hydride. *Journal of Alloys and Compounds*, **580**:S119—S121, 2013.
- ²⁶ ÅNES, HW. *Transmission Electron Microscopy Characterization of Hydride-based Smart Windows*. Project's thesis, 2016. Norwegian University of Science and Technology.
- ²⁷ KITTEL, C. *Introduction to Solid State Physics*. John Wiley & Sons, 8th ed., 2005.
- ²⁸ ALS-NIELSEN, J and McMORROW, D. *Elements of modern X-ray physics*. John Wiley & Sons, 2011.
- ²⁹ HAMMOND, C. *The basics of crystallography and diffraction*, vol. 12. Oxford University Press, 2009.
- ³⁰ VAJDA, P. *Handbook on the Physics and Chemistry of Rare Earths*, vol. 20. Test, 1995.
- ³¹ SAMUELSEN, EJ. *Materials physics: Structure, Diffraction, Imaging and Spectroscopy*. NTNU-trykk, 2nd ed., 2006.
- ³² WILLIAMS, DB and CARTER, CB. *Transmission Electron Microscopy: A Textbook for Materials Science*. Springer Science & Business Media, 2009.
- ³³ HUMPHREYS, CJ. The scattering of fast electrons by crystals. *Reports on Progress in Physics*, **42**(11):1825, 1979.
- ³⁴ COWLEY, JM. Applications of electron nanodiffraction. *Micron*, **35**(5):345–360, 2004.
- ³⁵ PENNYCOOK, SJ and NELLIST, PD. *Scanning Transmission Electron Microscopy*. Springer New York, 2011. doi:<http://dx.doi.org/10.1007/978-1-4419-7200-2>.
- ³⁶ VINCENT, R and MIDGLEY, PA. Double conical beam-rocking system for measurement of integrated electron diffraction intensities. *Ultramicroscopy*, **53**(3):271–282, 1994. doi:[https://doi.org/10.1016/0304-3991\(94\)90039-6](https://doi.org/10.1016/0304-3991(94)90039-6).
- ³⁷ MIDGLEY, PA and EGGEMAN, AS. Precession electron diffraction—a topical review. *IUCrJ*, **2**(1):126–136, 2015.

- ³⁸ RAUCH, EF, VÉRON, M, PORTILLO, J, BULTREYS, D, MANIETTE, Y and NICOLOPOULOS, S. Automatic crystal orientation and phase mapping in TEM by precession diffraction. *Microscopy and Analysis-UK*, **128**:S5–S8, 2008.
- ³⁹ SINGH, G, VAN HELVOORT, AT, BANDYOPADHYAY, S, VOLDEN, S, ANDREASSEN, JP and GLOMM, WR. Synthesis of Au nanowires with controlled morphological and structural characteristics. *Applied Surface Science*, **311**:780–788, 2014.
- ⁴⁰ VENABLES, JA and HARLAND, CJ. Electron back-scattering patterns—a new technique for obtaining crystallographic information in the scanning electron microscope. *Philosophical Magazine*, **27**(5):1193–1200, 1973.
- ⁴¹ BARNARD, JS, JOHNSTONE, DN and MIDGLEY, PA. High-resolution scanning precession electron diffraction: alignment and spatial resolution. *Ultramicroscopy*, 2016.
- ⁴² CLIFF, G and LORIMER, GW. The quantitative analysis of thin specimens. *Journal of Microscopy*, **103**(2):203–207, 1975.
- ⁴³ WATANABE, M and WILLIAMS, D. The quantitative analysis of thin specimens: a review of progress from the Cliff-Lorimer to the new ζ -factor methods. *Journal of Microscopy*, **221**(2):89–109, 2006.
- ⁴⁴ GOLDSTEIN, J, NEWBURY, DE, ECHLIN, P, JOY, DC, ROMIG JR, AD, LYMAN, CE, FIORI, C and LIFSHIN, E. *Scanning electron microscopy and X-ray microanalysis: a text for biologists, materials scientists, and geologists*. Springer Science & Business Media, 2012.
- ⁴⁵ ENGLER, O and RANDLE, V. *Introduction to texture analysis: macrotexture, microtexture, and orientation mapping*. CRC press, 2009.
- ⁴⁶ BUNGE, HJ. *Texture analysis in Materials Science*. Butterworths & Co; Akademie-Verlag Berlin, 1982.
- ⁴⁷ SIMONS, H, KING, A, LUDWIG, W, DETLEFS, C, PANTLEON, W, SCHMIDT, S, STÖHR, F, SNI-GIREVA, I, SNIGIREV, A and POULSEN, HF. Dark-field X-ray microscopy for multiscale structural characterization. *Nature communications*, **6**, 2015.
- ⁴⁸ ICE, GE and PANG, JW. Tutorial on X-ray microLaue diffraction. *Materials Characterization*, **60**(11):1191–1201, 2009.
- ⁴⁹ BACHMANN, F, HIELSCHER, R and SCHAEUBEN, H. Texture analysis with MTEX—free and open source software toolbox. vol. 160, pp. 63–68. Trans Tech Publ, 2010.
- ⁵⁰ MCMAHON, C, SOE, B, LOEB, A, VEMULKAR, A, FERRY, M and BASSMAN, L. Boundary identification in EBSD data with a generalization of fast multiscale clustering. *Ultramicroscopy*, **133**:16–25, 2013.
- ⁵¹ FRANK, FC. Orientation mapping. *Metallurgical Transactions A*, **19**(3):403–408, 1988.
- ⁵² MORAWIEC, A. *Orientations and Rotations. Computations in Crystallographic Textures*. Berlin, Heidelberg, New York: Springer-Verlag, 2004.
- ⁵³ SHLENS, J. A tutorial on principal component analysis. *arXiv preprint arXiv:1404.1100*, 2014.
- ⁵⁴ LEE, DD and SEUNG, HS. Learning the parts of objects by non-negative matrix factorization. *Nature*, **401**(6755):788–791, 1999.
- ⁵⁵ EGGEMAN, AS, KRAKOW, R and MIDGLEY, PA. Scanning precession electron tomography for three-dimensional nanoscale orientation imaging and crystallographic analysis. *Nature communications*, **6**, 2015.
- ⁵⁶ PISHTSHEV, A and KARAZHANOV, SZ. Role of oxygen in materials properties of yttrium trihydride. *Solid State Communications*, **194**:39–42, 2014.
- ⁵⁷ WASA, K and HAYAKAWA, S. *Handbook of sputter deposition technology*. Materials Science and Process Technology Series. William Andrew, 1st ed., 1993.

- ⁵⁸ MATTOX, DM. *Handbook of physical vapor deposition (PVD) processing*. William Andrew, 2010.
- ⁵⁹ THORNTON, JA. High rate thick film growth. *Annual review of materials science*, **7**(1):239–260, 1977.
- ⁶⁰ EBERG, E, MONSEN, ÅF, TYBELL, T, VAN HELVOORT, ATJ and HOLMESTAD, R. Comparison of TEM specimen preparation of perovskite thin films by tripod polishing and conventional ion milling. *Journal of electron microscopy*, **57**(6):175–179, 2008.
- ⁶¹ AYACHE, J, BEAUNIER, L, BOUMENDIL, J, EHRET, G and LAUB, D. *Sample preparation handbook for transmission electron microscopy: techniques*, vol. 2. Springer Science & Business Media, 2010.
- ⁶² RMC BOECKELER. PowerTome X, XL User Guide. http://rmcboeckeler.com/download/manuals/PowerTome_UG_0815.pdf.
- ⁶³ TEODORESCU, VS and BLANCHIN, MG. Fast and simple specimen preparation for TEM studies of oxide films deposited on silicon wafers. *Microscopy and Microanalysis*, **15**(01):15–19, 2009.
- ⁶⁴ MTEX. MTEX home page. <http://mtex-toolbox.github.io>.
- ⁶⁵ DE LA PEÑA, F, OSTASEVICIUS, T, FAUSKE, VT, BURDET, P, JOKUBAUSKAS, P, NORD, M, PRESTAT, E, SARAHAN, M, MACARTHUR, KE, JOHNSTONE, DN, TAILLON, J, CARON, J, FURNIVAL, T, ELJARRAT, A, MAZZUCCO, S, MIGUNOV, V, AARHOLT, T, WALLS, M, WINKLER, F, MARTINEAU, B, DONVAL, G, HOGGLUND, ER, ALXNEIT, I, HJORTH, I, ZAGONEL, LF, GARMANSLUND, A, GOHLKE, C, IYENGAR, I and CHANG, HW. hyperspy/hyperspy: Hyperspy 1.3. <https://doi.org/10.5281/zenodo.583693>, 2017.
- ⁶⁶ NANOMEGAS. NanoMegas web page. <http://www.nanomegas.com/>.
- ⁶⁷ RAUCH, E and VÉRON, M. Automated crystal orientation and phase mapping in TEM. *Materials Characterization*, **98**:1–9, 2014.
- ⁶⁸ ABRĂMOFF, MD, MAGALHÃES, PJ and RAM, SJ. Image processing with ImageJ. *Biophotonics international*, **11**(7):36–42, 2004.
- ⁶⁹ VAN DER WALT, S, SCHÖNBERGER, JL, NUNEZ-IGLESIAS, J, BOULOGNE, F, WARNER, JD, YAGER, N, GOULLART, E and YU, T. scikit-image: image processing in python. *PeerJ*, **2**:e453, 2014.
- ⁷⁰ Gatan Microscopy Suite Software. <http://gatan.com/products/tem-analysis/gatan-microscopy-suite-software>.
- ⁷¹ HUNTER, JD. Matplotlib: A 2d graphics environment. *Computing In Science & Engineering*, **9**(3):90–95, 2007. doi:10.1109/MCSE.2007.55.
- ⁷² INKSCAPE. Inkscape home page. <https://inkscape.org/en/>.
- ⁷³ DAOU, JN and VAJDA, P. Hydrogen ordering and metal-semiconductor transitions in the system YH_{2+x} . *Physical Review B*, **45**(19):10907, 1992.
- ⁷⁴ ANTIC, B, MITRIC, M and RODIC, D. Structure properties and magnetic susceptibility of diluted magnetic semiconductor $\text{Y}_{2-x}\text{Ho}_x\text{O}_3$. *Journal of magnetism and magnetic materials*, **145**(3):349–356, 1995.
- ⁷⁵ MONGSTAD, TT, PLATZER-BJÖRKMAN, C, KARAZHANOV, SZ, HOLT, A, MAEHLEN, JP and HAUBACK, BC. Transparent yttrium hydride thin films prepared by reactive sputtering. *Journal of Alloys and Compounds*, **509**:S812—S816, 2011.
- ⁷⁶ BARNA, P and ADAMIK, M. Fundamental structure forming phenomena of polycrystalline films and the structure zone models. *Thin solid films*, **317**(1):27–33, 1998.
- ⁷⁷ MENG, Y and ZUO, JM. Three-dimensional nanostructure determination from large diffraction dataset. Wiley Online Library, 2016.
- ⁷⁸ REID, N and BEESLEY, JE. *Sectioning and cryosectioning for electron microscopy*. Elsevier. Sole distributors for the USA, Elsevier Science Pub. Co., 1991.

- ⁷⁹ MONSEN, ÅF. *TEM Characterization of LaFeO₃ Thin Films*. Master's thesis, Norwegian University of Science and Technology, 2006.
- ⁸⁰ ALLIED MultiPrep System Brochure 2015.
<http://alliedhightech.com/Media/Default/EquipmentBrochures/MultiPrep%20Brochure%202015.pdf>.

A | Ultramicrotomy scheme

Steps followed to prepare cross-section, TEM specimens of sputtering deposited, YHO thin film on Si substrates, that easily delaminates from the substrate, using a *RMC Boeckeler PowerTome XL*⁶² ultramicrotome is presented here. The general preparation steps are based on an internal, working instruction document in TEM Gemini Centre and a book by Reid and Beesley,⁷⁸ while the exploitation of the delaminating film are new additions. The scheme steps are shown in Fig. 3.1.

A.1 Film removal from substrate

- ▶ Weigh *Epofix* resin and hardener in a plastic cup with a mixture ratio 25:3 (resin:hardener) and mix thoroughly for three minutes. When cutting sections of various thicknesses of the resulting epoxy, the thickness can be correlated to the colour of the section.
- ▶ Apply the epoxy mixture on the thin film on top of the substrate while carefully aligning a paper clip inside the epoxy. It will later be used to align the film relative to the cutting knife to cut electron transparent cross-sections.
- ▶ Wait at least 8 hours for the epoxy to cure.
- ▶ Carefully cut loose the epoxy and film from the substrate using a scalpel. Inspect the epoxy and substrate to make sure that the film successfully delaminated and is now glued to the epoxy.
- ▶ Weigh *Epofix* resin and hardener in a plastic cup with a mixture ratio 25:3, resin:hardener and mix thoroughly for three minutes.
- ▶ Align the epoxy with the thin film and paper clip in a plastic, embedding capsule so that the film cross-section is facing the bottom of the capsule.
- ▶ Fill the capsule with the epoxy mixture while simultaneously keeping the thin film cross-section aligned with the paper clip.
- ▶ Wait at least 8 hours for the epoxy to cure.
- ▶ Break or cut off the plastic capsule.

A.2 Pre-sectioning cutting

The goal of these steps is to ensure that sections of approximately $(100 \times 200) \mu\text{m}$ with the thin film cross-section in the middle along the $200 \mu\text{m}$ can be cut by the diamond knife, with the cutting direction perpendicular to the thin film growth direction.

- ▶ Fasten the epoxy/film to the sample holder, roughly orienting the thin film so that the cutting direction is perpendicular to the growth direction.
- ▶ Cut away chunks of epoxy/film with a razor blade or scalpel to create a rectangular front face of dimensions of about $(100 \times 200) \mu\text{m}$ while ensuring that the thin film cross-section is in the middle all along the $200 \mu\text{m}$ direction. It is useful to inspect the epoxy/film attached to the ultramicrotome holder in a VLM.
- ▶ Cut the epoxy/film with a triangular glass knife to smooth the sides and front with the thin film in gradually finer microtome sections.

A.3 Sectioning

The goal of these steps is to place multiple, electron transparent, ultramicrotomed sections with strips of thin film on holey-C Cu TEM grids.

- ▶ Choose a diamond knife suited for your material. Fill the trough with water so that the entire surface is reflecting the top light from the ultramicrotome and so that the knife is covered in water. This ensures that the sections float onto the water when cut and does not stick to the knife.
- ▶ Align the epoxy/film so that the knife cutting direction is perpendicular to the film growth direction.
- ▶ Slowly advance the arm by hand or the computer to the diamond knife by using the bottom light and the reflection of the epoxy/film in the knife.
- ▶ Advance the arm in 50 nm steps at a speed of 15 mm s^{-1} using the computer to cut sections, making sure that the slow-moving-regime of the arm movement is when the epoxy/film is on the knife.
- ▶ Cut a sufficient amount of complete sections and let them float on the water. Confirm their thickness by inspecting their colour.
- ▶ Carefully move a TEM grid, with the thin film side down, onto the water at an angle on top of the sections, while holding it in a tweezer. The sections, as well as a water droplet, should stick to the grid when removing it from the water.
- ▶ Remove the water droplet by flipping the grid and placing the side without the C film and sections on the edge of a piece of filter paper, making sure not to bend the grid.
- ▶ Inspect the grid in a VLM to confirm the presence of multiple, electron transparent sections with strips of thin film.
- ▶ Prepare multiple grids to be sure of electron transparent regions.

B | Tripod polishing scheme

Steps followed to prepare sputtering deposited YHO thin films on Si and GaAs substrates for TEM studies using an *Allied MultiPrep* tripod polishing machine is presented here. The steps are based on the tripod polishing scheme reported by Monsen *et. al.*⁷⁹ and Eberg *et. al.*⁶⁰ Although multiple specimens were prepared using this technique during this work, they were not of the same quality as specimens prepared by ultramicrotomy. The latter technique is therefore recommended. The scheme is included as a reference for the discussion in §5.2. It is in large part adapted from the author's project thesis of fall 2016.²⁶

B.1 Cutting and gluing

- ▶ Mount the specimen on a microscope slide with wax.
- ▶ Cut into slabs of $\sim 1 \times 1\text{--}2 \text{ mm}^2$ using a *Testbourne Model 650 Low Speed Diamond Wheel Saw* with a 150 μm thin diamond blade. Use load $> 100 \text{ g}$ and speed 10 rpm. If sawing an Si substrate, make sure to saw along crystallographic axes.
- ▶ Clean the slabs in acetone for $\sim 1 \text{ min}$ and rinse in ethanol to remove the wax.
- ▶ Prepare a clamp with office tape covering the areas where the slabs are to be in contact with the clamp. In gluing the slabs together, place a slab with the thin film side up on the bottom block and apply *Allied EpoxyBond 110* two-part adhesive on the thin film side with a sharpened toothpick. The glue turns red when cured.
- ▶ Put another slab on top of the slab on the bottom block, with thin film sides facing. If more than one thin film interface is desired, put another slab on top of the two slabs with substrate sides facing, apply glue and put yet another slab on top with thin film sides facing, etc. Make sure that all slabs are properly aligned with respect to each other.
- ▶ Attach office tape to the top block and fasten the block with the wing nuts. To ensure that the glue line thins properly while curing, a sufficient pressure must be applied, but not too much so the specimen lamella cracks.
- ▶ Apply *Allied EpoxyBond 110* to the piece of tape on the top block, for visual confirmation of when the glue is cured.
- ▶ Put the clamp on a hot plate set to 150 °C until the glue has cured. This typically takes $\sim 30 \text{ min}$.

- ▶ Cool down the clamp to room temperature before removing the specimen.

B.2 Reference plane polishing

- ▶ Polish a pyrex flat with 6 μm diamond lapping film (DLF) at 50 rpm and 500 g load, using an oscillation speed of 1 with deflection about half the platen radius. Rinse the platen continuously with water. Afterwards, rinse the pyrex in acetone followed by ethanol and inspect surface in a visible-light microscope (VLM).
- ▶ Attach the specimen to the pyrex with *Loctite Precision* acetone soluble glue, using the side that is closest to being perpendicular to the thin film interface(s). Apply the glue with a sharpened toothpick. Make sure to place the specimen edge as parallel to the pyrex edge as possible. Let the glue cure for ~ 2 hours.
- ▶ Adjust sideways tilt-angle with right micrometer-screw if the pyrex surface is not perpendicular to the interface(s).
- ▶ If the slabs in the cross-section specimen is not well aligned, polish with 15 μm DLF at 30 rpm and 200 g load until the specimen is flat, while using lateral oscillation and continuously rinsing with water. Rinse the DLF and specimen in de-ionised (DI) water before the next step. When the specimen is flat, both the substrate and film are polished at the same rate, keeping the interfacial plane perpendicular to the polishing surface.
- ▶ Polish off ~ 50 μm with 6 μm DLF, using same conditions as in the previous step. Inspect in a VLM to ensure removal of the proper amount of material.
- ▶ Polish off ~ 20 μm with 3 μm DLF, using same conditions as in the previous step.
- ▶ Polish off ~ 10 μm with 1 μm DLF and use *Allied GreenLube* lubricant instead of water. Use 50 g load, but otherwise same conditions as in the previous step. Inspect the specimen for scratches in a VLM and repeat this step if deep scratches are observed.
- ▶ Polish off ~ 0.1 μm with 0.5 μm DLF, using same conditions and inspections as in the previous step.
- ▶ Polish with 0.1 μm DLF for 10–15 s, without using lateral oscillation. Otherwise same conditions and inspections as in the previous step.
- ▶ Polish with a felt cloth stained with *Allied 0.02 μm Colloidal Silica* polish solution for ~ 1 min at 0 g load. Clean the specimen with *Allied Micro Organic* soap using a cotton-tip applicator, rinse in DI water and repeat cleaning two more times.
- ▶ Detach the specimen from the pyrex by putting it in an acetone beaker for ~ 30 min, followed by shorter immersions in fresh acetone and ethanol beakers.
- ▶ Attach the newly polished reference plane of the specimen to the pyrex using *Loctite Precision* glue as before.

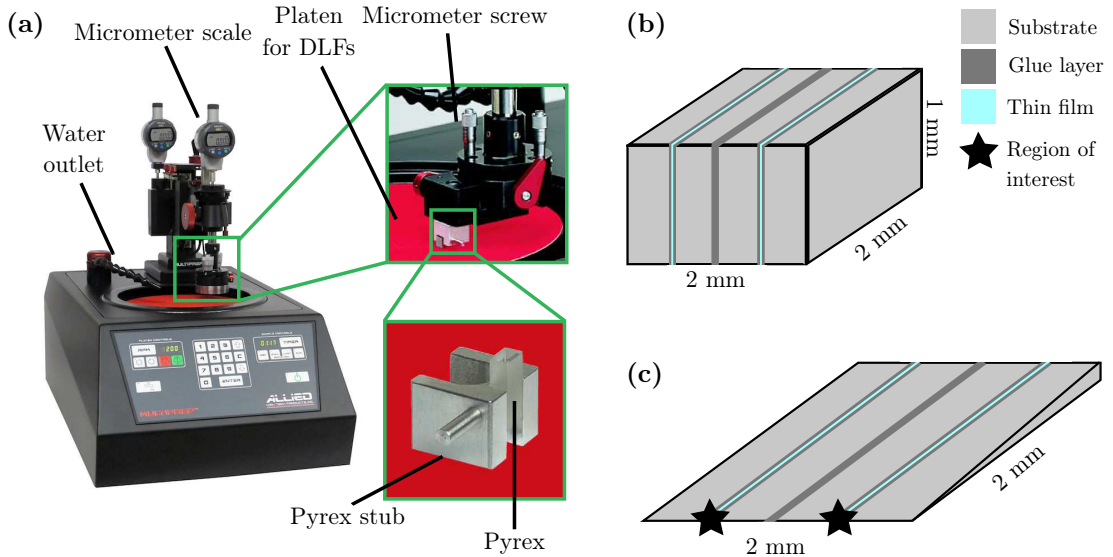


Figure B.1: Allied MultiPrep tripod polishing machine (a), showing the polishing arm with platen for DLFs and micrometer screws and the pyrex stub for attaching the specimen.⁸⁰ Geometry of the substrate and thin film lamella before thinning (b). Lamella after thinning (c), with regions of interest highlighted with stars. The dimensions of film, substrate and glue layer thickness are not on scale.

B.3 Second side polishing

- ▶ If the specimen is $> 500 \mu\text{m}$ thick, polish down to $500 \mu\text{m}$ with $15 \mu\text{m}$ DLF at 30 rpm, 200 g load and oscillation speed 1 with deflection about half the platen radius. Rinse platen continuously with water. Introduce a wedge angle of 2° relative to the platen by turning left micrometer-screw, at a thickness of $500 \mu\text{m}$. Polish further down to $250 \mu\text{m}$.
- ▶ Polish down to $150 \mu\text{m}$ with $6 \mu\text{m}$ DLF, using same conditions as in the previous step.
- ▶ Polish down to $60 \mu\text{m}$ with $3 \mu\text{m}$ DLF, using same conditions as in the previous step.
- ▶ Set load to 0 g and polish with $1 \mu\text{m}$ and *Allied GreenLube* lubricant instead of water. Check the specimen height in a VLM every 30 s, as the micrometer scale of the polisher is not accurate when no load is applied. Weak thickness fringes should appear at this step. Polish until the wedge is at the region of interest (ROI).
- ▶ Polish for 15 s until the wedge is at the ROI with $0.5 \mu\text{m}$ DLF, otherwise same conditions as in the previous step. The thickness fringes should be more pronounced. If not repeat this step. Also repeat this step if the ROI starts to crack.
- ▶ Polish for 15 s with $0.1 \mu\text{m}$ DLF, otherwise same conditions as in the previous step. If the ROI starts to crack, repeat this step or the two previous steps.
- ▶ Polish with a felt cloth stained with *Allied 0.02 \mu\text{m} Colloidal Silica* polish solution for ~ 1 min. Clean the specimen with *Allied Micro Organic* soap using a cotton-tip applicator, rinse in DI water and repeat cleaning two more times.
- ▶ Mount the specimen to a copper (Cu) grid as described in Section B.4.

B.4 Specimen mounting

Fig. B.2 shows a specimen lamella attached to a grid ready for insertion in a TEM holder.

- ▶ Apply a very small amount of *Biltema Quick-Epoxy* two-part, acetone-resistant glue on the thick part of the specimen while it is still attached to the pyrex. Put a Cu TEM grid on top of the specimen on the glue, not covering the electron transparent area, with a vacuum tweezer. Apply a gentle force with a toothpick to press the grid to the specimen. Let the glue cure for ~ 2 hours.
- ▶ Put the pyrex in an acetone beaker upside down on filter paper so the grid will fall onto the filter paper with specimen on the upside.
- ▶ When the grid falls off the pyrex, put it in a fresh acetone beaker for 15 min before putting it in an ethanol beaker. The specimen is now very brittle and should only be handled with a vacuum tweezer.

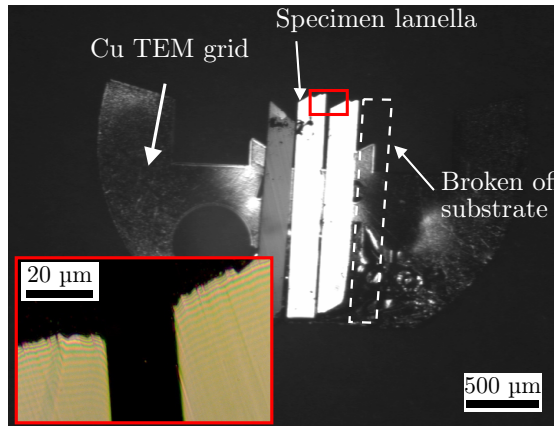


Figure B.2: Specimen lamella glued to a Cu TEM grid. The insert shows Si substrates with thickness fringes indicating thin regions. The glue layer have been removed unintentionally during polishing. According to Eberg et. al,⁶⁰ it is crucial that the glue layer is very thin (< 50 nm). Even though the initial layer is much thicker for this particular specimen, the preparation ended in a TEM specimen with electron transparent regions.

C | Data analysis code snippets

Creating a 1D diffraction pattern

```
1 import numpy as np
2 import matplotlib.pyplot as plt
3
4
5 def create_1d_pattern(pattern_2D, centre=(1024, 1024)):
6     """Create a 1D diffraction pattern from a 2D diffraction pattern.
7
8     Parameters
9     -----
10    pattern_2D: str
11        Path to image file of the 2D diffraction pattern.
12    centre: tuple, ints
13        Position of direct beam.
14
15    Returns
16    -----
17    pattern_1D: numpy array
18        1D diffraction pattern.
19
20    """
21
22    dp = plt.imread(pattern_2D)
23    centre = np.array([centre])
24
25    z = dp.shape[0] - centre.max()
26    y, x = np.indices((z, z))
27    r = np.sqrt((x - int(z/2))**2 + (y - int(z/2))**2)
28    r = r.astype(int)
29    r -= int(r.min())
30
31    counts = np.bincount(r.ravel(), weights=dp.ravel())
32    nr_occur = np.bincount(r.ravel())
33    pattern_1D = counts/nr_occur
34
35    return pattern_1D
```

Listing C.1: Function for creating a 1D diffraction pattern from a 2D diffraction pattern in Python.

Orientation data filtering and grain reconstruction

```
1 % Import .ang file
```

```

2 file = 'path/to/file';
3
4 % Define crystal structure
5 cs = {...
6     'notIndexed',...
7     crystalSymmetry('m-3m', [5.3867 5.3867 5.3867], 'mineral', 'YHO',...
8     'color', 'green')
9 };
10 cs_yho = crystalSymmetry('m-3m', [5.3867 5.3867 5.3867], 'mineral', 'YHO',...
11     'color', 'green');
12
13 % Set plotting convention
14 setMTEXpref('xAxisDirection', 'east');
15 setMTEXpref('zAxisDirection', 'intoPlane');
16
17 % Load data
18 raw_data = loadEBSD(file, cs, 'interface', 'ACOM',...
19     'convertEuler2SpatialReferenceFrame', 'ColumnNames', {'euler1' 'euler2'...
20     'euler3' 'X' 'Y' 'index' 'relperc' 'phase' 'rel'});
21
22 % Set scan unit (default is um)
23 raw_data.scanUnit = 'nm';
24
25 % Check average reliability and index
26 aveRel = mean(raw_data.rel);
27 aveInd = mean(raw_data.index);
28
29 % Filter data by reliability (R) and index (Q). Set unreliable pixels to
30 % notIndexed (0)
31 data = raw_data;
32 data(data.index < aveInd/2).phase = 1
33
34 % Calculate the optimal value for the orientation cluster segmentation
35 % sensitivity C in the fast multiscale clustering algorithm
36 c = linspace(0.1,5,50);
37 numC = length(c);
38 variances = zeros(1, c);
39 clusters = zeros(1, c);
40 data_yho = data('YHO');
41
42 for i=1:numC
43     c = cs(i);
44     [grains,data_yho.grainId] = calcGrains(data_yho, 'FMC',cs(i));
45     numGrains = length(grains);
46     grainVariance = zeros(1, numGrains);
47     for j=1:numGrains
48         grainOris = data_yho(grains(j)).orientations;
49         grainOrisFR = grainOris.project2EulerFR;
50         grainVariance(j) = var(grainOrisFR);
51     end
52     variances(i) = mean(grainVariance);
53     clusters(i) = numGrains;
54 end
55
56 % Before moving on, plot variance v clusters and fit two line segments to the
57 % data. The C value at the breakpoint is the optimal value. A code snippet in
58 % Python is included below.
59
60 % Reconstruct grains based on the optimal calculated value C = 2.6

```

```

61 [grains, data.grainId, data.mis2mean] = calcGrains(data, 'FMC', 2.6)
62
63 % Remove grains at the image boundaries
64 outerBoundary_id = any(grains.boundary.grainId==0,2);
65 grain_id = grains.boundary(outerBoundary_id).grainId;
66 grain_id(grain_id==0) = [];
67 grains(grain_id) = [];
68
69 % Remove unreliable grains where less than 25% of the pixels have a reliability
70 % higher than 15%, suggested by Rauch, E and Veron, M.
71 thresholdR = 15;
72 num_grains = length(grains);
73 grain_id = [];
74
75 for i = 1:num_grains
76     % Find all pixels in grain with reliability better than thresholdR
77     nrelpx = length(find(data(grains(i)).rel > thresholdR));
78     if nrelpx < thresholdPx*grains(i).grainSize
79         grain_id = [grain_id i];
80     end
81 end
82
83 grains(grain_id) = [];
84
85 % Smooth grain boundaries
86 grains = smooth(grains, 2);
87
88 % Determine grain size equivalent diameter
89 diameter = 2*grains.equivalentRadius;

```

Listing C.2: Orientation data filtering and grain reconstruction in the Matlab texture toolbox MTEX.

```

1 import scipy.optimize as sco
2 import numpy as np
3
4
5 # Read values for C and variances from a text file
6 c, variances = np.loadtxt('path/to/file.txt', unpack=True)
7
8 def piecewise_linear(x, x0, y0, k1, k2):
9     """Perform piecewise linear regression."""
10    return np.piecewise(x, [x < x0], [lambda x:k1*x + y0-k1*x0, lambda x:k2*x +
11    y0-k2*x0])
12
13 # Fit two line segments to the data using piecewise linear regression
14 p, e = sco.curve_fit(piecewise_linear, c, variances)
15
16 # Print the optimal value
17 p[0]

```

Listing C.3: Performing segmented linear regression on the plot of average variance of orientations within clusters calculated for each segmentation sensitivity value C, in Python.

EDS quantification

```

1 import hyperspy.api as hs
2 import pandas as pd
3 import re
4

```

```

5
6 # The following code for the creation of a HyperSpy signal from an EDS map
7 # acquired through the Oxford AZtec software was created by PhD student Adrian
8 # Lervik at NINU. The necessary files to export from AZtec are:
9 # * .rpl = datafile from exported MAPDATA
10 # * .msa = energy calibration of single spectra
11 # * .txt = spatial calibration from an EDS map metadata (details)
12
13 # Define file paths
14 FILES_PATH = 'path/to/files'
15 RAW = PATH + 'rawfile'
16 MSA = PATH + 'msafile'
17 METADATA = PATH + 'metadatafile'
18
19 # Load files
20 s = hs.load(RAW, signal_type='EDS_TEM').as_signal1D(0)
21 spatial_calibration_rawdata = pd.read_csv(MSA, sep='\t', header=None)
22 single_spectra = hs.load(MSA, signal_type='EDS_TEM')
23
24 # Energy calibration
25 s.get_calibration_from(single_spectra)
26 s.axes_manager[2].name = 'Energy'
27
28 # Spatial resolution calibration
29 columns = ['2', '3', '4', '5']
30 spatial_calibration = []
31 for column in columns:
32     a = [int(s) for s in re.findall(r'\d+',
33                                     string=(spatial_calibration_rawdata.
34                                               get_value(
35                                                 int(column), 1, takeable=False)))]
36     spatial_calibration.append(a[0])
37
38 names = ['x', 'y']
39 units = 'nm'
40 scales = [spatial_calibration[2]/spatial_calibration[0],
41           spatial_calibration[3]/spatial_calibration[1]]
42
43 for i in range(2):
44     ax = s.axes_manager[i]
45     ax.name = names[i]
46     ax.units = units
47     ax.scale = scales[i]
48
49 # Save file
50 s.save('edsmap.hdf5', extension='hdf5')

```

Listing C.4: Exporting an EDS map from AZtec and creating a HyperSpy signal. It is written by PhD student Adrian Lervik at NTNU.

```

1 import hyperspy.api as hs
2
3
4 # Load EDS map from .hdf5 file
5 s = hs.load('path/to/file')
6
7 # Add elements of peaks to quantify
8 s.add_elements(['O', 'Y'])
9

```

```
10 # Ask HyperSpy to find the relevant peaks
11 s.add_lines()
12
13 # Integrate the intensities inside the peaks using an automatic window
14 intensities = s.get_lines_intensity()
15
16 # Define theoretical k factors from Oxford AZtec software
17 kfactors = [1.977, 1.754] # O Ka, Y La
18
19 # Calculate atomic percents (at.%) using the Cliff-Lorimer ratio technique
20 atomic_percent = s.quantification(intensities=intensities, method='CL',
21                                 factors=kfactors)
22
23 # Rebin dataset and normalise to create a line plot and extract the O Ka and
24 # Y La peaks. For that we need the size of the map in the y direction
25 s_y = s.axes_manager['y'].size
26 o_rebin = atomic[0].rebin(newshape=(1, s_y))/s_y
27 y_rebin = atomic[1].rebin(newshape=(1, s_y))/s_y
```

Listing C.5: Atomic percent quantification using the Cliff-Lorimer ratio technique, facilitated by the HyperSpy library in Python.

D | Study of GaAs nanowires

To test if the number of component patterns returned from an NMF decomposition can be limited to the number of orientations or phases in the studied volume, a SPED dataset was acquired from an epitaxially grown GaAs nanowire by Prof. Antonius van Helvoort and the author. It consists of two twinned zinc-blend crystal structures and one wurtzite crystal structure. The nanowires were dispersed on a holey-C Cu TEM grid. The SPED acquisition parameters are included in Tab. D.1.

Table D.1: Parameters used to acquire a SPED dataset from a GaAs nanowire specimen.

Parameter	Value
Probe spot size	1.0 nm
Semi-convergence angle α	1.0 mrad
Camera length	20 cm
Precession angle ϕ	0.5°
Precession frequency ω	100 Hz
Probe positions	(111 × 386)
Probe step length	3.2 nm
Exposure time	10 ms

Fig. D.1 shows a plot of the proportion of variance as a function of principal components from a PCA decomposition performed on parts of the acquired dataset. Compared to the similar plot of the PCA decomposition of the YHO dataset in Fig. 4.10, the drop in proportion of variance is notable, making it easier to discern how many orientations and phases is present in the dataset. Based on visual inspection of the components and the plot, the first five components were considered to be signal while the rest were discarded as noise.

A VBF image from the dataset, with the region of interest decomposed by NMF highlighted in a red square, is shown in Fig. D.2 (a). The decomposition was asked to keep the first five components, of which three is shown. The nanowire’s full structure is described by the three component patterns (e,f,g) and corresponding loading maps (b,c,d). Component patterns (e,g) are the two twinned zinc-blend structures, while pattern (f) is the wurtzite structure. This example demonstrates the power of an unbiased, robust method to separate diffracted intensities in a SPED dataset.

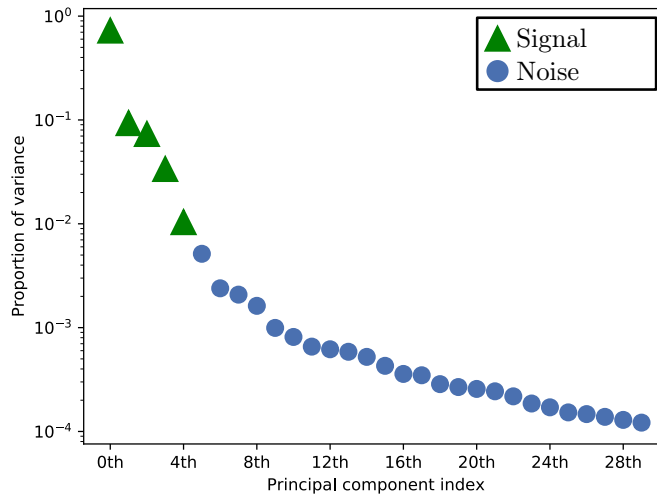


Figure D.1: Proportion of variance as a function of principal components from a PCA decomposition of a SPED dataset from the GaAs nanowire. Based on visual inspection of the components returned by the decomposition, the first five components were considered to be signal while the rest was discarded as noise. Note that component #1 is termed the 0th component in the plot.

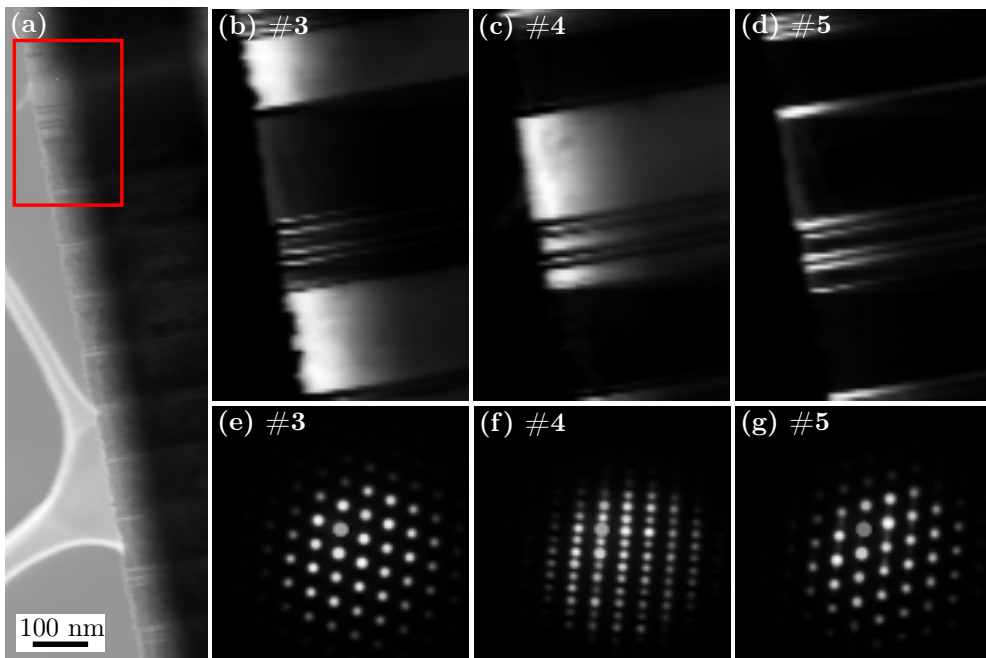


Figure D.2: A SPED dataset was acquired from a GaAs nanowire, shown in the VBF image (a). An NMF decomposition asked to keep the five first components were performed on the PED patterns within the red square. Component patterns (e,g) and corresponding loading maps (b,d) show where the two twinned zinc-blend structures are present, while component pattern (f) and its corresponding loading map (c) show the wurtzite structure.